Graduate School
UNIVERSITY OF COLORADO **BOULDER**

Thesis Approval Form

Student Name Shaun Burd Student ID 104352524

Doctoral Degree in Physics

Thesis Title:

Squeezing and amplification of trapped-ion motion

Have you performed research involving human subjects which requires approval from the Institutional Review Board (IRB)? ___ Yes _X_ No

IRB Protocol Number _____

Have you used live animals, animal tissue, or observational animal work which requires approval from the Institutional Animal Care and Use Committee (IACUC)? ___ Yes _X_ No

IACUC Protocol Number _____

Attach the final copy of thesis/dissertation for committee review. While formatting changes may be requested by the Graduate School, the content of the attached document should be final.

Approvals:

Committee Chair Name Dietrich Leibfried

Signature DocuSigned by: Dietrich Leibfried 5FB45ABA56E44F8... Date Signed 7/27/2020

Committee Member Name David Wineland

Signature DocuSigned by: David Wineland 016F2529282F430... Date Signed 7/27/2020

The final copy of this thesis has been examined by the signatories, and we find that both the content and the form meet acceptable presentation standards of scholarly work in the above-mentioned discipline.

Squeezing and amplification of trapped-ion motion

by

Shaun C. Burd

B.S., University of the Witwatersrand, 2010

M.S., University of Natal, 2014

A thesis submitted to the

Faculty of the Graduate School of the

University of Colorado in partial fulfillment

of the requirements for the degree of

Doctor of Philosophy

Department of Physics

2020

This thesis entitled:
Squeezing and amplification of trapped-ion motion
written by Shaun C. Burd
has been approved for the Department of Physics

_____

Dr. Dietrich Leibfried

_____

Prof. David J. Wineland

Date _____

The final copy of this thesis has been examined by the signatories, and we find that both the content and the form meet acceptable presentation standards of scholarly work in the above mentioned discipline.

Burd, Shaun C. (Ph.D., Physics)

Squeezing and amplification of trapped-ion motion

Thesis directed by Dr. Dietrich Leibfried and Prof. David J. Wineland

In my thesis work I have explored a variety of ways for using parametric modulation to control the dynamics of trapped atomic ions. Parametric modulation allows the wavefunction of a quantum oscillator to be reversibly distorted or "squeezed" by redistributing quantum fluctuations between conjugate observables. This enables tailoring of an oscillator's wavefunction to enhance the sensitivity of measurements of observables of interest, and permits amplification of the oscillator's motion. In our experiment, parametric modulation is implemented by periodic distortion of the confining potential of the ion trap. With this tool, we can prepare oscillator states with up to 20 decibels of squeezing in 5 μs, a duration short compared to the oscillator coherence time. Furthermore, parametric modulation implements a unitary squeezing operator, enabling nearly noise-free amplification of harmonic oscillator displacements. Using this amplification method, we have increased the sensitivity for measurements of weak forces by up to 17 decibels. Unitary squeezing also enables amplification of phonon-mediated interactions between trapped-ion qubits — allowing us to accelerate the generation of entanglement between qubits. Additionally, I describe experiments demonstrating "Hamiltonian amplification", a general method for using parametric modulation to accelerate dynamics of quantum systems governed by a wide variety of Hamiltonians. The methods demonstrated here can potentially extend the capabilities of many physical platforms used for precision measurements, quantum information science, and explorations of fundamental physics, in which harmonic oscillators are essential components.

Dedication

To my wife Caroline, my son James, and my parents.

Acknowledgements

Firstly, I thank my supervisors Didi Leibfried and Dave Wineland for giving me the opportunity to work in the NIST Ion Storage Group. It has been a great privilege to work with some of the brightest people in experimental physics. I am very grateful that I was allowed and encouraged to pursue independent research directions. I feel that this allowed me to grow as a physicist. I am also indebted to John Bollinger for his continued support and advice, and to Andrew Wilson for helping to keep everything working.

Special thanks go to the other members of the "μCrew". To my fellow grad student and best man Raghu Srinivas, we had many thought-provoking discussions about physics, and we also had fun outside of lab watching movies and playing board games. Thanks also to David Allcock and Daniel Slichter, my postdocs during most of my time at NIST, two of the smartest people I have ever met. Although I couldn't understand what he was saying at first, David eventually taught me the art of planning and engineering an experiment, and other important things an experimentalist should know like how (and how not) to solder, how to connect the inputs and outputs of microwave amplifiers, and how to find tiny screws dropped into the depths of over-engineered equipment. Daniel showed me the importance of paying attention to detail and how to write the best possible paper. To Hannah, and Laurent, thanks for reading my thesis, maybe we will finally trap calcium.

In addition to those mentioned above, I had the opportunity to work with many great physicists in the ion-storage group: David Hume, Chin Wen Chou, Ethan Clements, Steven Erickson, Yong Wan, Yiheng Lin, David Leibrandt, Ryan Bowler, Ting Rei Tan, John Gaebler, Kevin Gilmore, Elena Jordan, Alejandra Collopy, May Kim, Panyu Hou, Jenny Wu, Dan Cole, Sam

Brewer, Matt Affolter, Dalton Chaffee, Kaifeng Cui, Jonas Keller, Robert Jördens, Katie McCormick, Susanna Todaro, Justin Niedermeyer, Justin Bohnet, Brian Sawyer, and Joe Britton. I would also like to thank several of my mentors from my time at the CSIR in South Africa, Christoph Bollig, who introduced me to real lasers, Musa "Yoda" Mhlanga my supervisor during my foray into molecular biology, and Hermann Uys, who introduced me to atomic physics and guided me to NIST. Finally, I would like to thank my family. Thank you to my beautiful wife Caroline, who has always stood by me; my mother Annette, who raised me and tolerated my many science experiments; and my father Michael for always supporting me every time I decided to change my career path.

Contents

Chapter

Tables

Table

Figures

Figure

Chapter 1

Introduction

Control of systems at the quantum level has led to advances such the observation of exotic states of matter [1], precision measurements of unprecedented accuracy [2], and the development of quantum computers and simulators [3, 4, 5]. In many physical platforms for quantum science, harmonic oscillators are essential components and are used directly as sensors or to mediate interactions between other quantum objects. Expanding the toolbox of methods for controlling a quantum oscillator will likely lead to an improved understanding of quantum physics and to novel applications. In this thesis, I present new methods for controlling quantum states of trapped-ion harmonic oscillators. While laser-based methods have traditionally been used for high-fidelity manipulation of both the internal and oscillator degrees of freedom of trapped ions, here I describe methods that use magnetic and electric fields at much lower frequencies for controlling trapped ion dynamics. In particular, modulation of electric field gradients enables the generation of squeezed harmonic oscillator states, which can be used as a resource for quantum-enhanced metrology. This parametric modulation produces a unitary squeezing operation that has been challenging to implement using laser methods. Beyond generating metrologically useful states, unitary squeezing enables amplification of interactions between harmonic oscillators and external fields and also enables amplification of interactions between quantum objects that are mediated by harmonic oscillators, which are essential for quantum-information processing in a variety of physical platforms. While the experiments described in this thesis were implemented using trapped ions, these techniques should be applicable to any system where the required interactions can be generated.

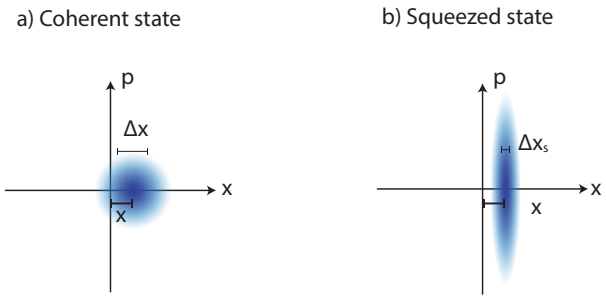

Figure 1.1: Phase-space illustration (not to scale) of a squeezing enhanced position measurement. a) Coherent state with position uncertainty Δx displaced by x. b) Squeezed state where the uncertainty Δx_s for measuring the system position has been reduced compared to the coherent state.

1.1 Squeezing and metrology

Quantum-enhanced metrology aims to use intrinsically quantum effects such as entanglement and superposition for increasing the sensitivity of measurements beyond what could be achieved using classical methods. One method for obtaining quantum-enhanced measurement sensitivity is the method of squeezing. The key concept is illustrated in Figure 1.1. Consider measurements of two non-commuting observables such as the position x and momentum p of a mechanical oscillator. The uncertainties for measuring these quantities Δx and Δp are constrained by the Heisenberg uncertainty principle $\Delta x \Delta p \geq \hbar/2$. By squeezing the oscillator, the uncertainties for measuring these observables can be redistributed, allowing greater sensitivity for measuring one observable at the expense of increased fluctuations of the other.

The seminal work of Caves [6] was the first detailed proposal describing how squeezed light can improve the sensitivity of gravitational wave detectors. Work by Wineland et al. [7, 8], and Kitagawa and Ueda [9] laid out the theory of spin squeezing, paving the way towards quantum-enhanced atomic clocks and atom interferometers. Squeezed states are now routinely created in a variety of physical systems including electromagnetic fields [10], spin systems [11, 12, 13, 14, 15], micro-mechanical oscillators [16, 17, 18], and the motional modes of single trapped ions [19, 20]. However, exploiting squeezing for enhanced metrology has proven to be challenging. One reason is

that large squeezed states can be very sensitive to perturbations from the environment that result in their decoherence. Another more subtle reason is that a detection method with noise below the squeezed noise is typically required to take advantage of squeezing. These challenges are not fundamental and are being overcome by technological improvements. Almost forty years after the original proposal [6], squeezed light was used in LIGO to give a 2.2 dB sensitivity enhancement [21]. Furthermore spin-squeezed atom interferometers [22] and optical atomic clocks [23] are on the horizon.

1.2 Squeezed states in trapped ions

Trapped atomic ions form one of the most pristine platforms for experimental quantum physics. The ions' motion can be described as an almost ideal quantum harmonic oscillator and specially chosen pairs of internal electronic states can serve as qubits for quantum computation or simulation applications. Both squeezed states of the harmonic motion of ion crystals, and spin-squeezed states of hundreds of ions [24] have been realized experimentally. Squeezing of the motional state has been accomplished using several methods. Historically, the proposal of Heinzen and Wineland [25] was the first to describe using parametric modulation for squeezing and amplification of the motion of trapped charged particles. Resonant parametric modulation involves applying an oscillating potential at twice the motional frequency to squeeze the motional state. While electronic (laser-free) parametric modulation has been used to squeeze the thermal motion of of single ions [26] and for phase-sensitive parametric amplification of highly displaced thermal states [27], it has not previously been implemented with ions cooled close to the motional ground state. Optical forces can also be used for parametric modulation [19, 28], but decoherence due to photon scattering and higher order nonlinearities in the optical field have limited the achievable squeezing [19]. An alternative method known as reservoir engineering [16, 20] relies on dissipative processes to prepare an oscillator in a squeezed state.

A key enabling technology for the experiments described in this thesis is the implementation of direct electronic parametric modulation in a surface-electrode ion trap, with ions initially cooled

close to the motional ground state. With this method we can rapidly prepare and manipulate large squeezed states. In contrast to methods for preparing squeezed states that rely on dissipation, parametric modulation is unitary, enabling reversal of the squeezing and ideally noiseless phase-sensitive amplification of ion motion. For sensing applications, noiseless amplification can reduce the requirements of low noise detection. In a force sensing protocol we use squeezing-based amplification to improve the measurement sensitivity by a factor of 17(3) dB.

1.3 Beyond metrology

The applications of parametric modulation in quantum systems extends far beyond the generation of squeezed states. In trapped-ion and other experimental platforms for quantum information processing and simulation, interactions between qubits are often mediated by bosons - excitations of a shared harmonic oscillator coupled to the qubits. These interactions can be amplified by parametrically modulating the shared harmonic oscillator. We demonstrate this by using parametric driving to speed up the generation of a maximally entangled Bell state between two trapped-ion qubits. More generally, parametric modulation can be used to increase coupling strengths in a large class of Hamiltonians involving harmonic oscillator degrees of freedoms, and should enable exploration of new parameter regimes for fundamental studies of quantum mechanics, and improved quantum information processors and simulators.

1.4 Thesis structure

Chapter 2 reviews the theory of quantum harmonic oscillators with a focus on parametric modulation and squeezing in trapped ion systems.

Chapter 3 gives an overview of spin-motion coupling using magnetic field gradients including the theory of spin-dependent forces and trapped-ion entangling gates.

Chapter 4 presents the experimental system. This includes descriptions of the $^{25}Mg^{+}$ ion internal structure, the surface-electrode ion trap, vacuum system, laser systems, microwave systems, and parametric drive.

Chapter 5 discusses the preparation and analysis of various harmonic oscillator states including number states, coherent states, and squeezed states, using laser-free methods.

Chapter 6 describes an experimental implementation of phase-sensitive amplification of coherent displacements of a single trapped ion.

Chapter 7 extends the technique discussed in Chapter 6 to allow phase-insenstive amplification and describes an experimental demonstration of "Hamiltonian amplification" a method for accelerating dynamics for a large class of Hamiltonians.

Chapter 8 describes parametric amplification of phonon-mediated interactions between two trapped-ion qubits leading to a reduction in the time required to implement an entangling gate.

Chapter 9 summarizes key results of the thesis and discusses prospective outlooks.

Chapter 2

The harmonic oscillator

Harmonic oscillators are ubiquitous in nature. Systems as seemingly varied as a mass on a spring, an electromagnetic field in a cavity, and the vibrations of atoms in molecules can all be described as harmonic oscillators. The harmonic oscillator is defined as a system that is subject to a restoring force proportional to the displacement of the oscillator from its equilibrium position. For a one-dimensional oscillator where the displacement from equilibrium is denoted by x, the restoring force is given by Hooke's law: $F = -kx$, where k is the spring constant. This corresponds to the conservative potential $V(x) = \frac{1}{2}kx^2$. Summing the kinetic and potential energies gives the Hamiltonian for a classical harmonic oscillator:

$$H = \frac{1}{2m}p^2 + \frac{1}{2}m\omega^2x^2, \tag{2.1}$$

where m is the mass of the oscillator, $\omega = \sqrt{\frac{k}{m}}$ is the oscillator frequency, and p is the momentum of the oscillator. The total energy of the oscillator E and the position and momentum are constrained to fall on ellipses in phase space given by

$$E = \frac{1}{2m}p^2 + \frac{1}{2}m\omega^2x^2. \tag{2.2}$$

The position and momentum oscillate sinusoidally in time according to

$$x(t) = A\sin(\omega t + \phi),$$

and,

$$p(t) = Am\omega\cos(\omega t + \phi), \tag{2.3}$$

where the amplitude A and phase ϕ depend on the initial conditions. The motion can be described in terms of the dimensionless variables

$$\tilde{x} = \frac{1}{2}\sqrt{\frac{2m\omega}{\hbar}}x, \tag{2.4}$$

and

$$\tilde{p} = \frac{1}{2}\sqrt{\frac{2}{m\hbar\omega}}p. \tag{2.5}$$

In this picture, the oscillator follows circular trajectories in phase space with amplitude $\alpha = \sqrt{mw/2\hbar}A$. Planck's constant $\hbar$ has been used in the definitions of $\tilde{x}$ and $\tilde{p}$ in anticipation of the phase-space description of the quantum harmonic oscillator. However, $\hbar$ can be replaced by any constant with units of angular momentum to give a dimensionless transformation.

In the next sections we move to the quantum mechanical description of the harmonic oscillator. After reviewing the theory of the quantum oscillator, I will describe several important quantum states of the harmonic oscillator, their properties, and how they can be generated.

2.1 The quantum harmonic oscillator

The Hamiltonian for the quantum harmonic oscillator is obtained from the classical one by replacing the canonical variables x and p with operators $\hat{x}$ and $\hat{p}$, giving

$$\hat{H} = \frac{1}{2m}\hat{p}^2 + \frac{1}{2}m\omega^2\hat{x}^2. \tag{2.6}$$

The canonical operators satisfy the commutation relation $[\hat{x}, \hat{p}] = i\hbar$. The harmonic oscillator Hamiltonian can be diagonalized by expressing $\hat{x}$ and $\hat{p}$ in terms of the raising and lowering operators $\hat{a}$ and $\hat{a}^\dagger$ as $\hat{x} = x_0(\hat{a} + \hat{a}^\dagger)$, where $x_0 = \sqrt{\frac{\hbar}{2m\omega}}$, and $\hat{p} = ip_0(\hat{a}^\dagger - \hat{a})$, where $p_0 = \sqrt{\frac{\hbar m\omega}{2}}$. The

creation and annihilation operators satisfy the commutation relations $[\hat{a}, \hat{a}^\dagger] = 1$. The Hamiltonian can then be written as

$$\hat{H} = \hbar\omega \left(\hat{n} + \frac{1}{2} \right), \tag{2.7}$$

where $\hat{n} = \hat{a}^\dagger \hat{a}$. The energy eigenvalues $E_n = \hbar\omega(n + \frac{1}{2})$ are evenly spaced, with integer $n \geq 0$. The eigenstates of the harmonic oscillator (also known as number states) are denoted by $|n\rangle$. One of the striking features of the quantum oscillator is that even in its lowest possible energy state $|n = 0\rangle$, there are fluctuations of the measured position and momentum. To see this consider the uncertainty in observing $\hat{x}$: $\sigma(\hat{x}) = \sqrt{\langle \hat{x}^2 \rangle - \langle \hat{x} \rangle^2}$. In the motional ground state, $\langle 0|\hat{x}|0\rangle = 0$ and $\langle 0|\hat{x}^2|0\rangle = x_0^2$ giving $\sigma(\hat{x}) = x_0$. Similarly, the uncertainty in observing $\hat{p}$ for an oscillator prepared in the motional ground state is $\sigma(\hat{p}) = p_0$. The uncertainties of any non-commuting observables are fundamentally linked by the Heisenberg uncertainty principle. The Heisenberg uncertainty relation for an oscillator in the grounds state is given by

$$\sigma(\hat{x})\sigma(\hat{p}) \geq \frac{1}{2} |\, \langle [\hat{x}, \hat{p}] \rangle \,| = \frac{\hbar}{2} \tag{2.8}$$

Since $\sigma(\hat{x})\sigma(\hat{p}) = \hbar/2$, the uncertainty principle is saturated and the ground state is said to be a minimum uncertainty state. It is also useful to know the underlying probability distribution for position measurements. The probability of finding the oscillator at position x given that it was initially in a number state n is given by $P_x = |\, \langle x|n\rangle \,|^2$. The projections of the eigenstates onto eigenfunctions $|x\rangle$ of the position operator $\langle x|n\rangle$ are known as wavefunctions. The wavefunctions of the harmonic oscillator are given by [29]

$$\langle x|n\rangle = \frac{1}{\sqrt{2^n n!}} \left(\frac{1}{2\pi x_0^2} \right)^{1/4} e^{-\left(\frac{x}{2x_0}\right)^2} H_n \left(\frac{x}{\sqrt{2}x_0} \right) \tag{2.9}$$

where H_n are the Hermite polynomials. Several of these wavefunctions are shown in Fig. 2.1. For the special case of the motional ground state, the wave function is a Gaussian given by

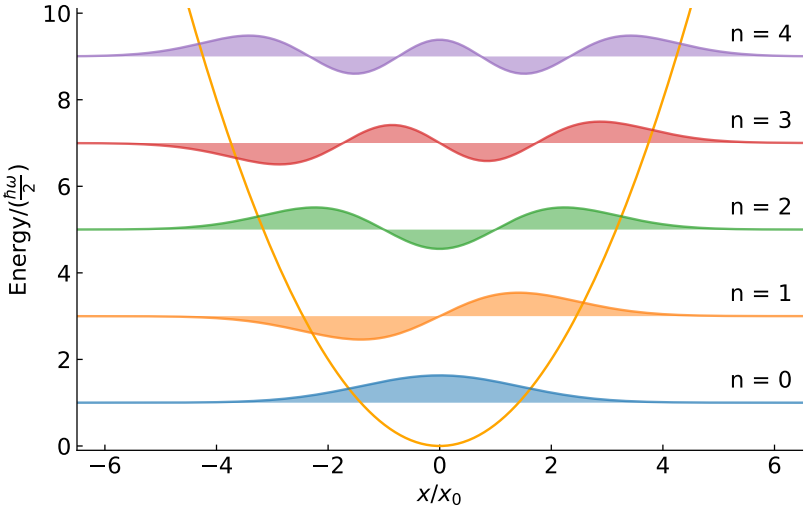

Figure 2.1: Wavefunctions of the quantum harmonic oscillator.

$$\langle x|0\rangle = \left(\frac{1}{2\pi x_0^2}\right)^{1/4} e^{-\left(\frac{x}{2x_0}\right)^2}. \tag{2.10}$$

The probability for measuring the position x when the oscillator was prepared in the ground state is

$$P_0(x) = |\langle x|0\rangle|^2 = \left(\frac{1}{2\pi x_0^2}\right)^{1/2} e^{-\frac{1}{2}\left(\frac{x}{x_0}\right)^2}, \tag{2.11}$$

which is a Gaussian of standard deviation x_0 as expected.

2.2 Wigner function representation

The states of a quantum harmonic oscillator can also be visualized in phase space using a quasi-probability distribution function [30]. Although there are several quasi-probability distribution functions, the Wigner distribution [31] is the most widely used and is most suitable for the quantum states described in this thesis. For an arbitrary density operator $\hat{\rho}$, the Wigner function is defined as

$$W(x,p) \equiv \frac{1}{2\pi\hbar}\int_{-\infty}^{\infty} \langle x + \frac{1}{2}q|\hat{\rho}|x - \frac{1}{2}q\rangle\, e^{ipq/\hbar} dq, \tag{2.12}$$

where $|x \pm \frac{1}{2}q\rangle$ are position eigenstates. The Wigner function for the n^{th} number state is given by [32]

$$W(n,\alpha) = \frac{2}{\pi}(-1)^n \mathcal{L}_n(4|\alpha|^2) e^{-2|\alpha|^2}, \tag{2.13}$$

where $\mathcal{L}_n$ is a Laguerre polynomial of degree n, and $\alpha = x/2x_0 + ip/2p_0$ is a complex dimensionless phase-space coordinate. Example Wigner functions of pure number states are plotted in Fig. 2.2.

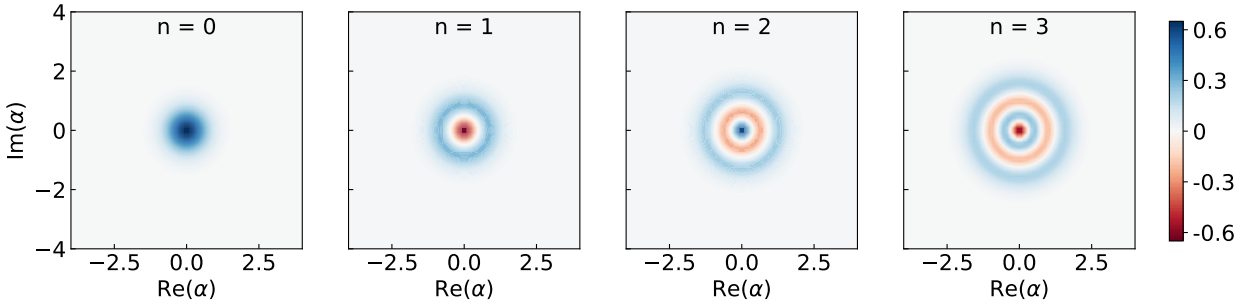

Figure 2.2: Wigner functions of the first few harmonic oscillator number states.

2.3 Coherent states

Coherent states have been described as the most classical-like states of the harmonic oscillator [33]. A coherent state $|\alpha\rangle$ is defined as the eigenstate of the annihilation operator $\hat{a}$ with eigenvalue α, mathematically $\hat{a}\,|\alpha\rangle = \alpha\,|\alpha\rangle$. The coherent state can be expressed in the number state basis as

$$|\alpha\rangle = e^{\frac{-|\alpha|^2}{2}} \sum_{n=0}^{\infty} \frac{\alpha^n}{\sqrt{n!}} |n\rangle\,. \tag{2.14}$$

The probability of finding the oscillator in state $|n\rangle$ after it was prepared in $|\alpha\rangle$ is given by the Poisson distribution

$$P_n = |\,\langle n|\alpha\rangle\,|^2 = e^{-|\alpha|^2} \frac{|\alpha|^{2n}}{n!}, \tag{2.15}$$

which has a mean value of $\langle\hat{n}\rangle = \sum_n nP_n = |\alpha|^2$ equal to its variance. The probabilities P_n for an example coherent state are shown in Fig. 2.3 a. The expectation values of the position and momentum of the coherent state are $\langle\alpha|\hat{x}|\alpha\rangle = 2x_0 Re\{\alpha\}$ and $\langle\alpha|\hat{p}|\alpha\rangle = 2p_0 Im\{\alpha\}$. The uncertainties for measurements of the position are $\sigma(\hat{x}) = x_0$ and $\sigma(\hat{p}) = p_0$. The coherent state therefore has the same phase-space extent as the ground state, but the center of the wavepacket is shifted from the origin by α. This is clear from the coherent state Wigner function (Fig. 2.3 b)

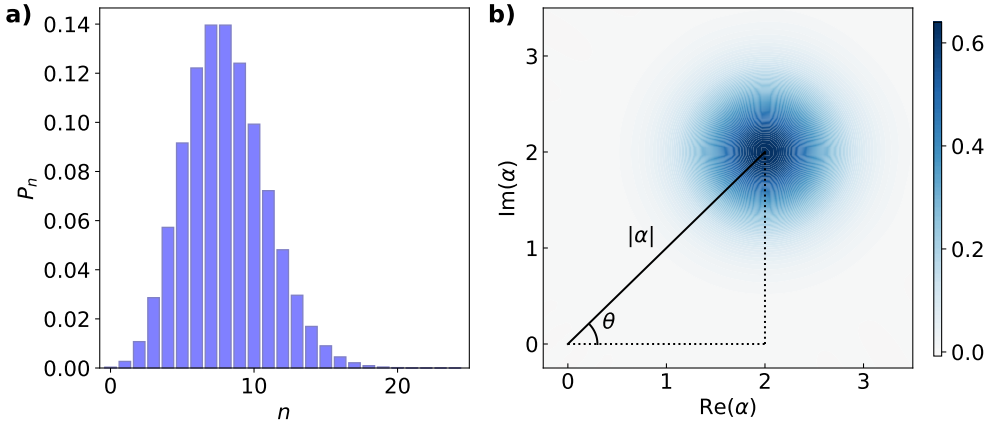

Figure 2.3: a) Number state probabilities and b) Wigner function for a coherent state with $\alpha = 2+2i$

given by [32]

$$W(\alpha, \beta) = \frac{2}{\pi} e^{-2|\alpha-\beta|^2}. \tag{2.16}$$

Coherent states can be generated from the motional ground state by the action of the displacement operator $|\alpha\rangle = \hat{D}(\alpha)\,|0\rangle$ where

$$\hat{D}(\alpha) = e^{\alpha\hat{a}^\dagger - \alpha^*\hat{a}}. \tag{2.17}$$

The displacement operator has some very interesting (and useful!) properties. A displacement followed by a displacement in the opposition direction in phase space brings the system back to where it started, i.e. $\hat{D}^\dagger(\alpha)\hat{D}(\alpha) = \hat{D}(-\alpha)\hat{D}(\alpha) = \hat{I}$. The displacement operator is therefore a unitary operator. The following identities are especially useful:

$$\begin{aligned} \hat{D}^\dagger(\alpha)\hat{a}\hat{D}(\alpha) &= \hat{a} + \alpha \\ \hat{D}(\alpha)\hat{a}\hat{D}^\dagger(\alpha) &= \hat{a} - \alpha, \end{aligned} \tag{2.18}$$

If a displacement by α is followed by a displacement by β,

$$\hat{D}(\beta)\hat{D}(\alpha) = e^{\frac{1}{2}(\beta\alpha^* - \beta^*\alpha)}\hat{D}(\alpha+\beta) = e^{i\mathrm{Im}[\beta\alpha^*]}\hat{D}(\alpha+\beta) \tag{2.19}$$

This can be proved by using the Baker-Campbell-Hausdorff formula [29]. The phase factor is a geometric phase that depends on the area circumscribed by the path in phase space. If the displacements follow a rectangular closed path

$$\hat{D}(-\beta)\hat{D}(-\alpha)\hat{D}(\beta)\hat{D}(\alpha) = \hat{I}e^{\frac{1}{2}(\beta\alpha^* - \beta^*\alpha)}e^{\frac{1}{2}(\beta\alpha^* - \beta^*\alpha)} = \hat{I}e^{2i\mathrm{Im}[\beta\alpha^*]}, \tag{2.20}$$

where $\hat{I}$ is the identity operator, which shows that the geometric phase is equal to the area of the enclosed shape. The presence of this geometric phase is essential for generating entanglement between trapped-ion qubits as described in Chapter 3.

It is useful to consider the displacement operator from a slightly different perspective. From introductory quantum mechanics, the generator of translations in position space is momentum and conversely, the generator of translations in momentum space is the position. For a position translation by an amount x_d, the translation operator is

$$\hat{\mathcal{T}}(x_d) = \exp\left(\frac{-ix_d\hat{p}}{\hbar}\right). \tag{2.21}$$

For the harmonic oscillator, this becomes

$$\begin{aligned}\hat{\mathcal{T}}(x_d) &= \exp\left(\frac{x_d p_0}{\hbar}(\hat{a}^\dagger - \hat{a})\right) \\ &= \exp\left(\frac{x_d}{2x_0}(\hat{a}^\dagger - \hat{a})\right) \\ &= \hat{D}\left(\frac{x_d}{2x_0}\right).\end{aligned} \tag{2.22}$$

Which shows that a displacement by α along the real axis in phase space corresponds to a position translation of $x_d = 2x_0\alpha$. A similar line of reasoning applies to the momentum and further motivates why $\hat{D}(\alpha)$ is called a displacement operator.

2.4 The driven harmonic oscillator

We have seen that a coherent state can be generated by the action of the displacement operator on the ground state. I will now describe how the displacement operator can be implemented

using an oscillating classical force with frequency ω_d [33]. If the force can be derived from the potential $\hat{V}(t) = -F\hat{x}\sin(\omega_d t + \phi)$, the Hamiltonian describing the dynamics is given by

$$\begin{aligned}\hat{H} &= \hbar\omega\left(\hat{a}^\dagger\hat{a} + \frac{1}{2}\right) - F\hat{x}\sin(\omega_d t + \phi) \\ &= \hbar\omega\left(\hat{a}^\dagger\hat{a} + \frac{1}{2}\right) - Fx_0(\hat{a} + \hat{a}^\dagger)\sin(\omega_d t + \phi). \end{aligned} \tag{2.23}$$

Transforming into the interaction picture [29] with respect to $\hat{H}_0 = \hbar\omega\hat{a}^\dagger\hat{a}$ gives

$$\begin{aligned}\hat{H}_I &= e^{i\hat{H}_0 t/\hbar}\hat{V}(t)e^{-i\hat{H}_0 t/\hbar} \\ &= -Fx_0(\hat{a}e^{-i\omega t} + \hat{a}^\dagger e^{i\omega t})\sin(\omega_d t + \phi). \\ &= -\frac{Fx_0}{2i}\left(\hat{a}(e^{i(\omega_d-\omega)t+i\phi} - e^{-i(\omega+\omega_d)t-i\phi}) - \hat{a}^\dagger(e^{i(\omega-\omega_d)t-i\phi} - e^{i(\omega+\omega_d)t-i\phi})\right). \end{aligned} \tag{2.24}$$

where I have used

$$\begin{aligned}e^{\frac{i}{\hbar}\hat{H}_0 t}\hat{a}e^{-\frac{i}{\hbar}\hat{H}_0 t} &= \hat{a}e^{-i\omega t} \\ e^{\frac{i}{\hbar}\hat{H}_0 t}\hat{a}^\dagger e^{-\frac{i}{\hbar}\hat{H}_0 t} &= \hat{a}^\dagger e^{i\omega t}. \end{aligned} \tag{2.25}$$

Provided $\Omega \ll \omega$, where $\Omega = Fx_0/\hbar$, the counter-rotating terms oscillating at $\omega+\omega_d$ can be dropped (rotating-wave approximation) and the interaction Hamiltonian reduces to

$$\hat{H}_I = -\frac{\hbar\Omega}{2i}(\hat{a}e^{-i\delta t+i\phi} - \hat{a}^\dagger e^{i\delta t-i\phi}), \tag{2.26}$$

where the detuning is defined as $\delta \equiv \omega_d - \omega$. It is worth considering the case where the classical drive is tuned onto resonance with the harmonic oscillator ($\omega = \omega_d$). With this condition, the interaction Hamiltonian (Eq. 2.26) commutes with itself at all times and the time evolution operator is given by

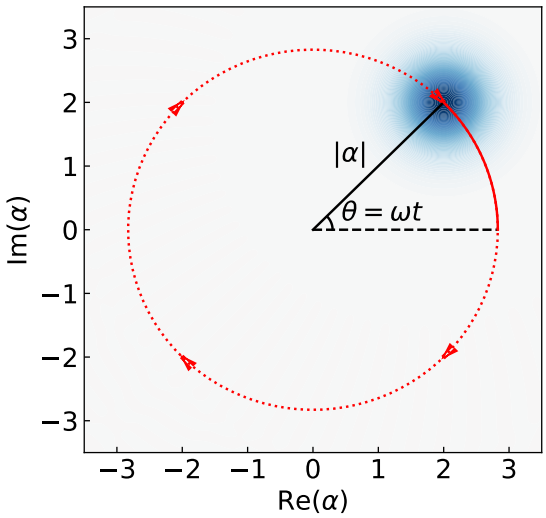

Figure 2.4: Coherent state in the lab frame after applying a resonant drive for a duration $t_d = \frac{2|\alpha|}{\Omega}$ to the ground state. The wavepacket follows circular trajectories with angular frequency ω.

$$\begin{aligned}\hat{U}_I &= \exp\left(-\frac{i}{\hbar}\int_0^t \hat{H}_I(t')dt'\right) \\ &= \exp\left(\frac{\Omega t}{2}(\hat{a}e^{i\phi} - \hat{a}^\dagger e^{-i\phi})\right) \\ &= \hat{D}\left(\frac{\Omega t}{2}e^{-i\phi}\right), \end{aligned} \tag{2.27}$$

where the displacement amplitude $\alpha(t) = \frac{\Omega t}{2}e^{-i\phi}$ depends linearly on the duration t_d the drive is applied. Although the the coherent state has a fixed phase in the interaction picture, in the lab frame $\hat{U}(t_d) = e^{\frac{i}{\hbar}\hat{H}_0 t_d}\hat{U}_I e^{-\frac{i}{\hbar}\hat{H}_0 t_d} = \hat{D}\left(\frac{\Omega t_d}{2}e^{i\omega t_d - i\phi}\right)$ the wavepacket will rotate about the origin in phase space at the frequency ω (Fig 2.4).

What about the validity of the rotating wave approximation? It is straightforward to show that without dropping any fast rotating terms the time evolution operator is (up to an overall phase factor)

$$\hat{U}_I = \hat{D}\left(\frac{\Omega t}{2}e^{-i\phi} - \frac{\Omega}{2\omega}\sin(\omega t)e^{i(\omega t+\phi)}\right), \tag{2.28}$$

which shows that the effect of the counter-rotating terms is to superimpose a circular motion on the

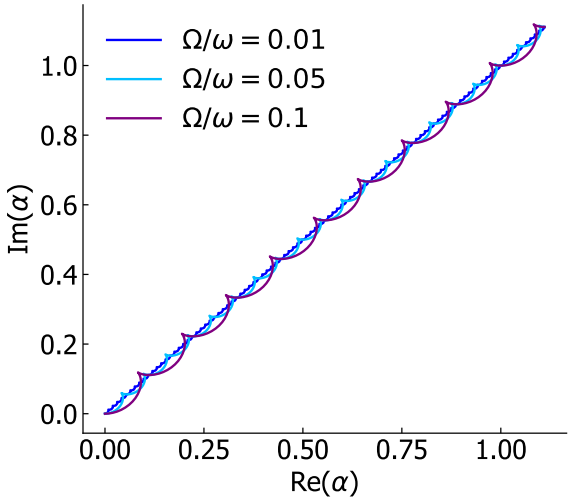

Figure 2.5: Phase space trajectories of $\alpha(t)$, in the interaction frame rotating at ω, for a resonantly driven oscillator without invoking the rotating wave approximation for $\Omega t \in [0, 0.5]$, for various values of Ω/ω.

linearly increasing amplitude. The amplitude of the fast circular motion is suppressed by a factor of Ω/ω (see Fig. 2.5). For the experiments described in this thesis, we typically have $\Omega/\omega \sim 10^{-3}$, allowing us to safely make the rotating wave approximation for all subsequent analysis.

Next I consider the more general case where the driving force is detuned from the oscillator frequency. As Eq. 2.26 does not commute with itself at all times for arbitrary δ, the time evolution operator cannot be derived by direct integration of $\hat{H}_I$. As described in Appendix A, the Magnus expansion method can be used to evaluate the time evolution operator. Since

$$[\hat{H}_I(t), \hat{H}_I(t')] = \hbar^2\Omega^2(\sin(\delta(t - t'))) \tag{2.29}$$

and

$$[[\hat{H}_I(t), \hat{H}_I(t')], \hat{H}_I(t'')] = 0, \tag{2.30}$$

the Magnus expansion terminates at the first order. The time evolution operator is therefore

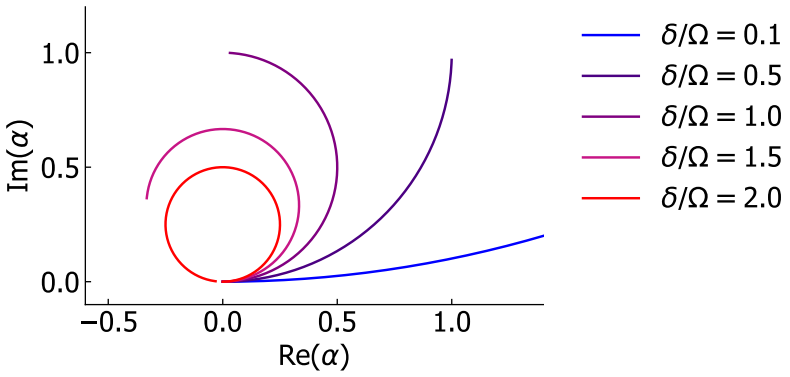

Figure 2.6: Phase space trajectories of $\alpha(t)$, in the interaction frame rotating at ω, for the detuned driven oscillator for $\Omega t/2\pi \in [0, 0.49]$, for various values of $\dfrac{\delta}{\Omega}$ for $\alpha(0) = 0$.

$$\begin{aligned}\hat{U}_I(t) &= \exp\left(-\frac{\Omega}{\delta}\sin\left(\frac{\delta t}{2}\right)\left[\hat{a}e^{-i\delta t/2}e^{i\phi} + \hat{a}^\dagger e^{i\delta t/2}e^{-i\phi}\right]\right) \\ &\times \exp\left(-i\frac{\Omega^2}{\delta^2}[\delta t - \sin(\delta t)]\right) \\ &= \hat{D}(\alpha(t))e^{i\Phi(t)} \end{aligned} \tag{2.31}$$

where the time dependent displacement amplitude is given by

$$\alpha(t) = -\frac{\Omega}{\delta}\sin\left(\frac{\delta t}{2}\right)e^{i\delta t/2}e^{-i\phi}, \tag{2.32}$$

and the geometric phase by

$$\Phi(t) = \frac{\Omega^2}{\delta^2}[\delta t - \sin(\delta t)]. \tag{2.33}$$

From a phase-space perspective, $\alpha(t)$ follows a path along the arc of a circle of diameter $\frac{\Omega}{\delta}$ (Fig. 2.6). The motional state returns to where it started at $t = 0$ every $t_n = \dfrac{2n\pi}{\delta}$ where n is an integer and $n > 0$. The geometric phase $\Phi(t)$ is equal to the area circumscribed by the trajectory and a straight line from the point $\alpha(t)$ back to $\alpha(0) = 0$.

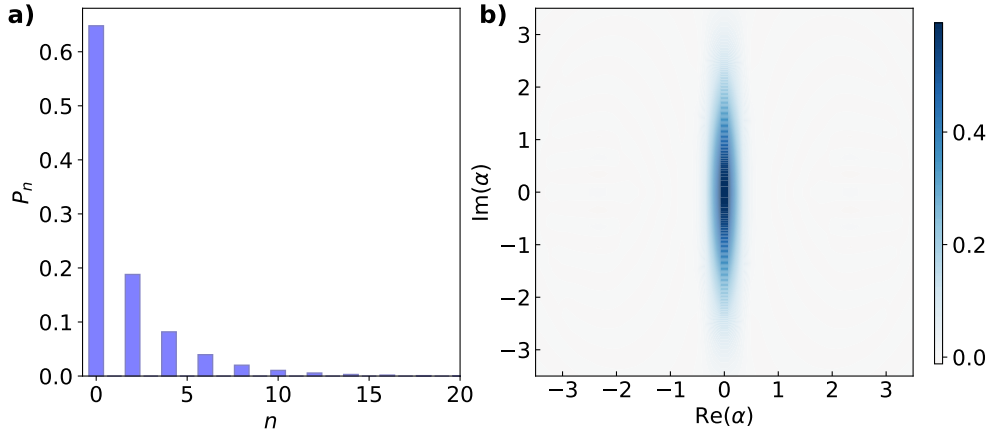

Figure 2.7: a) Number state probabilities and b) Wigner function for a squeezed state with $r = 1$, $\theta = 0$.

2.5 Squeezed states

The previous section described the generation of coherent states of motion by displacing the ground state of an oscillator with a near-resonant force. In the rotating frame at the harmonic oscillator frequency, resonant driving serves to translate the oscillator's wavepacket in phase space, but leaves its shape unchanged. Controllable distortion of the oscillator's wavepacket can be generated using the single-mode squeezing operator defined as

$$\hat{S}(\xi) = e^{\frac{1}{2}(\xi^* \hat{a}^2 - \xi \hat{a}^{\dagger 2})}, \tag{2.34}$$

where $\xi = re^{i\theta}$ is the squeezing parameter. If the squeezing operator is applied to the harmonic oscillator ground state, the resulting state $|\xi\rangle = \hat{S}\,|0\rangle$, is known as a squeezed ground state or squeezed vacuum state. For a squeezed state characterized by the complex squeezing parameter $\xi = re^{i\theta}$, the number state decomposition is given by

$$|\xi\rangle = \frac{1}{\sqrt{\cosh r}} \sum_{n=0}^{\infty} \frac{e^{in\theta}(-\tanh r)^n \sqrt{(2n)!}}{2^n n!} \,|2n\rangle\,, \tag{2.35}$$

showing that the odd Fock state amplitudes are zero (see Fig. 2.7 a). The even number state

populations are given by

$$P_{2n} = \frac{(\tanh r)^{2n}}{\cosh r} \frac{(2n)!}{(2^n n!)^2}. \tag{2.36}$$

The Wigner function for a squeezed ground state is given by [30]

$$W(r, \theta, \alpha) = \frac{2}{\pi} \exp\left(-2e^{2r}\,\mathrm{Re}[e^{-i\theta/2}\alpha]^2 - 2e^{-2r}\,\mathrm{Im}[e^{-i\theta/2}\alpha]^2\right), \tag{2.37}$$

which is a two-dimensional Gaussian function (see Fig. 2.7 b).

The action of the squeezing operator on the annihilation and creation operators yields the Boguliubov transformations [34]:

$$\hat{S}^\dagger(\xi)\hat{a}\hat{S}(\xi) = \quad \hat{a}\cosh r - \hat{a}^\dagger e^{i\theta}\sinh r \tag{2.38}$$

$$\hat{S}^\dagger(\xi)\hat{a}^\dagger\hat{S}(\xi) = \quad \hat{a}^\dagger\cosh r - \hat{a}e^{-i\theta}\sinh r \tag{2.39}$$

Using these expressions, it is easy to show that the expectation value of the number operator $\langle n\rangle = \sinh^2 r$, which shows that the expectation value of the energy grows exponentially with r. Like the ground state, the squeezed ground state is centered on the origin in phase space and the expectation values of the position and momentum operators are zero i.e. $\langle\xi|\hat{x}|\xi\rangle = 0$, and $\langle\xi|\hat{p}|\xi\rangle = 0$. Perhaps the most striking feature of the squeezed state is that the uncertainties along orthogonal phase space quadratures can be very different. The uncertainty in measuring the position is

$$\sigma(\hat{x}) = x_0\sqrt{\frac{e^{2r}(1-\cos\theta)}{2} + \frac{e^{-2r}(1+\cos\theta)}{2}}. \tag{2.40}$$

When $\theta = 0$, $\sigma(\hat{x}) = e^{-r}x_0$, which is smaller than the width of the ground state probability distribution. For $\theta = \pi$, $\sigma(\hat{x}) = e^{r}x_0$, which is larger than the ground state width. Furthermore

$$\sigma(\hat{p}) = p_0\sqrt{\frac{e^{2r}(1+\cos\theta)}{2} + \frac{e^{-2r}(1-\cos\theta)}{2}}, \tag{2.41}$$

and the uncertainty product is given by

$$\sigma(\hat{x})\sigma(\hat{p}) = \frac{\hbar}{2}\sqrt{1+\frac{1}{2}(\cosh 4r - 1)\sin^2\theta} \tag{2.42}$$

which is equal to $\hbar/2$ when $\theta = n\pi$, for $n = 0, 1, 2....$ As the squeezed state can saturate the Heisenberg uncertainty relation, it is also a minimum uncertainty state.

2.6 Parametric modulation

The squeezing operator described in the previous section can be implemented by modulating the curvature of the potential of the quantum oscillator at twice its natural frequency. To see how this arises, consider the Hamiltonian given by

$$\begin{aligned}\hat{H} &= \frac{\hat{p}^2}{2m} + \frac{1}{2}m\omega^2\hat{x}^2 - \hbar g\sin(\omega_p t - \theta)\left(\frac{\hat{x}}{x_0}\right)^2, \\ &= \hbar\omega\left(\hat{a}^\dagger\hat{a} + \frac{1}{2}\right) - \hbar g\sin(\omega_p t - \theta)(\hat{a}^{\dagger 2} + \hat{a}^2 + 2\hat{a}^\dagger\hat{a} + 1),\end{aligned} \tag{2.43}$$

where ω_p is the modulation frequency, g is the parametric modulation strength, θ is the phase of the modulation drive. Transforming into the interaction picture with respect to the bare ($g = 0$) harmonic oscillator Hamiltonian gives the interaction Hamiltonian

$$\hat{H}_I = -\hbar g\sin(\omega_p t - \theta)(\hat{a}^{\dagger 2}e^{2i\omega_r t} + \hat{a}^2 e^{-2i\omega_r t} + 2\hat{a}^\dagger\hat{a} + 1). \tag{2.44}$$

If we make the rotating wave approximation by neglecting terms oscillating at $\pm(2\omega_r + \omega_p)$ and ω_p, $\hat{H}_I$ reduces to

$$\hat{H}_I = -\hbar\frac{g}{2i}\left(\hat{a}^2 e^{-2i\omega_r t + i\omega_p t - i\theta} - \hat{a}^{\dagger 2}e^{2i\omega_r t - i\omega_p t + i\theta}\right). \tag{2.45}$$

If $\omega_p = 2\omega_r$,

$$\hat{H}_I = i\hbar\frac{g}{2}(\hat{a}^2 e^{-i\theta} - \hat{a}^{\dagger 2}e^{i\theta}), \tag{2.46}$$

which is the Hamiltonian describing degenerate parametric amplification of a single-mode boson field [35]. If this Hamiltonian is applied for a duration t, the time evolution operator $\hat{U}(t)$ in the frame rotating at ω is

$$\hat{U}(t) = e^{\frac{-i\hat{H}_I t}{\hbar}} = e^{\frac{gt}{2}(\hat{a}^2 e^{-i\theta} - \hat{a}^{\dagger 2} e^{i\theta})}. \tag{2.47}$$

Paramteric modulation therefore implements a squeezing operator $\hat{S}(\xi)$ with squeezing parameter $\xi = gte^{i\theta}$.

2.7 Displaced squeezed states

Displacement and squeezing operations can combined to make more complicated states. For a state that is prepared by first squeezing the ground state with squeezing parameter ξ and then displaced by α, the state vector is given by

$$|\xi, \alpha\rangle = \hat{D}(\alpha)\hat{S}(\xi)\,|0\rangle\,, \tag{2.48}$$

and the probabilities of finding the oscillator in a given number state are [30]

$$\begin{aligned} P_n &= |\,\langle n|\alpha,\xi\rangle\,|^2 = \frac{(\frac{1}{2}\tanh r)^n}{n!\cosh r}\left|H_n\left(\frac{\alpha\cosh r + \alpha^* e^{i\theta}\sinh r}{\sqrt{e^{i\theta}\sinh(2r)}}\right)\right|^2 \\ &\quad \times \exp\left[-|\alpha|^2 - \frac{1}{2}(\alpha^{*2}e^{i\theta} + \alpha^2 e^{-i\theta})\tanh r\right], \end{aligned} \tag{2.49}$$

where H_n are Hermite polynomials. The number state probability distribution and Wigner function for a particular displaced squeezed state are shown in Fig. 2.8.

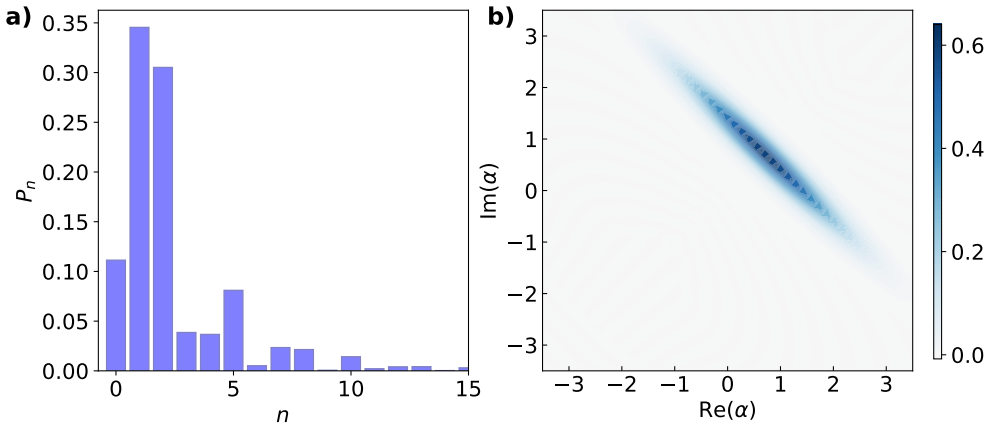

Figure 2.8: a) Number state probabilities and b) Wigner function for a state that is first squeezed with $r = 1.0$, and the displaced with $|\alpha| = 1$.

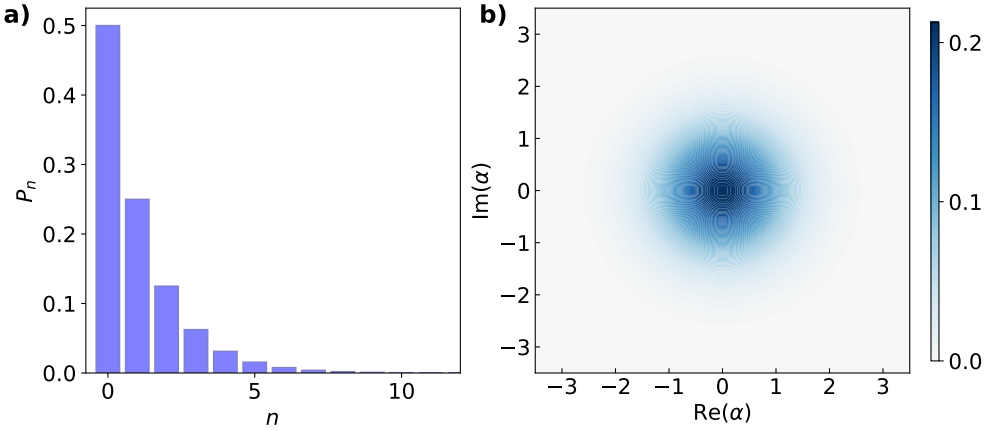

Figure 2.9: a) Number state probabilities and b) Wigner function for a thermal distribution with $\bar{n} = 1.0$.

2.8 Thermal distribution

The states described in the previous sections are pure quantum states. In experimentally relevant situations, the oscillator will have some degree of coupling with its environment, and after an extended period of time will tend to reach thermal equilibrium with its surroundings. The oscillator will then be in a mixed state with a density matrix given by [29]

$$\hat{\rho}_{th} = \frac{e^{-\beta \hat{H}}}{Z} \tag{2.50}$$

where Z is the partition function and $\beta = 1/k_B T$. As described in Appendix B, for a one dimensional harmonic oscillator

$$\hat{\rho}_{th} = (1 - e^{-\hbar\omega_z \beta}) \sum_{n=0}^{\infty} e^{-\beta \hbar \omega_z n} \left|n\right\rangle \left\langle n\right| . \tag{2.51}$$

In typical ion trapping experiments, the quantity that can be measured is $\bar{n} = \mathrm{Tr}[\hat{\rho}_{th}\hat{n}]$, which is related to the temperature T by

$$T = \frac{\hbar\omega_z}{k_B} \frac{1}{\ln[\frac{\bar{n}}{1+\bar{n}}]}. \tag{2.52}$$

Substituting into 2.51 gives

$$\hat{\rho}_{th} = \frac{1}{\bar{n}+1} \sum_{n=0}^{\infty} \left(\frac{\bar{n}}{1+\bar{n}} \right)^n |n\rangle \langle n| \tag{2.53}$$

and thus the probabilities for finding the oscillator in a given number state (Fig. 2.9 a) are given by

$$P_n = \frac{1}{\bar{n}+1} \left(\frac{\bar{n}}{1+\bar{n}} \right)^n. \tag{2.54}$$

The Wigner function of the thermal state is given by[32]

$$W(\bar{n}, \alpha) = \frac{2}{\pi} \frac{1}{1+2\bar{n}} e^{-2|\alpha|^2/(1+2\bar{n})}, \tag{2.55}$$

which describes a circular Gaussian in phase space, but with a larger width than that of a coherent state (Fig. 2.9 b).

Chapter 3

Spins and Springs

Trapped ions have been used to construct the world's most accurate atomic clock [36] and for pioneering experiments in quantum information processing [4], and quantum simulation [24, 37, 38]. For these and other experiments, controllable couplings between the ions' motion and internal electronic states are essential.

In this chapter, I describe the theory of coupling two-level systems or "spins" and harmonic oscillators. In addition to providing a powerful method for harmonic oscillator state analysis, spin-motion coupling is also required for resolved-sideband cooling, and for implementing spin-dependent forces that can be used to generate interesting non-classical states such as Schrödinger-cat states and squeezed cat states. Moreover, spin-dependent forces are essential for generating high-fidelity entanglement between trapped-ion qubits.

3.1 Harmonically confined spins

Consider a two-level system (TLS) with an energy splitting of $\hbar\omega_0$ (see Fig. 3.1) and energy eigenstates denoted by $|\uparrow\rangle$ and $|\downarrow\rangle$. It is convenient to represent the TLS as a spin 1/2 system. If a static magnetic field $B_s\vec{e}_z$ applied to define the quantization axis, the Hamiltonian for such a system, up to an additive constant is given by

$$\hat{H} = \frac{\hbar\omega_0}{2}\hat{\sigma}_z, \tag{3.1}$$

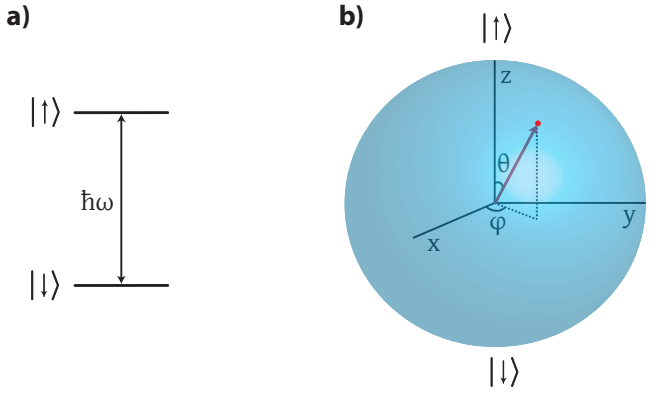

Figure 3.1: The spin. a) Two levels with energy separation $\hbar\omega$ with energy eigenstates $|\downarrow\rangle$ and $|\uparrow\rangle$. b) Bloch sphere representation of the quantum state of a two-level system. A pure state is represented by a point (red dot) on the surface of the sphere

where $\hat{\sigma}_z = |\uparrow\rangle\langle\uparrow| - |\downarrow\rangle\langle\downarrow|$ is a Pauli operator. A pure state of the TLS can be represented as a point on the Bloch sphere (Fig. 3.1 b) given by

$$|\Psi\rangle = \cos\left(\frac{\theta}{2}\right)|\downarrow\rangle + e^{i\phi}\sin\left(\frac{\theta}{2}\right)|\uparrow\rangle\,. \tag{3.2}$$

If the TLS is harmonically confined in one spatial dimension, the Hamiltonian, up to an additive constant, becomes

$$\hat{H}_0 = \frac{\hbar\omega_0}{2}\hat{\sigma}_z + \hbar\omega\hat{a}^\dagger\hat{a}. \tag{3.3}$$

This can be visualized as each spin state being associated with a set of harmonic oscillator energy levels (Fig. 3.2). In a trapped-ion system there is typically no significant intrinsic coupling between the internal states of the ion and its harmonic oscillator states. However, they can be coupled together by applying external electric or magnetic field gradients. Here I describe the essential physics of the latter and leave details of the experimental implementation for Chapter 4

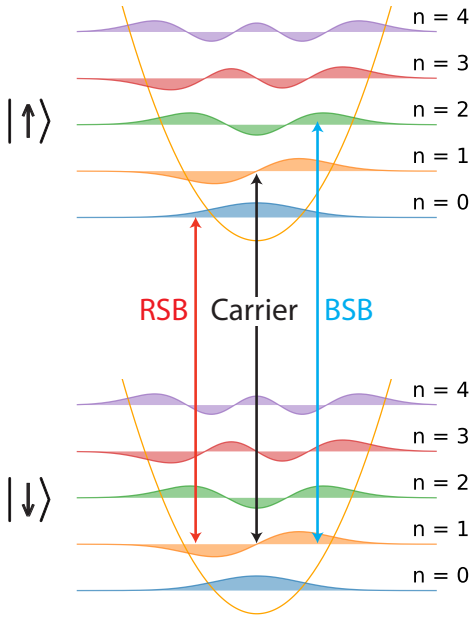

Figure 3.2: Energy levels and transitions of a harmonically confined two-level system. The red sideband (RSB) induces transitions from $|\downarrow\rangle|n\rangle \leftrightarrow |\uparrow\rangle|n-1\rangle$. The blue sideband (BSB) induces transitions from $|\downarrow\rangle|n\rangle \leftrightarrow |\uparrow\rangle|n+1\rangle$. Carrier transitions change the spin state but leave the motional state unchanged.

3.2 Spin-motion coupling

We now subject the harmonically confined ion to a sinusoidally oscillating magnetic field

$$\vec{B} = (B_x\vec{e}_x + B_y\vec{e}_y + B_z\vec{e}_z)\cos(\omega_d t + \phi), \tag{3.4}$$

where ω_d and ϕ are the drive frequency and phase respectively. As described below, the spin can be coupled to the oscillator provided the components of $\vec{B}$ vary appropriately in space [1] . The oscillating field results in the Hamiltonian

$$\hat{V}(t) = -\hat{\vec{\mu}} \cdot \vec{B}(t). \tag{3.5}$$

where $\vec{\mu}$ is the dipole moment operator of the TLS. Two relevant situations arise depending on the difference Δm of the projection of the total angular momentum of the ion on the quantization axis between the $|\downarrow\rangle$ and $|\uparrow\rangle$ states. For $\Delta m = 0$,

$$\hat{V}(t) = -(\mu_{||}\hat{\sigma}_x + \mu_z\hat{\sigma}_z + \mu_I\hat{I})B_z\cos(\omega_d t + \phi). \tag{3.6}$$

The first term describes transitions between $|\downarrow\rangle$ and $|\uparrow\rangle$ when a π polarized field (where the direction of oscillation of the magnetic field is parallel to the quantization axis) is applied to the ion. The second term is a time varying frequency shift of the TLS, where the transition energy is periodically modulated due to the difference in magnetic dipole moments (μ_z) of the two states. The last term (where $\hat{I}$ is the 2×2 identity operator) represents the common shift of the levels and does not affect the dynamics. This term will be neglected in later discussions. For the case where $\Delta m = \pm 1$

$$V(t) = -(\mu_\perp(\hat{\sigma}_x B_x + \hat{\sigma}_y B_y) + \mu_z\hat{\sigma}_z B_z + \mu_I\hat{I})\cos(\omega_d t + \phi), \tag{3.7}$$

where now the transverse components of the magnetic field drive transitions between $|\downarrow\rangle$ and $|\uparrow\rangle$. The remaining terms result in a time varying frequency shift as in the $\Delta m = 0$ case. We will now

[1] Spin-motion coupling can also be achieved using static magnetic field gradients [39]

focus on the $\Delta m = 0$ case, and return to the $\Delta m = \pm 1$ case later in the chapter. The z component of the magnetic field can be Taylor expanded along the direction of the unit vector $\vec{q}$ that is parallel to the direction of oscillation of a normal mode of motion. The displacement from equilibrium is described by the operator $\hat{q} = q_0(\hat{a} + \hat{a}^\dagger)$, where $q_0 = \sqrt{\frac{\hbar}{2m\omega}}$, to give $B_z = (B_{z0} + (\nabla B.\vec{q})\hat{q} + ...)$. Higher-order contributions to the Taylor expansion are assumed to be negligible. Furthermore we will assume that the differential magnetic moment $\mu_z = 0$ (these assumptions will be justified in Chapter 4). The Hamiltonian describing the oscillating field can then be written as

$$\hat{V}(t) = -\mu_{||}\left[B_{z0} + (\nabla B.\vec{q})q_0(\hat{a} + \hat{a}^\dagger)\right]\hat{\sigma}_x \cos(\omega_d t + \phi) \tag{3.8}$$

and the combined Hamiltonian for the harmonically confined spin in the oscillating magnetic field is then

$$\begin{aligned} \hat{H} &= \hat{H}_0 + \hat{V}(t) \\ &\simeq \frac{\hbar\omega_0}{2}\hat{\sigma_z} + \hbar\omega\hat{a}^\dagger\hat{a} - \mu_{||}\left[B_{z0} + (\nabla B.\vec{q})q_0(\hat{a} + \hat{a}^\dagger)\right]\hat{\sigma}_x \cos(\omega_d t + \phi). \end{aligned} \tag{3.9}$$

Insight into the dynamics resulting from Eq. 3.9 can be gained by transforming into the interaction picture where

$$\hat{H}_I = e^{\frac{i}{\hbar}\hat{H}_0 t}\hat{V}(t)e^{-\frac{i}{\hbar}\hat{H}_0 t}. \tag{3.10}$$

Using the Baker-Campbell-Hausdorff formula [29] we obtain

$$e^{\frac{i}{\hbar}\hat{H}_0 t}\hat{\sigma}_+ e^{-\frac{i}{\hbar}\hat{H}_0 t} = \hat{\sigma}_+ e^{i\omega_0 t} \tag{3.11}$$

$$e^{\frac{i}{\hbar}\hat{H}_0 t}\hat{\sigma}_- e^{-\frac{i}{\hbar}\hat{H}_0 t} = \hat{\sigma}_- e^{-i\omega_0 t}. \tag{3.12}$$

and we can write the interaction Hamiltonian as

$$\begin{aligned}\hat{H}_I &= -\hbar\Omega_0(\hat{\sigma}_+ e^{i\omega_0 t} + \hat{\sigma}_- e^{-i\omega_0 t})\cos(\omega_d t + \phi) \\ &\quad -\hbar\Omega(\hat{\sigma}_+ e^{i\omega_0 t} + \hat{\sigma}_- e^{-i\omega_0 t})(\hat{a}e^{-i\omega t} + \hat{a}^\dagger e^{+i\omega t})\cos(\omega_d t + \phi) \end{aligned} \tag{3.13}$$

where

$$\Omega_0 \equiv \frac{\mu_{||} B_{z0}}{\hbar} \tag{3.14}$$

and,

$$\Omega \equiv \frac{\mu_{||} q_0 B'}{\hbar}, \tag{3.15}$$

where $B' \equiv \nabla B.\vec{q}$. In the experiments described in this thesis, we typically operate in a regime where $\omega_0, \omega_d \gg \omega$, and $|\omega_0 + \omega_d| \gg |\omega - \omega_d|$. Terms oscillating at $\pm(\omega_0 + \omega_d)$ in Equation 3.13 can safely be dropped (rotating-wave approximation) and the interaction Hamiltonian becomes

$$\begin{aligned}\hat{H}_I &= -\frac{\hbar}{2}(\hat{\sigma}_+ e^{i(\omega_0-\omega_d)t - i\phi} + \hat{\sigma}_- e^{-i(\omega_0-\omega)t + i\phi}) \\ &\quad \times \left[\Omega_0 + \Omega(\hat{a}e^{-i\omega t} + \hat{a}^\dagger e^{+i\omega t})\right]. \end{aligned} \tag{3.16}$$

There are three particular choices of ω_d that are worth describing in detail.

i) Carrier interaction

If the drive is tuned close to the qubit frequency so that $|\omega_0 - \omega_d| \ll \omega$, and $\Omega \ll \omega$, the terms depending on the motion will be off-resonant and can be dropped, and the interaction Hamiltonian can be written as

$$\hat{H}_I \rightarrow \hat{H}_C = -\frac{\hbar\Omega_0}{2}(\hat{\sigma}_+ e^{i\delta t - i\phi} + \hat{\sigma}_- e^{-i\delta t + i\phi}), \tag{3.17}$$

where the detuning $\delta = \omega_0 - \omega_d$. On resonance ($\delta = 0$), $\hat{H}_C = -\frac{\hbar\Omega_0}{2}(\cos(\phi)\hat{\sigma}_x + i\sin(\phi)\hat{\sigma}_y)$. This Hamiltonian will generate rotations about an axis in the equatorial plane of the Bloch sphere (Fig. 3.1 b). $\hat{H}_C$ therefore induces carrier transitions $|\downarrow\rangle|n\rangle \leftrightarrow |\uparrow\rangle|n\rangle$, which change the spin state, but leave the oscillator state unchanged. This is illustrated in Figs. 3.2 and 3.3.

ii) Red sideband interaction

If the homogeneous part of the magnetic field is negligible ($B_{z0} = 0$), and $\Omega \ll \omega$, tuning ω_d near $\omega_0 - \omega$ gives

$$\hat{H}_I \rightarrow \hat{H}_{RSB} = \frac{\hbar\Omega}{2}(\hat{\sigma}_+\hat{a}e^{i\delta t - i\phi} + \hat{\sigma}_-\hat{a}^\dagger e^{-i\delta t + i\phi}), \tag{3.18}$$

where $\delta = \omega_0 - \omega_d - \omega$. $\hat{H}_{RSB}$ is known as the red-sideband interaction. It is also formally equivalent to the Jaynes-Cummings Hamiltonian for an atom coupled to a single electromagnetic field mode in a cavity [30]. To get a feel for this Hamiltonian consider the case where $\delta = 0$. The time evolution of the state $|n\rangle|\uparrow\rangle$ generated by $\hat{H}_{RSB}$ is given by

$$\begin{aligned}
|\psi(t)\rangle &= e^{-\frac{i}{\hbar}\hat{H}_{RSB}t}|n\rangle|\uparrow\rangle \\
&= \sum_{n=0}^{\infty}\left[\frac{(-1)^n}{(2n)!}\left(\frac{\sqrt{n+1}\Omega t}{2}\right)^{2n}|n\rangle|\uparrow\rangle - ie^{-i\phi}\frac{(-1)^n}{(2n+1)!}\left(\frac{\sqrt{n+1}\Omega t}{2}\right)^{2n+1}|n+1\rangle|\downarrow\rangle\right] \\
&= \cos\left(\frac{\sqrt{n+1}\Omega t}{2}\right)|n\rangle|\uparrow\rangle - ie^{-i\phi}\sin\left(\frac{\sqrt{n+1}\Omega t}{2}\right)|n+1\rangle|\downarrow\rangle,
\end{aligned} \tag{3.19}$$

which describes Rabi oscillations between states $|n\rangle|\uparrow\rangle$ and $|n+1\rangle|\downarrow\rangle$ with Rabi frequency $\sqrt{n+1}\Omega$ (Fig. 3.3). Note that the $|0\rangle|\downarrow\rangle$ state is an eigenstate of $\hat{H}_{RSB}$ with eigenvalue 0, therefore $e^{-\frac{i}{\hbar}\hat{H}_{RSB}t}|0\rangle|\downarrow\rangle = |0\rangle|\downarrow\rangle$ for all t . This property is exploited in resolved sideband cooling (see Chapter 4), which enables cooling of an oscillator close to its motional ground state [40, 41].

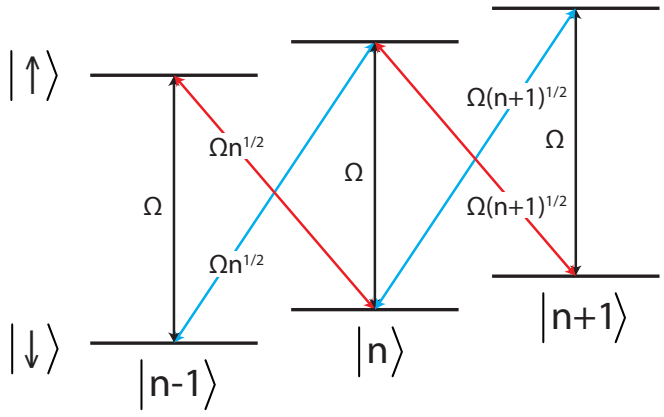

Figure 3.3: Energy levels of a harmonically confined qubit (not to scale). Carrier transitions indicated by black arrows change the qubit state, but leave the oscillator state unchanged. Blue and red sideband transitions, depicted as appropriately colored arrows, change both the qubit and motional state. Rabi frequencies for sideband transitions are indicated on the transition arrows.

iii) Blue sideband interaction

If the drive frequency is tuned close to the sum of the qubit and motional frequencies $\omega_d = \omega_0 + \omega$, with the restriction $\Omega \ll \omega$,

$$\hat{H}_I \rightarrow \hat{H}_{BSB} = \frac{\hbar\Omega}{2}(\hat{\sigma}_+ \hat{a}^\dagger e^{i\delta t - i\phi} + \hat{\sigma}_- \hat{a} e^{-i\delta t + i\phi}), \tag{3.20}$$

where $\delta = \omega_0 - \omega_d + \omega$. $\hat{H}_{BSB}$ is the blue-sideband or the anti-Jaynes Cummings interaction. For the case where $\delta = 0$, the state $|n\rangle|\downarrow\rangle$ evolves into

$$\begin{aligned} |\psi(t)\rangle &= e^{-\frac{i}{\hbar}\hat{H}_{BSB}t}|n\rangle|\downarrow\rangle \\ &= \sum_{n=0}^{\infty}\left[\frac{(-1)^n}{(2n)!}\left(\frac{\sqrt{n+1}\Omega t}{2}\right)^{2n}|n\rangle|\downarrow\rangle - ie^{-i\phi}\frac{(-1)^n}{(2n+1)!}\left(\frac{\sqrt{n+1}\Omega t}{2}\right)^{2n+1}|n+1\rangle|\uparrow\rangle\right] \\ &= \cos\left(\frac{\sqrt{n+1}\Omega t}{2}\right)|n\rangle|\downarrow\rangle - ie^{-i\phi}\sin\left(\frac{\sqrt{n+1}\Omega t}{2}\right)|n+1\rangle|\uparrow\rangle\,. \end{aligned} \tag{3.21}$$

So the blue sideband induces transitions between the $|n\rangle|\downarrow\rangle$ and $|n+1\rangle|\uparrow\rangle$ states. The probability

of measuring the spin state $|\downarrow\rangle$ after applying $\hat{H}_{BSB}$ for a duration t is given by

$$P_{\downarrow}(t) = |\langle\downarrow|\psi(t)\rangle|^2 = \cos^2\left(\frac{\sqrt{n+1}\Omega t}{2}\right), \tag{3.22}$$

which describes Rabi oscillations with a frequency $\sqrt{n+1}\Omega$. If the oscillator is prepared in a superposition of number states before the blue sideband is applied

$$\begin{aligned}|\psi(t)\rangle &= e^{-\frac{i}{\hbar}\hat{H}_{BSB}t}\sum_{n=0}^{\infty} c_n |n\rangle|\downarrow\rangle \\ &= \sum_{n=0}^{\infty} c_n \cos\left(\frac{\sqrt{n+1}\Omega t}{2}\right)|n\rangle|\downarrow\rangle - ie^{-i\phi}\sum_{n=0}^{\infty} c_{n+1}\sin\left(\frac{\sqrt{n+1}\Omega t}{2}\right)|n+1\rangle|\uparrow\rangle,\end{aligned} \tag{3.23}$$

and the probability of measuring $|\downarrow\rangle$ is given by

$$P_{\downarrow}(t) = \sum_{n=0}^{\infty} P_n \cos^2\left(\frac{\sqrt{n+1}\Omega t}{2}\right), \tag{3.24}$$

where the $P_n = |c_n|^2$ are the probabilities of finding the harmonic oscillator in state $|n\rangle$ before applying the BSB drive. It is straightforward to show that Eq. 3.24 also holds if the oscillator state is initially in a mixed state described by the density matrix $\hat{\rho} = \sum_{n=0,m=0}^{\infty}\rho_{nm}|n\rangle\langle m|$. $P_{\downarrow}(t)$ contains different frequency components weighted according to P_n. Therefore P_n for an unknown oscillator state can be determined by Fourier transforming $P_{\downarrow}(t)$ [19].

Sequences of sideband and carrier interactions can also be used to prepare number states of the harmonic oscillator [19, 42]. For example, starting in the state $|\downarrow\rangle|0\rangle$ and applying $\hat{H}_{BSB}$ for time $t = \pi/\Omega$ generates $|\uparrow\rangle|n=1\rangle$. A carrier π pulse then gives $|\downarrow\rangle|1\rangle$. This sequence of BSB π pulses (with appropriately chose interaction durations) and carrier π pulses can be repeated to generate $|\downarrow\rangle|n\rangle$.

3.3 Spin-dependent forces

The next family of spin-motion coupling interactions that we consider are spin-dependent forces. These interactions are used to generate non-classical harmonic oscillator states and to

implement geometric-phase gates. A spin-dependent force that acts in a spin basis on the equator of the Bloch sphere can be implemented by simultaneously applying a blue and a red sideband [43]. The frequencies of the sideband drives are set to $\omega_d = \omega_0 + \omega + \delta$ and $\omega_d = \omega_0 - \omega - \delta$ for the blue and red sideband respectively. If the sidebands have equal Rabi frequencies, the resulting Hamiltonian after making the RWA, is given by

$$\begin{aligned} \hat{H}_{SDF} &= \frac{\hbar\Omega}{2}\left(\hat{\sigma}_+\hat{a}e^{i\delta t+i\phi} + \hat{\sigma}_-\hat{a}^\dagger e^{-i\delta t-i\phi}\right) + \frac{\hbar\Omega}{2}\left(\hat{\sigma}_-\hat{a}e^{i\delta t+i\phi} + \hat{\sigma}_+\hat{a}^\dagger e^{-i\delta t-i\phi}\right) \\ &= \frac{\hbar\Omega}{2}\hat{\sigma}_\phi(\hat{a}e^{+i\delta t} + \hat{a}^\dagger e^{-i\delta t}), \end{aligned} \tag{3.25}$$

where $\hat{\sigma}_\phi = \cos\phi\hat{\sigma}_x - i\sin\phi\hat{\sigma}_y$. For the remainder of this chapter, the phase ϕ plays no role, so I will set it to 0. If this Hamiltonian is applied on resonance ($\delta = 0$), the time evolution operator is equivalent to a spin-dependent displacement operator

$$\hat{U}(t) = e^{-i\frac{\Omega t}{2}\hat{\sigma}_x(\hat{a}+\hat{a}^\dagger)} = \hat{D}\left(\alpha(t)\hat{\sigma}_x\right), \tag{3.26}$$

where $\alpha(t) = -i\dfrac{\Omega t}{2}$ is the time-dependent displacement amplitude. If the system is initially prepared in $|\downarrow\rangle|n\rangle = \dfrac{1}{\sqrt{2}}(|+\rangle - |-\rangle)|n\rangle$, where $|\pm\rangle$ are the eigenstates of $\hat{\sigma}_x$, the resulting state is

$$|\psi(t)\rangle = \frac{1}{\sqrt{2}}\left[\hat{D}(\alpha(t))|n\rangle|+\rangle - \hat{D}(-\alpha(t))|n\rangle|-\rangle\right], \tag{3.27}$$

which shows that the $|+\rangle$ and $|-\rangle$ spin states are displaced in opposite directions in phase space. If the oscillator is initially prepared in $|0\rangle$, this coherent superposition of separated oscillator wavepackets is sometimes called a Schrödinger-cat state [32, 44]. The Wigner function (Fig.3.4) shows interference fringes with regions of negative quasi probability—a signature of the nonclassical nature of the cat state. These features have been termed sub-Planck structure [45] and can be much narrower than the ground state wave function extent allowing cat states and variations of cat states to be used for quantum-enhanced metrology [46, 47]. If a measurement is made on the

spin state, the probability of finding the system in the $|\downarrow\rangle$ state is given by

$$P_{\downarrow} = \frac{1}{2}\left[1 + \langle n|\hat{D}(2\alpha(t))|n\rangle\right]. \tag{3.28}$$

From Appendix C, the matrix element $\langle n|\hat{D}(\alpha)|n\rangle = e^{-|\alpha|^2/2}\mathcal{L}_n(|\alpha|^2)$. Substituting into 3.32 gives

$$P_{\downarrow} = \frac{1}{2}\left[1 + e^{-2|\alpha(t)|^2}\mathcal{L}_n(|2\alpha(t)|^2)\right]. \tag{3.29}$$

Using the generating function for the Laguerre polynomials (see Appendix C), $P_{\downarrow}(t)$ for a system initially prepared in a thermal distribution with motional occupation $\bar{n}$ is given by

$$P_{\downarrow,th} = \frac{1}{2}\left[1 + e^{-4(\bar{n}+1/2)|\alpha(t)|^2}\right]. \tag{3.30}$$

Figure 3.5 shows $P_{\downarrow}$ for various values of n and $\bar{n}$ for the initial oscillator state. For pure number states, $P_{\downarrow}(t)$ drops faster than for the ground state and there are clear oscillations, resulting from the phase space structure of Fock states (see Fig.2.2), before $P_{\downarrow}$ settles at 0.5. For thermal distributions, the oscillations are damped out from the contributions of multiple Lageurre polynomials of different orders to $P_{\downarrow}$. Note that the thermal distribution approaches $P_{\downarrow} = 1/2$ faster than the ground state despite the fact that the thermal state has a larger phase space width than the ground state. This is because $P_{\downarrow}$ for a thermal distribution is the average of $P_{\downarrow}$ taken over a distribution of number states; and the higher number states have a faster initial decay.

Next we consider the case where the oscillator is prepared in a squeezed number state. After applying the SDF, the state is given by

$$|\psi(t)\rangle = \frac{1}{\sqrt{2}}\left[\hat{D}(\alpha(t))\hat{S}(\xi)\,|n\rangle\,|+\rangle - \hat{D}(-\alpha(t))\hat{S}(\xi)\,|n\rangle\,|-\rangle\right], \tag{3.31}$$

which is known as a squeezed cat state. An example Wigner function, where the initial squeezing is in the same direction as the displacement, is shown in Fig. 3.6. The sub-Planck structure is stretched out along the anti-squeezed axis. This highlights another way of thinking about squeezing:

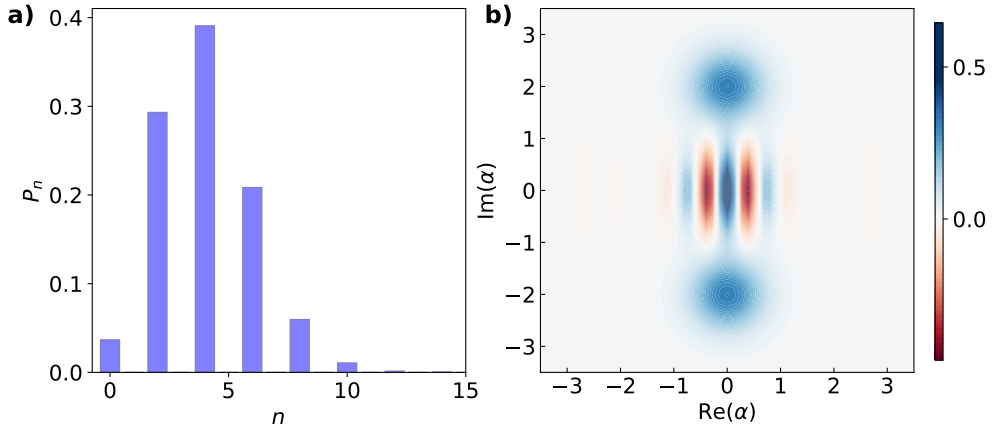

Figure 3.4: a) Number state probabilities and b) Wigner function for the cat state $\frac{1}{\sqrt{2}}(|\alpha\rangle + |-\alpha\rangle)$ with $\alpha = 2i$.

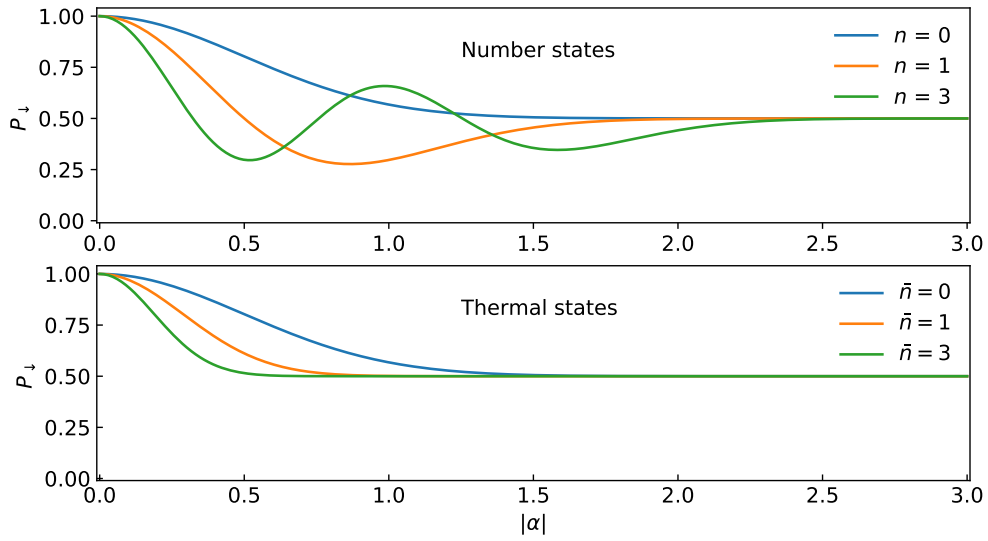

Figure 3.5: $P_\downarrow$ as a function of the spin dependent force displacement amplitude $|\alpha|$ for systems prepared in pure number states (Eq. 3.29) and thermal distributions (Eq. 3.30)

instead of visualizing squeezing as a distortion of the wavepacket, one can instead think of all of phase space being compressed in one phase-space quadrature and stretched in the orthogonal quadrature.

As squeezing redistributes quantum uncertainty between orthogonal quadratures, we expect $P_\downarrow$ given by

$$P_\downarrow = \frac{1}{2}\left[1 + \langle n|\hat{S}^\dagger(\xi)\hat{D}(2\alpha(t))\hat{S}(\xi)|n\rangle\right], \tag{3.32}$$

to depend both on the squeezing angle and on the direction of the SDF. Applying Eq. 2.39,

$$\begin{aligned}\hat{S}^\dagger(\xi)\hat{D}(\beta)\hat{S}(\xi) &= \hat{S}^\dagger(\xi)e^{\beta\hat{a}^\dagger - \beta^*\hat{a}}\hat{S}(\xi) \\ &= \hat{D}(\beta\cosh r + \beta^* e^{i\theta}\sinh r).\end{aligned} \tag{3.33}$$

The matrix element can now be evaluated using the results from Appendix C,

$$\begin{aligned}\langle n|\,\hat{D}(\beta\cosh r + \beta^* e^{i\theta}\sinh r)\,|n\rangle &= \mathcal{L}_n(|\beta\cosh r + \beta^* e^{i\theta}\sinh r|^2)e^{-\frac{1}{2}|\beta\cosh r + \beta^* e^{i\theta}\sinh r)|^2} \\ &= \mathcal{L}_n(|\beta|^2(e^{2r}\cos^2(\phi-\theta/2) + e^{-2r}\sin^2(\phi-\theta/2))) \\ &\quad \times e^{-|\beta|^2(e^{2r}\cos^2(\phi-\theta/2)+e^{-2r}\sin^2(\phi-\theta/2))/2},\end{aligned} \tag{3.34}$$

where $\mathcal{L}_n(x)$ is a Laguerre polynomial and $\beta \equiv |\beta|e^{i\phi}$. Replacing β with 2α gives

$$\begin{aligned}P_\downarrow &= \frac{1}{2}(1 + \mathcal{L}_n(|2\alpha|^2(e^{2r}\cos^2(\phi-\theta/2) + e^{-2r}\sin^2(\phi-\theta/2))) \\ &\quad \times e^{-2|\alpha|^2[e^{2r}\cos^2(\phi-\theta/2)+e^{-2r}\sin^2(\phi-\theta/2)]})\end{aligned} \tag{3.35}$$

For the special case where the ion is initially in the ground state,

$$P_{\downarrow,n=0} = \frac{1}{2}\left(1 + e^{-2|\alpha|^2[e^{2r}\cos^2(\phi-\theta/2)+e^{-2r}\sin^2(\phi-\theta/2)]}\right) \tag{3.36}$$

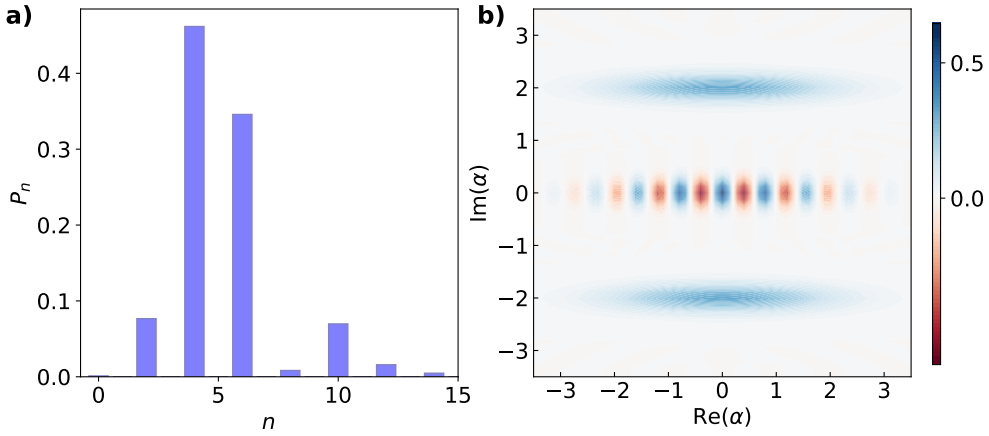

Figure 3.6: a) Number state probabilities and b) Wigner function for a squeezed cat state with $\xi = -1.0$ and $\alpha = 2i$

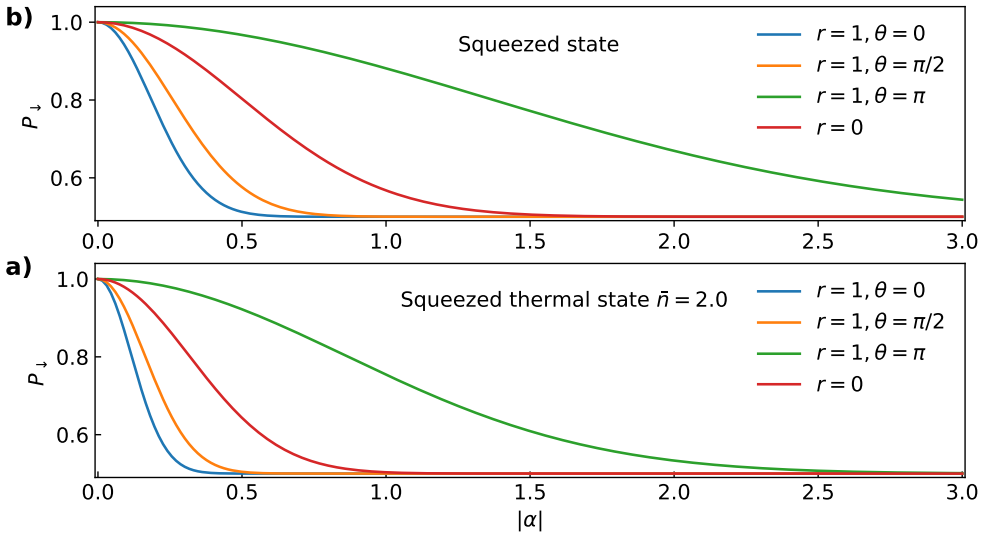

Figure 3.7: $P_\downarrow$ as a function of $|\alpha|$ for a squeezed states with $r = 1.0$, and various values of the squeezing phase θ, and for different initial thermal occupations ($\bar{n} = 0$ upper panel, $\bar{n} = 0$ lower panel). The relative angle of the SDF $\phi = 0$. For comparison, the unsqueezed state ($r = 0$) is also shown.

$P_\downarrow$ depends on both the angle of the spin-dependent force and on the direction of squeezing (see Fig. 3.7). The rate at which $P_\downarrow$ tends to 1/2 is maximized when the SDF is applied along the squeezed axis ($\theta = 0$, $\phi = 0$) and minimized if the SDF is applied along the anti squeezed axis ($\theta = \pi$, $\phi = 0$). If the ion is initially in a thermal distribution with $\langle n \rangle = \bar{n}$,

$$P_{\downarrow,th} = \frac{1}{2}\left(1 + e^{-|\alpha|^2(2\bar{n}+1)[e^{2r}\cos^2(\phi-\theta/2)+e^{-2r}\sin^2(\phi-\theta/2)]}\right). \tag{3.37}$$

The initial thermal occupation results in faster decay of $P_{\downarrow,th}$ to 1/2 than for a system prepared in the motional ground state (see Fig. 3.7).

3.4 Geometric phase gates

This section describes the implementation of geometric phase gates using spin-dependent forces. There are two classes of geometric phase gates that operate on different spin bases: the Mølmer-Sørensen, or $\hat{\sigma}_\phi\hat{\sigma}_\phi$, gate [48, 49, 50] and the $\hat{\sigma}_z\hat{\sigma}_z$ gate [51, 52].

3.4.1 The Mølmer-Sørensen gate

The Mølmer-Sørensen gate [48] is implemented by applying a spin dependent force to two (or more) trapped ions with a shared mode of motion. Without any spin-motion coupling, the Hamiltonian describing the harmonically confined qubits is

$$\hat{H}_0 = \frac{\hbar\omega_0}{2}\hat{\sigma}_{z1} + \frac{\hbar\omega_0}{2}\hat{\sigma}_{z2} + \hbar\omega\hat{a}^\dagger\hat{a}, \tag{3.38}$$

where $\hat{\sigma}_{z1}$ and $\hat{\sigma}_{z2}$ are Pauli operators describing the qubit state of each ion and $\hat{a}(\hat{a}^\dagger)$ is now the annihilation (creation) operator of the shared motional mode. Following the methods of the previous section, the interaction picture Hamiltonian for the spin-dependent force is given by

$$\hat{H}_{MS} = \frac{\hbar\Omega}{2}\hat{S}_x(\hat{a}e^{i\delta t} + \hat{a}^\dagger e^{-i\delta t}) \tag{3.39}$$

where $\hat{a}$ is the harmonic oscillator annihilation operator for the shared motional mode. The coupling strength Ω is assumed to be the same for both ions, $\hat{S}_x = \sum_{i=1}^{2} \beta_i \hat{\sigma}_{xi}$, where β_i is proportional to the i^{th} component of the mode eigenvector, and $\hat{\sigma}_{xi}$ is the Pauli operator for the i^{th} ion. For a center-of-mass (COM) mode, the mode eigenvector is $\frac{1}{\sqrt{2}}(1,1)$. For convenience, we set $\hat{S}_x = \hat{\sigma}_{x1} + \hat{\sigma}_{x2}$ and let the factor of $\frac{1}{\sqrt{2}}$ be absorbed into Ω. For an out-of-phase motional mode the eigenvector is $\frac{1}{\sqrt{2}}(1,-1)$ and $\hat{S}_x = \hat{\sigma}_{x1} - \hat{\sigma}_{x2}$. The time evolution operator for Eq. 3.39 can be calculated exactly using the Magnus expansion method (see Appendix A). The relevant commutators are

$$\begin{aligned}
[\hat{H}(t), \hat{H}(t')] &= \left(\frac{\hbar\Omega}{2}\right)^2 \hat{S}_x^2 [\hat{a}e^{i\delta t} + \hat{a}^\dagger e^{-i\delta t}, \hat{a}e^{i\delta t'} + \hat{a}^\dagger e^{-i\delta t'}] \\
&= 2i \left(\frac{\hbar\Omega}{2}\right)^2 \hat{S}_x^2 \sin(\delta(t-t'))
\end{aligned} \tag{3.40}$$

and

$$[[\hat{H}(t), \hat{H}(t')], \hat{H}(t'')] = 0. \tag{3.41}$$

The time evolution operator is then

$$\hat{U}(t, t_0) = e^{-C_1(t,t_0)} e^{-C_2(t,t_0)} \tag{3.42}$$

where

$$\begin{aligned}
C_1(t, t_0) &= \frac{1}{i\hbar} \int_{t_0}^{t} \hat{H}(t') dt' \\
&= \frac{1}{i\hbar} \frac{\hbar\Omega}{2} \hat{S}_x \int_{t_0}^{t} (\hat{a}e^{i\delta t'} + \hat{a}^\dagger e^{-i\delta t'}) dt' \\
&= i\frac{\Omega}{\delta} \hat{S}_x \sin\left(\frac{\delta(t-t_0)}{2}\right) (\hat{a}e^{i\delta(t+t_0)/2} - \hat{a}^\dagger e^{-i\delta(t+t_0)/2}),
\end{aligned} \tag{3.43}$$

and

$$\begin{aligned} C_2(t,t_0) &= \frac{1}{2}\left(\frac{1}{i\hbar}\right)^2 \int_{t_0}^{t}\int_{t_0}^{t'} [\hat{H}(t'),\hat{H}(t'')]dt' \\ &= -i\frac{\Omega^2}{4}\hat{S}_x^2 \int_{t_0}^{t}\int_{t_0}^{t'} \sin(\delta(t'-t''))dt''dt' \\ &= i\frac{\Omega^2}{4\delta^2}\hat{S}_x^2[\delta(t-t_0)-\sin(\delta(t-t_0))], \end{aligned} \tag{3.44}$$

giving

$$\hat{U}(t,t_0) = \hat{D}(\beta(t,t_0)\hat{S}_x)e^{-i\Phi(t,t_0)\hat{S}_x^2} \tag{3.45}$$

where the spin-dependent displacement amplitude is

$$\beta(t,t_0)\hat{S}_x = -i\frac{\Omega}{\delta}\sin\left(\frac{\delta(t-t_0)}{2}\right)e^{-i\delta(t+t_0)/2}\hat{S}_x, \tag{3.46}$$

and the spin-dependent geometric phase is given by

$$\Phi(t,t_0)\hat{S}_x^2 = \frac{\Omega^2}{4\delta^2}[\delta(t-t_0)-\sin(\delta(t-t_0))]\hat{S}_x^2. \tag{3.47}$$

If $\hat{S}_x = \hat{\sigma}_{x1}+\hat{\sigma}_{x2}$, the matrix representations of $\hat{S}_x$ and $\hat{S}_x^2$ in terms of the two-ion spin states $|{+}{+}\rangle$, $|{+}{-}\rangle$, $|{-}{+}\rangle$ and $|{-}{-}\rangle$ (where $|\pm\rangle = \frac{1}{\sqrt{2}}(|\uparrow\rangle \pm |\downarrow\rangle)$ are the eigenstates of $\hat{\sigma}_x$) are given by

$$\hat{S}_x = \begin{bmatrix} 2 & 0 & 0 & 0 \\ 0 & 0 & 0 & 0 \\ 0 & 0 & 0 & 0 \\ 0 & 0 & 0 & -2 \end{bmatrix} \tag{3.48}$$

and

$$\hat{S}_x^2 = \begin{bmatrix} 4 & 0 & 0 & 0 \\ 0 & 0 & 0 & 0 \\ 0 & 0 & 0 & 0 \\ 0 & 0 & 0 & 4 \end{bmatrix}. \tag{3.49}$$

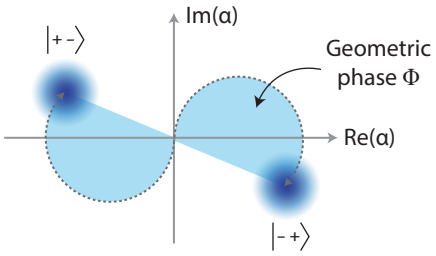

Figure 3.8: Phase-space illustration of the oscillator wavepacket trajectories during a geometric phase gate.

If $\hat{S}_x = \hat{\sigma}_{x1} - \hat{\sigma}_{x2}$, the matrix representations are

$$\hat{S}_x = \begin{bmatrix} 0 & 0 & 0 & 0 \\ 0 & 2 & 0 & 0 \\ 0 & 0 & -2 & 0 \\ 0 & 0 & 0 & 0 \end{bmatrix} \tag{3.50}$$

and

$$\hat{S}_x^2 = \begin{bmatrix} 0 & 0 & 0 & 0 \\ 0 & 4 & 0 & 0 \\ 0 & 0 & 4 & 0 \\ 0 & 0 & 0 & 0 \end{bmatrix}. \tag{3.51}$$

The detuned spin-dependent force results in spin-dependent displacements with circular trajectories in phase space. For the out-of-phase mode, the $|{+}{+}\rangle$ and $|{-}{-}\rangle$ states are not displaced. The $|{+}{-}\rangle$ and $|{-}{+}\rangle$ states follow circular trajectories and return to the origin when $t_K = t_0 + K\frac{2\pi}{\delta}$, where $K = 1, 2, 3...$. The area enclosed by each phase space loop is equal to the geometric phase accrued at t_n, $4\Phi(t_n) = \frac{2\pi\Omega^2}{\delta^2}$.

To implement an entangling gate with one phase space loop ($K = 1$), the $|{+}{-}\rangle$ and $|{-}{+}\rangle$ states must acquire a phase of $\pi/2$ relative to the $|{+}{+}\rangle$, and $|{-}{-}\rangle$ states. The truth table for the

gate is given by

$$\begin{aligned}
|{+}{+}\rangle &\rightarrow |{+}{+}\rangle \\
|{+}{-}\rangle &\rightarrow e^{i\pi/2}\,|{+}{-}\rangle \\
|{-}{+}\rangle &\rightarrow e^{i\pi/2}\,|{-}{+}\rangle \\
|{-}{-}\rangle &\rightarrow |{-}{-}\rangle\,. \qquad (3.52)
\end{aligned}$$

If the initial state is $|\Psi\rangle_0 = |{\downarrow}{\downarrow}\rangle\,|0\rangle$, applying the Mølmer-Sørensen time evolution operator (Eq. 3.45) to $|\Psi\rangle_0$, with $t_0 = 0$ and $t_n = t_g = \dfrac{\pi}{\Omega}$ gives

$$\begin{aligned}
|\Psi(t_g)\rangle &= \hat{U}(t_g)\,|\Psi\rangle_0 \\
&= \frac{1}{2}\exp\left(-i\frac{\pi\hat{S}_x^2}{8}\right)(|{+}{+}\rangle - |{+}{-}\rangle - |{-}{+}\rangle + |{-}{-}\rangle) \\
&= -\frac{e^{-i\pi/4}}{\sqrt{2}}(|{\downarrow}{\downarrow}\rangle + i\,|{\uparrow}{\uparrow}\rangle), \qquad (3.53)
\end{aligned}$$

a maximally entangled Bell state. It is also useful to have an analytical expression for the state and populations at any time given an arbitrary initial Fock state $|n\rangle$ and spin state $|{\downarrow}{\downarrow}\rangle$.

$$\begin{aligned}
|\Psi_n(t)\rangle &= \hat{U}(t, t_0 = 0)\,|{\downarrow}{\downarrow}\rangle\,|n\rangle \\
&= \frac{1}{2}\Big[\hat{D}(2\beta(t))e^{-4i\Phi(t)}\,|{+}{+}\rangle + \hat{D}(-2\beta(t))e^{-4i\Phi(t)}\,|{-}{-}\rangle \\
&\quad - |{+}{-}\rangle - |{-}{+}\rangle\Big]\,|n\rangle \qquad (3.54)
\end{aligned}$$

The projection onto the $|{\downarrow}{\downarrow}\rangle$ state is then

$$\langle{\downarrow}{\downarrow}\,|\Psi_n(t)\rangle = \frac{1}{4}\left[\hat{D}(2\beta(t))e^{-4i\Phi(t)} + \hat{D}(-2\beta(t))e^{-4i\Phi(t)} + 2\right]|n\rangle\,, \qquad (3.55)$$

and probability of measuring $|{\downarrow}{\downarrow}\rangle$ is

$$P_{\downarrow\downarrow}(t) = \frac{1}{8}\left(3 + 4\cos(4\Phi(t))\mathcal{L}_n(|2\beta(t)|^2)e^{-\frac{|2\beta(t)|^2}{2}} + \mathcal{L}_n(|4\beta(t)|^2)e^{-\frac{|4\beta(t)|^2}{2}}\right). \qquad (3.56)$$

The projection onto the $|\downarrow\uparrow\rangle$ state is

$$\langle\downarrow\uparrow|\Psi_n(t)\rangle = \frac{1}{4}\left[\hat{D}(2\beta(t))e^{-4i\Phi(t)} - \hat{D}(-2\beta(t))e^{-4i\Phi(t)}\right]|n\rangle\,, \tag{3.57}$$

and the probability of measuring $|\uparrow\downarrow\rangle$ is

$$P_{\uparrow\downarrow}(t) = \frac{1}{8}\left(1 - \mathcal{L}_n(|4\beta(t)|^2)e^{-\frac{|4\beta(t)|^2}{2}}\right). \tag{3.58}$$

The remaining populations can be calculated from $P_{\downarrow\downarrow}(t)$ and $P_{\uparrow\downarrow}(t)$. The probability of measuring $|\downarrow\uparrow\rangle$, $P_{\downarrow\uparrow}(t) = P_{\uparrow\downarrow}(t)$, and $P_{\uparrow\uparrow}(t) = 1 - P_{\downarrow\downarrow}(t) - P_{\uparrow\downarrow}(t) - P_{\downarrow\uparrow}(t)$. If the initial state is in a thermal distribution

$$P_{\downarrow\downarrow}(t) = \frac{1}{8}\left(3 + 4\cos(4\Phi(t))e^{-(\bar{n}+1/2)|2\beta(t)|^2} + e^{-(\bar{n}+1/2)|4\beta(t)|^2}\right) \tag{3.59}$$

and

$$P_{\uparrow\downarrow}(t) = \frac{1}{8}\left(1 - e^{-(\bar{n}+1/2)|4\beta(t)|^2}\right). \tag{3.60}$$

Another quantity of interest is the Bell-state fidelity defined as

$$\mathcal{F} \equiv \langle\Psi_{Bell}|\,\hat{\rho}_{sys}\,|\Psi_{Bell}\rangle\,, \tag{3.61}$$

where $|\Psi_{Bell}\rangle = \frac{1}{\sqrt{2}}(\uparrow\uparrow + i\,|\downarrow\downarrow\rangle)$, and $\hat{\rho}_{sys}$ is the system density matrix. If the system is in a pure state $|\Psi_n(t)\rangle$, the density matrix is $\hat{\rho}_{sys} = |\Psi_n(t)\rangle\langle\Psi_n(t)|$ and the fidelity is given by

$$\mathcal{F} = \frac{1}{8}\left[3 + e^{-|4\beta(t)|^2/2}\mathcal{L}_n(|4\beta(t)|^2) + 4\sin(4\Phi(t))e^{-|2\beta(t)|^2/2}\mathcal{L}_n(|2\beta(t)|^2)\right]. \tag{3.62}$$

Figure 3.9 shows the populations and fidelity as a function of detuning for the optimal single-loop gate time. For an initial thermal distribution with mean motional occupation $\bar{n}$, the fidelity becomes

$$\mathcal{F} = \frac{1}{8}\left[3 + e^{-(\bar{n}+1/2)|4\beta(t)|^2} + 4\sin(4\Phi(t))e^{-(\bar{n}+1/2)|2\beta(t)|^2}\right]. \tag{3.63}$$

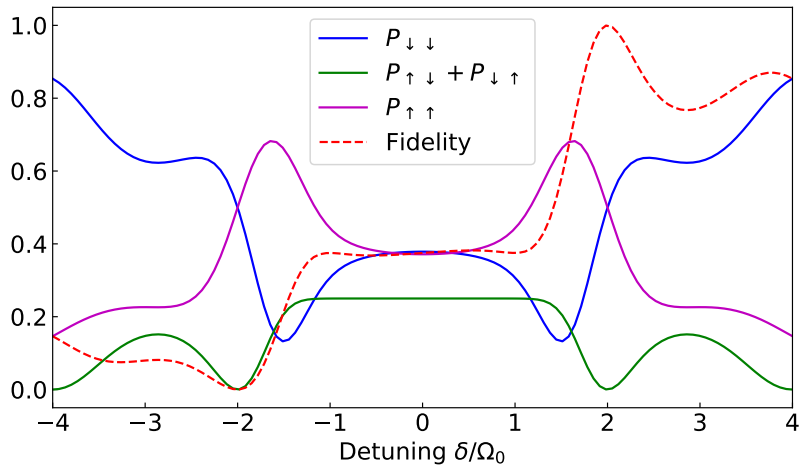

Figure 3.9: Populations and fidelity for generating the Bell-state $\frac{1}{\sqrt{2}}(|\downarrow\downarrow\rangle + i\,|\uparrow\uparrow\rangle)$ as a function of the gate detuning for the Mølmer-Sørensen entangling gate, where the gate mode was initialized in the motional ground state. The gate time is $t_g = \pi/\Omega$. Note that the fidelity reaches 1 at a detuning of $\delta/\Omega = 2$. At $\delta/\Omega = -2$, the orthogonal bell-state $\frac{1}{\sqrt{2}}(|\downarrow\downarrow\rangle - i\,|\uparrow\uparrow\rangle)$ is generated giving a fidelity of 0.

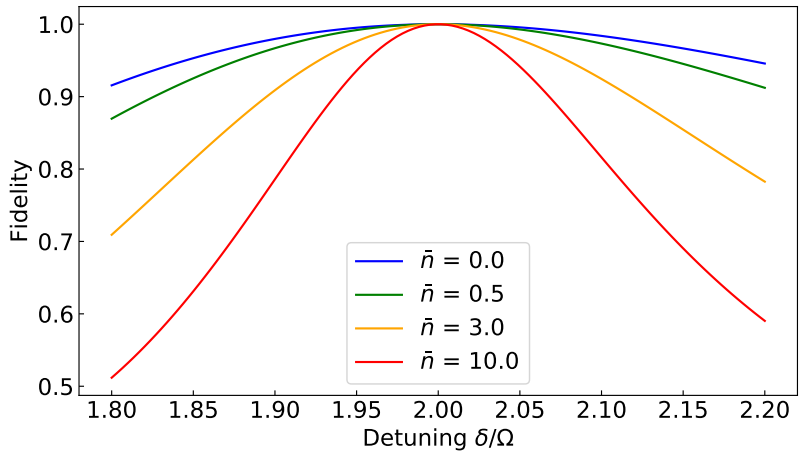

Figure 3.10: Bell-state fidelity as a function of the gate detuning for various values of the initial thermal occupation $\bar{n}$. The gate time is $t_g = 2\pi/\Omega_0$. Increasing $\bar{n}$ increases the sensitivity of the fidelity to detuning errors.

The initial thermal distribution does not prevent the generation of maximally entangled Bell-states, however the gate becomes more sensitive to miscalibrations of parameters such as the gate time and detuning (see Fig.3.10). There are many other mechanisms that can reduce the fidelity of geometric phase gates. These will be discussed later in this chapter.

3.4.2 $\hat{\sigma}_z\hat{\sigma}_z$ gate

Geometric phase gates can also be implemented using spin-dependent forces that act in the z basis. The so called $\hat{\sigma}_z\hat{\sigma}_z$ gate was originally proposed by Milburn et al. [51] and was first demonstrated using lasers at NIST by Leibfried et al. [52]. The interaction picture Hamiltonian for the $\hat{\sigma}_z\hat{\sigma}_z$ interaction is given by

$$\hat{H}_{ZZ} = \frac{\hbar\Omega}{2}\hat{S}_z(\hat{a}e^{i\delta t} + \hat{a}^\dagger e^{-i\delta t}), \tag{3.64}$$

where $\hat{S}_z = \sum_{i=1}^{2}\beta_i\hat{\sigma}_{zi}$. For a two-ion radial center-of-mass mode (COM), $\hat{S}_z = \hat{\sigma}_{z1} + \hat{\sigma}_{z2}$ and for an out-of-phase mode $\hat{S}_z = \frac{1}{\sqrt{2}}(\hat{\sigma}_{z1} - \hat{\sigma}_{z2})$. Because the $\hat{\sigma}_z\hat{\sigma}_z$ gate acts on the eigensates of $\hat{S}_z$, generation of entangled states is usually requires $\hat{H}_{ZZ}$ to be applied within a Ramsey sequence. The derivation of the time evolution operator is very similar to the derivation for the MS gate described above.

3.5 Motional decoherence

In this section I discuss the dominant noise processes affecting our experiments, motional heating and motional dephasing. Experimentally both dephasing and heating can arise from anomalous electric field noise on ion trap surfaces [41, 53, 54] and can also result from technical noise. We account for motional decoherence processes by numerically integrating the master equation[32]

$$\frac{\partial\hat{\rho}}{\partial t} = -\frac{i}{\hbar}[\hat{H},\hat{\rho}] + \frac{1}{2}\sum_{n=0}\left[2\hat{C}_n\hat{\rho}C_n^\dagger - \{\hat{C}_n^\dagger C_n,\hat{\rho}\}\right], \tag{3.65}$$

where $\hat{\rho}$ is the system density matrix, $\hat{H}$ is the Hamiltonian in the absence of noise, and the $\hat{C}_n$ are Lindblad operators that describe the decoherence processes (the sum runs over all processes that are considered). This approach requires that the noise can be modeled as a stochastic Markov process with no memory [55]. A more comprehensive analysis of coherent and incoherent error sources for MS gates can be found in [56]. For all numerical simulations in the thesis, I used the QuTip [57] python package.

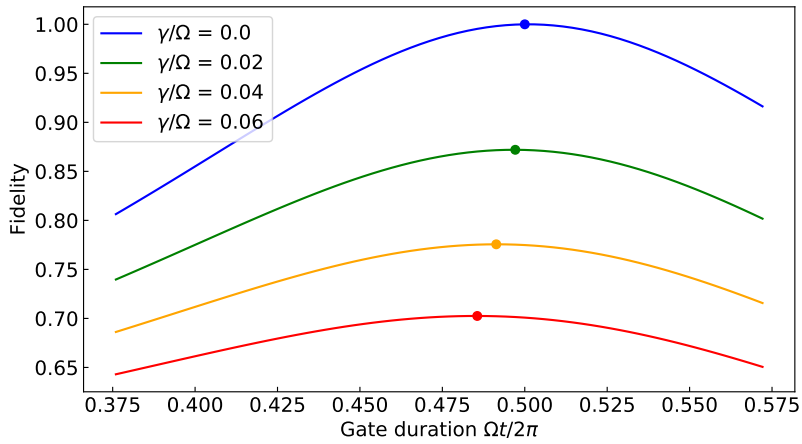

Figure 3.11: Simulated fidelity of a Bell state produced by the Mølmer-Sørensen gate as a function of gate duration $\Omega t/2\pi$ for various values of the motional dephasing rate γ, with all other gate parameters held at their ideal values. Here t is the gate duration and Ω is the Rabi frequency (Eq. 3.39). It is assumed that no other sources of decoherence are present. For all simulations, the gate detuning is set to $\delta = 2\Omega$. Circles indicate the duration at which maximum fidelity occurs for each value of γ. Increasing γ reduces the gate fidelity and also the gate duration at which maximum fidelity occurs.

3.5.1 Motional dephasing

The first process that we consider results from motional mode frequency fluctuations that are fast compared to the duration of a coherent operation such as a geometric phase gate. During a gate these fluctuations dephase the motional state while it is entangled with the qubit states resulting in reduced fidelity. We model motional dephasing using the Lindblad operator $\hat{C}_0 = \sqrt{\gamma}\hat{a}^\dagger\hat{a}$, where γ is the motional dephasing rate. For a purely motional density matrix expressed in the number state basis as $\hat{\rho} = \sum_{n,m} \rho_{nm} |m\rangle \langle n|$, dephasing results in the decay of the off diagonal elements (coherences) given by [58]

$$\rho_{nm}(t) = e^{-\frac{\gamma}{2}(n-m)^2 t}\rho(0)_{nm}, \tag{3.66}$$

showing that the off-diagonal elements decay exponentially at a rate proportional to the square of the number state difference $n - m$. After integrating Eq. 3.65, we plot the fidelity of a single-loop two-qubit MS gate as a function of the gate time for various values of γ (Fig. 3.11), with the

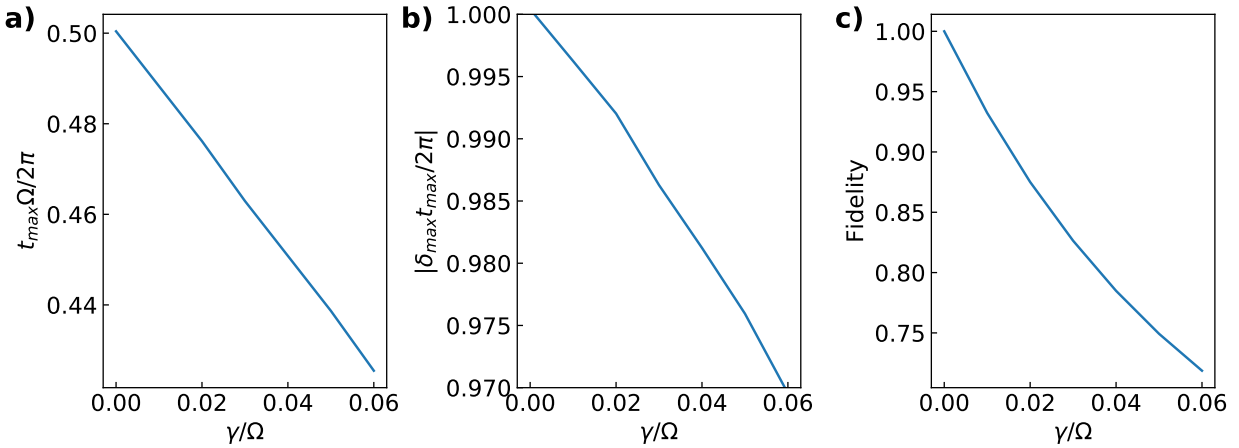

Figure 3.12: Simulated gate duration t_{max} (a) and product $t_{max}\delta_{max}$ (b) required for maximum fidelity of a Bell state produced by the Mølmer-Sørensen gate (c) as a function of the motional dephasing rate γ, with no additional sources of decoherence. Ω is the gate Rabi frequency. Increasing γ reduces both the fidelity and the gate duration that gives maximum fidelity.

gate detuning δ fixed at -2Ω. As expected, increasing γ reduces the gate fidelity. It is also clear that shorter gate durations maximize the fidelity as the dephasing rate increases. To investigate this effect further, we calculate the gate duration t_{max} and detuning δ_{max} that maximize the Bell-state fidelity for various values of γ (Fig.3.12). The optimized gate duration falls off linearly with γ, whereas the fidelity decrease is less than linear. Physically the tradeoff between fidelity reduction from motional decoherence (which penalizes longer gate durations) and from incorrect geometric phase acquisition or failure to close the phase space loop (which penalize either shorter or longer durations than the theoretically optimal duration) results in a shorter gate duration giving the highest fidelity. This effect also occurs with motional heating, which I discuss next and is an important factor in our investigation of parametrically accelerated geometric phase gates (Chapter 8).

3.5.2 Motional heating

Another type of motional decoherence results from uncontrolled heating of the ion crystal. We model stochastic motional heating using the Lindblad operators $\hat{C}_1 = \sqrt{\dot{n}}\hat{a}$ and $\hat{C}_2 = \sqrt{\dot{n}}\hat{a}^\dagger$,

where $\dot{n}$ is the heating rate. Theoretically, this kind of decoherence arises when an oscillator is coupled via its position to a bath consisting of an infinite bath of oscillators at thermal equilibrium [58]. Results from numerical integration of Eq. 3.65 including only $\hat{C}_1$ and $\hat{C}_2$ Lindblad operators are shown in Fig. 3.13. Increasing the heating rate $\dot{n}$ reduces the fidelity as expected. As for motional dephasing, heating shifts the gate time and detuning required to maximize the fidelity (Fig. 3.14).

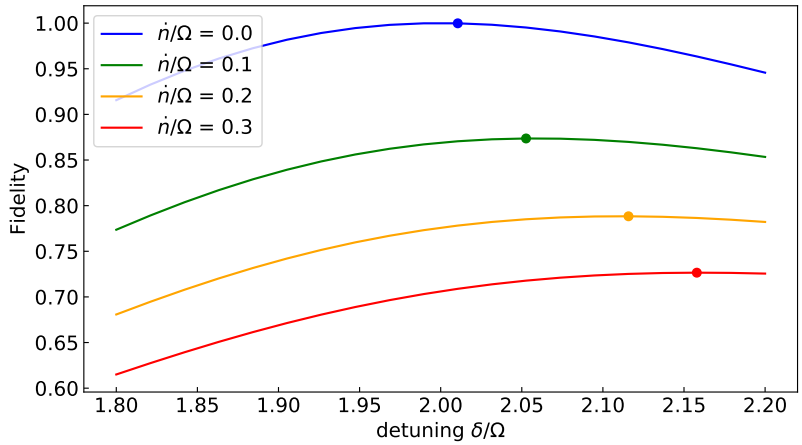

Figure 3.13: Simulated fidelity of a Bell state produced by the Mølmer-Sørensen gate as a function of gate detuning δ/Ω, where δ is the detuning and Ω is the Rabi frequency (Eq. 3.39), for various values of the heating rate $\dot{n}$, assuming no other sources of error. For all simulations, the gate duration is set to $t = \pi/\Omega$. Circles indicate the duration at which maximum fidelity occurs for each value of $\dot{n}$. Increasing $\dot{n}$ reduces the gate fidelity and lowers the detuning needed to maximize the fidelity for a given value of $\dot{n}$.

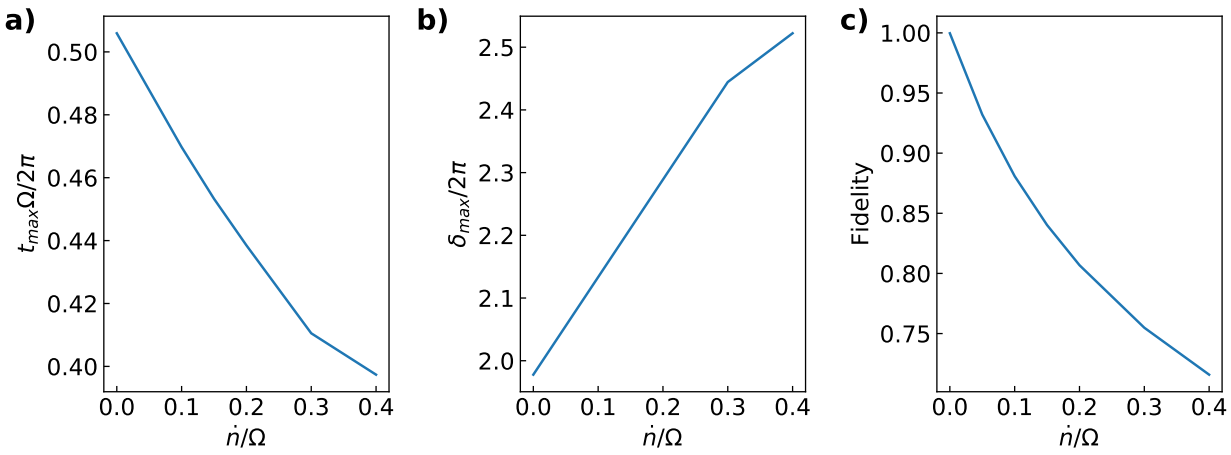

Figure 3.14: Simulated Mølmer-Sørensen gate duration t_{max} (a) and detuning δ_{max} (b) for maximized Bell-state fidelity (c) as a function of the motional dephasing rate $\dot{n}$, assuming no other error sources are present. Ω is the gate Rabi frequency. Increasing $\dot{n}$ reduces both the fidelity and the gate duration that gives maximum fidelity.

Chapter 4

Experimental setup

Our experimental apparatus was designed for trapping ions in close proximity to current carrying electrodes for implementing high-fidelity "laser-free" entangling gates using oscillating near-field magnetic field gradients. Furthermore, the geometry of our trap enables relatively strong oscillating electric-field gradients to be generated at the ions' position allowing parametric modulation and squeezing of the ions' motion. This chapter gives an overview of the experimental hardware we use for trapping ions and for controlling them using these gradients.

4.1 Surface-electrode ion trap

Charged particles cannot be confined in three dimensions using only static electric fields. However, stable confinement can be achieved using a combination of static and time varying fields. Figure 4.1 a shows a diagram of a typical 3D linear radio frequency (RF) or Paul trap [59]. Confinement along the trap axis (dotted line) is provided by static potentials applied to the outer DC electrodes, whereas confinement in the plane normal to the axis (the radial plane) is achieved by applying an oscillating potential $V_{RF}\cos(\omega_{RF}t) + V_b$ to two diagonally opposite electrodes. To leading order, the potential near the trap axis in the radial plane is a quadrupole (Fig. 4.1 a). Provided the amplitude V_{RF} and RF frequency ω_{RF} are chosen correctly [41, 60], a charged particle will feel a ponderomotive restoring force and a corresponding effective harmonic potential, which enables stable confinement in the radial plane. Away from locations with zero RF field, motion in the effective potential (known as "secular motion") is superimposed with small-amplitude motion

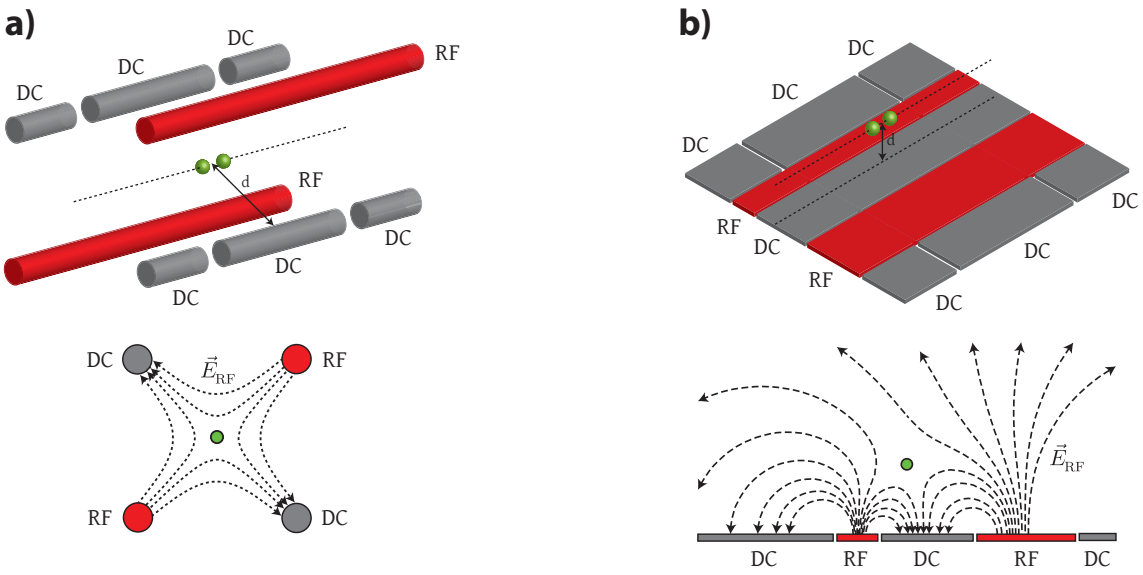

Figure 4.1: Linear radio-frequency (RF) Paul traps. The upper figures show schematic diagrams of a conventional linear RF Paul trap (a) and a surface-electrode Paul trap (b) with two trapped ions indicated by green spheres. Dashed lines indicate the trap axis. Lower panels show radial cross sections perpendicular to the trap axis. Dashed arrows illustrate electric field lines and green disks the radial equilibrium position of the ions.

at ω_{RF} which is known as micromotion.

One can also imagine unfolding and flattening the 3D Paul trap structure onto a plane (Fig. 4.1 B). In this case a quadrupole forms above the trap surface and the device is known as a surface-electrode ion trap [61, 62]. Our current trap is a surface-electrode trap that was designed and fabricated by Daniel Slichter and David Allcock building on previous NIST designs [63]. A photograph and electron microscope image of the trap are shown in Figure 4.2. Ions are trapped at a height of $d \simeq 30\,\mu$m above the trap surface. RF potentials with a frequency of $\omega_{RF}/2\pi = 68.608\,$MHz and amplitude of $V_{RF} \simeq 30\,$V are applied to the RF electrodes to provide confinement in the radial $(y-z)$ plane. The amplitude of the RF drive is stabilized using a limiting amplifier circuit based on a design in [64]. A half-wave coaxial resonator serves to step up the RF amplitude to the level required at the trap electrodes. Eighteen DC electrodes are used to apply potentials for axial confinement, for micromotion compensation, for setting the frequencies of the

two secular modes of motion in the y-z plane, and for implementing resonant displacements. The potentials on these electrodes are controlled using a multi-channel digital-to-analog converter [65]. The axial secular frequency is $\omega_x/2\pi \simeq 3\,\mathrm{MHz}$. Typical secular frequencies in the radial plane are $(\omega_{r1}, \omega_{r2})/2\pi \simeq (6, 7.5)\,\mathrm{MHz}$, where $r1$ and $r2$ denote orthogonal unit vectors in the $y - z$ plane. The orientations of the radial modes depend on the values of the DC potentials. The trap also has three "microwave" electrodes for carrying the oscillating currents required to generate near-field magnetic field gradients. These electrodes are grounded at one end of the trap to give a current anti-node near the position of the ions. These microwave electrodes are discussed in more detail in section 4.6.1

All trap electrodes are $8\,\mu$m-thick gold electroplated onto a sapphire substrate. The trap electrodes are ribbon-bonded onto screen-printed gold electrodes on an alumina circuit board, which also hosts RC low-pass filters (100 kHz cut-off frequency) to reduce high-frequency voltage noise on the dc electrodes.

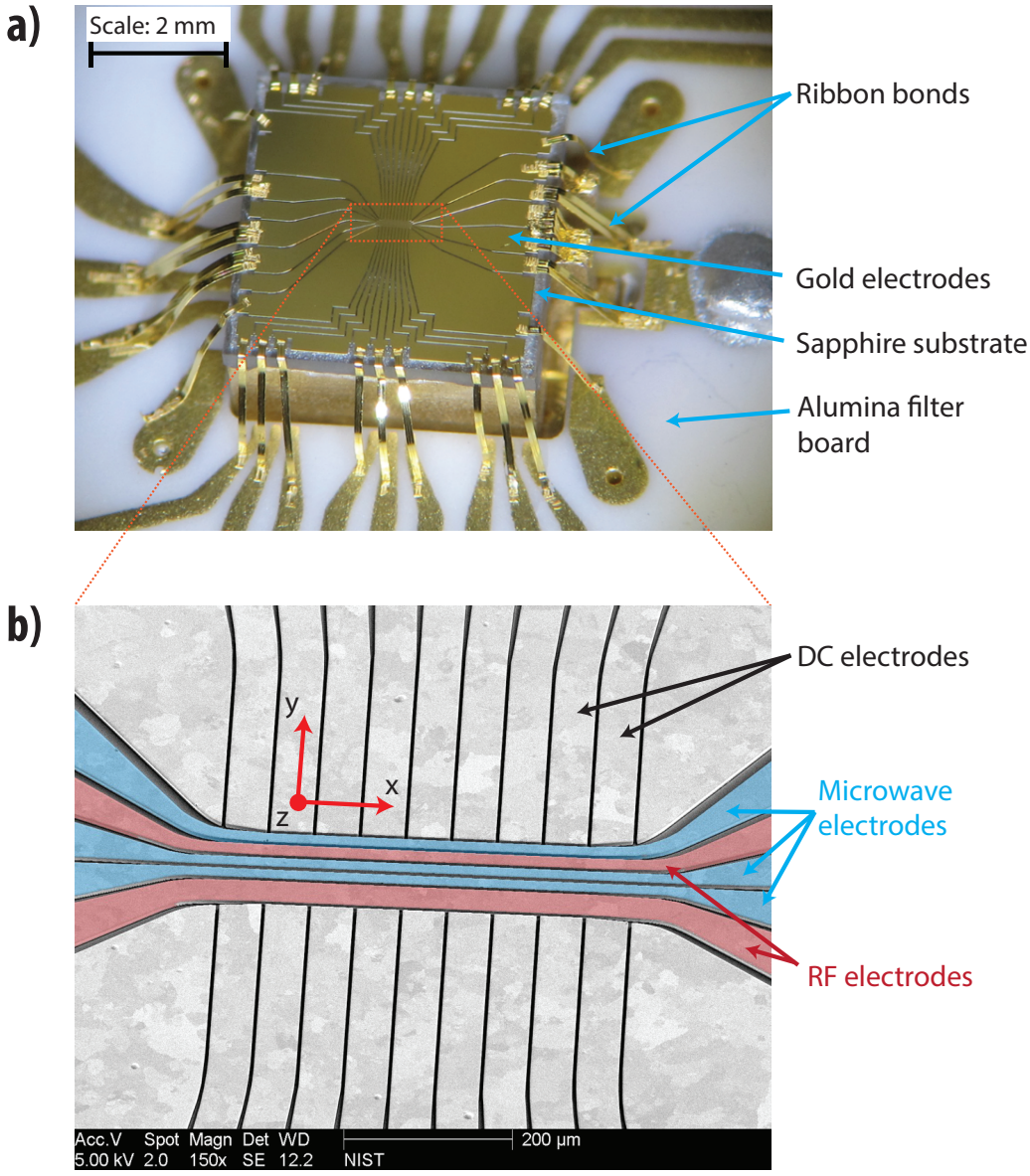

Figure 4.2: Surface-electrode ion trap designed for implementing near-field magnetic field gradient entangling gates. a) Photograph of the trap chip. b) Electron microscope image of the trapping zone with false colors indicating the DC, RF, and microwave electrodes.

4.2 Vacuum chamber and cryostat

The filter board and ion trap are contained in a gold-coated oxygen-free high thermal conductivity (OFHC) copper pillbox (Fig. 4.3). The relatively large thermal diffusivity of the pillbox

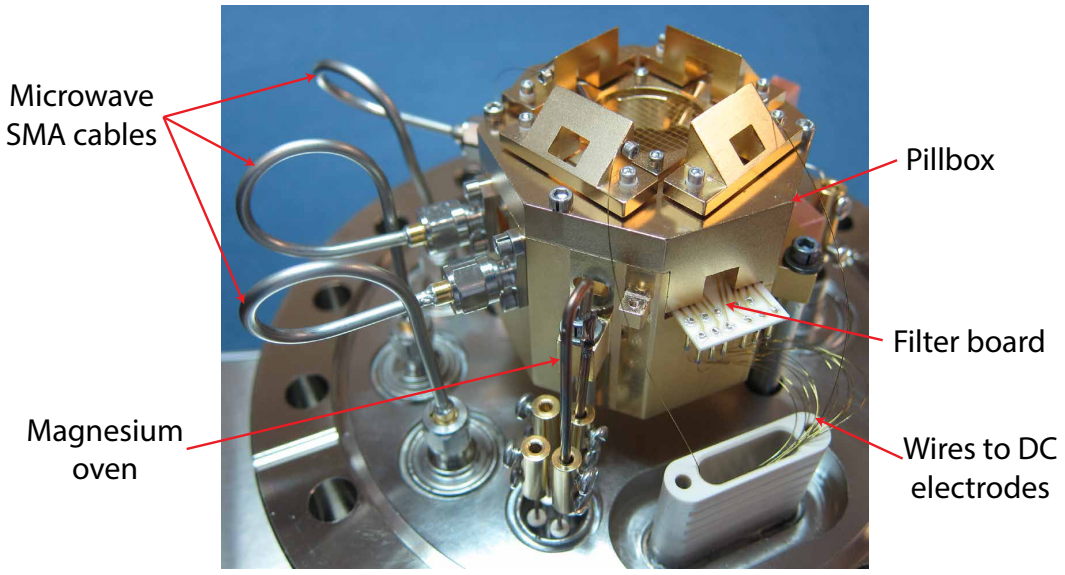

Figure 4.3: Annotated photograph of the pillbox.

helps to rapidly transfer heat generated by microwave and RF currents away from the trap. The pillbox is cryogenically cooled below 20 K through a copper braid connected to a liquid helium flow cryostat. There are several advantages of operating at low temperatures. First, cryogenic operation reduces background gas pressure, which improves ion lifetime in the trap. Second, heating due to anomalous electric field noise is typically suppressed at cryogenic temperatures [66, 67, 68]. Third, the thermal and electrical conductivity of the gold trap electrodes are larger at cryogenic temperatures than at room temperature enabling larger current densities in the microwave electrodes than would be possible at room temperature. Larger currents in these electrodes permit stronger spin-motion coupling (see section 4.6.1).

The pillbox is housed in a 6" octagonal vacuum chamber[1] see Figs. 4.4 and 4.5). The chamber has angled viewports which serve to keep view-port reflections of laser beams away from the trap. Ultra-high vacuum pressure is maintained using a non-evaporable getter pump[2] .

[1] Kimball Physics custom part
[2] Agilent Vaclon Plus 20 Star Cell

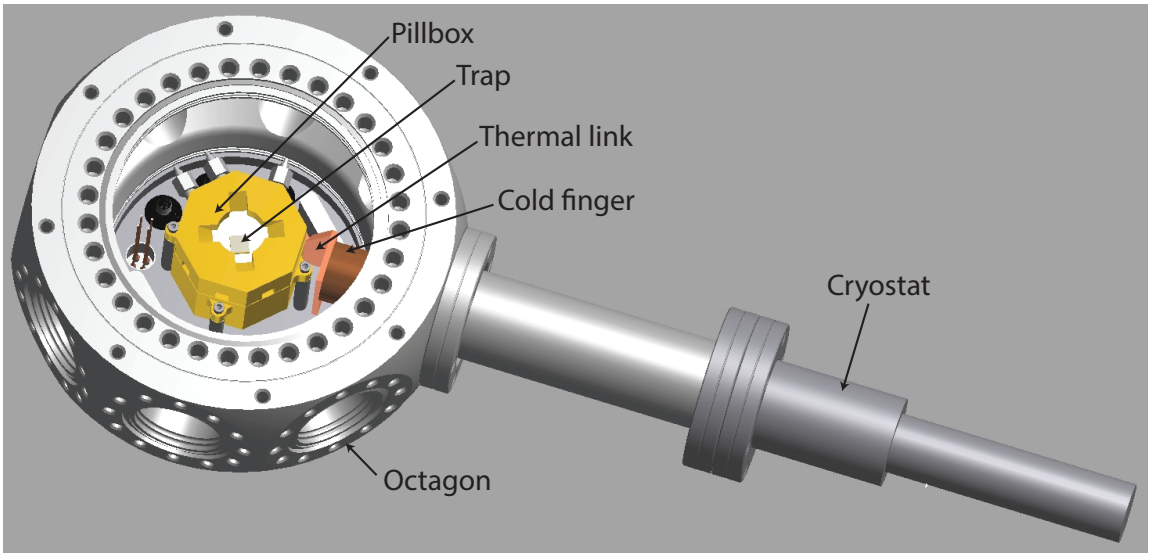

Figure 4.4: Partial CAD rendering of the vacuum chamber and cryostat

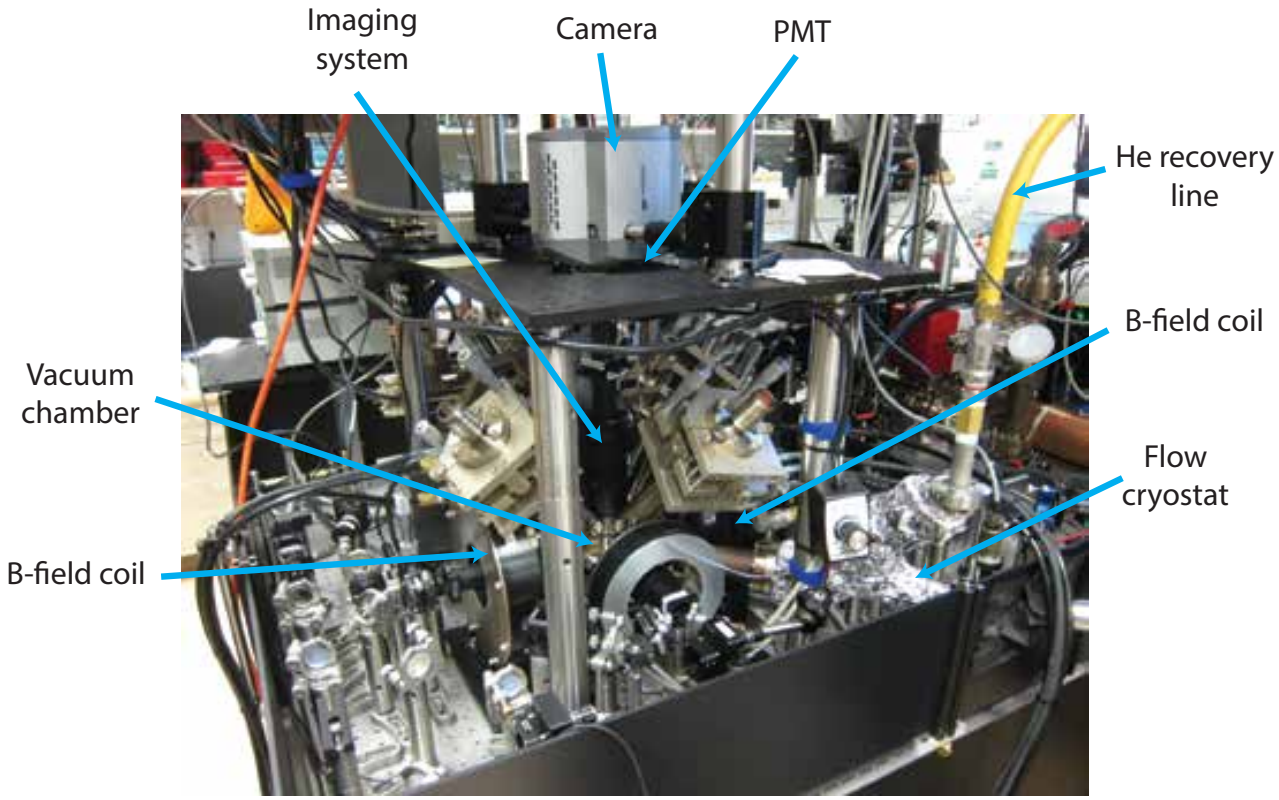

Figure 4.5: Annotated photograph of the vacuum chamber, cryostat, and imaging system. PMT: Photo-multiplier tube

4.3 $^{25}Mg^{+}$ ion qubit

In our system we use $^{25}Mg^{+}$ ions. With a single valence electron, $^{25}Mg^{+}$ has an electronic structure similar to that of neutral alkali atoms. A diagram with the relevant energy levels is shown in Figure 4.6. The electronic ground state configuration is $1s^2 2s^2 2p^6 3s^2\, ^2S_{J=1/2}$, where $J = L + S$ is the sum of the orbital angular momentum ($L = 0$) and the electron spin angular momentum ($S = 1/2$). The interaction between the nuclear spin ($I = 5/2$) and the outer electron spin give rise to hyperfine splitting of the atomic energy levels. In the ground state, there are two hyperfine levels that are split by $\sim 1.7\,\text{GHz}$ and are labeled $F = 2$ and $F = 3$, where $F = I + J$ is the total angular momentum quantum number. The hyperfine levels are further split into Zeeman sublevels labeled by the magnetic quantum number m_F, which is the projection of the total angular momentum along the direction of an external magnetic field of $B \simeq 212\,\text{G}$. At this field the frequency of the $|F = 3, m_F = 1\rangle \leftrightarrow |F = 2, m_F = 1\rangle$ "clock" transition ($\omega_0/2\pi = 1.686\,\text{GHz}$) is first-order insensitive to magnetic field fluctuations [69, 70]. These levels, labeled as $|\downarrow\rangle \equiv |3, 1\rangle$, and $|\uparrow\rangle \equiv |2, 1\rangle$, comprise the qubits for most of the experiments in this thesis. The coherence time of these qubits (measured using a Ramsey experiment) is longer than 200 ms. For several applications it is convenient to use a two-level system formed by the $|\downarrow_s\rangle \equiv {}^2S_{1/2}\,|3, 3\rangle$ and $|\uparrow_s\rangle \equiv {}^2S_{1/2}\,|2, 2\rangle$ levels, which have a frequency splitting of $\omega_s/2\pi = 1.326\,\text{GHz}$.

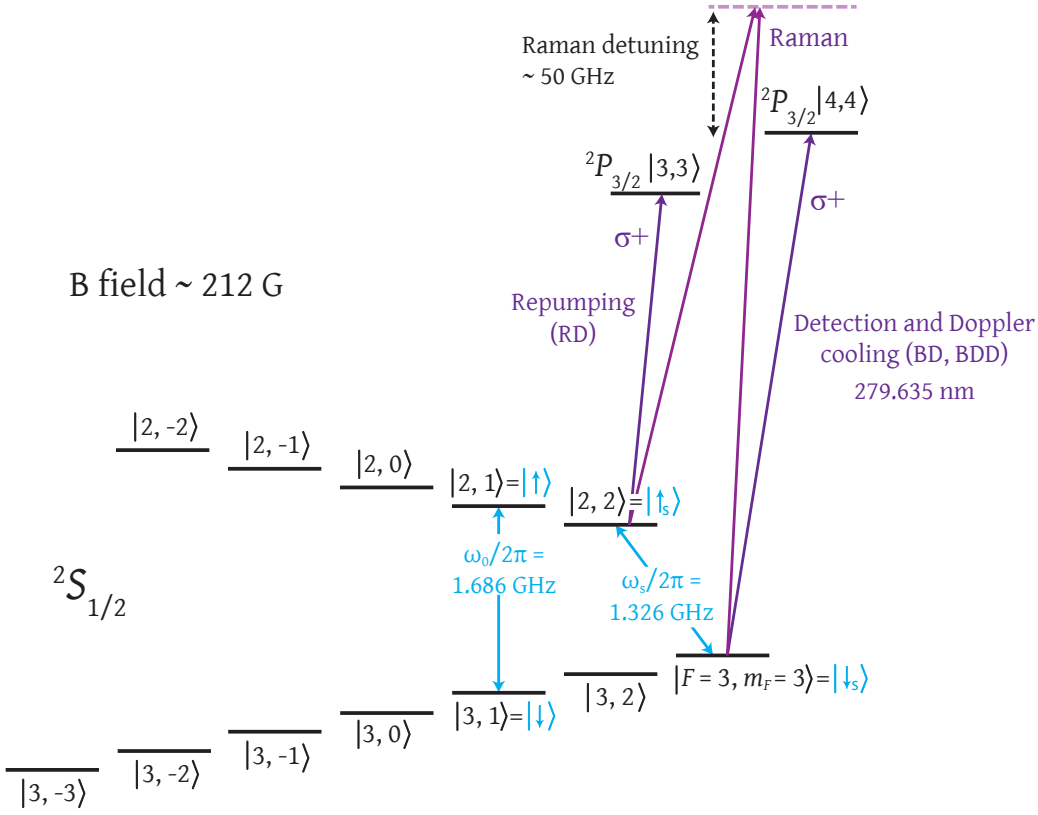

Figure 4.6: Relevant energy level structure (not to scale) of $^{25}Mg^+$ in a magnetic field of $\simeq 212\,\mathrm{G}$. Arrows indicate lasers or microwaves used to drive the associated transitions. Qubits are encoded in $|\downarrow\rangle \equiv {}^2S_{1/2}\,|3,1\rangle$ and $|\uparrow\rangle \equiv {}^2S_{1/2}\,|2,1\rangle$. The qubit frequency is first-order insensitive to magnetic field fluctuations.

4.4 State preparation and detection

Any experimental run starts with loading ions into the trap using laser-based photoionization and Doppler cooling. After loading, we perform experiments to minimize micromotion for optimal cooling and detection. This is achieved by systematically moving the ion(s) towards the rf null with DC potentials, based on measurements of the transverse and out-of plane micromotion. After compensating the micromotion, we perform several procedures to optimize the position of laser beams on the ion(s) and to measure the frequencies of important microwave transitions in the

$^2S_{1/2}$ ground state manifold. Once the micromotion compensation and calibration experiments are complete (some iteration may be required), we can proceed to physics experiments.

We typically initialize the ion(s) in the $|\downarrow\rangle$ qubit state and close to the $|n = 0\rangle$ motional state at the start of each shot of a physics experiment. State preparation begins with a stage of Doppler cooling to reduce the average motional occupation to $\bar{n} \sim 2$. This is followed by a sequence of coherent microwave pulses and dissipative optical repumping to prepare the ion's internal state in $|3, 3\rangle$. Resolved sideband cooling then serves to cool the motional mode(s) used in the experiment closer to the ground state. State preparation is completed after the internal state is transferred from $|3, 3\rangle$ to $|\downarrow\rangle$ using coherent microwave pulses. At the end of an experiment we need to measure our qubits. We apply microwave pulses to transfer or "shelve" the populations of the $|\downarrow\rangle$ and $|\uparrow\rangle$ states in the $|3, 3\rangle$ and $|2, -1\rangle$ states respectively. Detection of fluorescence from the $^2S_{1/2}\,|3, 3\rangle \leftrightarrow$ $^2P_{3/2}\,|4, 4\rangle$ cycling transition indicates the ion was projected into the $|\downarrow\rangle$ qubit state.

Each of the stages of state preparation, detection, and micromotion compensation are discussed in more detail in the subsections below. The laser systems used to implement these operations are described in section 4.5. The microwave drive chain is discussed in section 4.6.

4.4.1 Doppler cooling

We use two laser beams tuned below resonance with the dipole allowed $^2S_{1/2}\,|3, 3\rangle \leftrightarrow {}^2P_{3/2}\,|4, 4\rangle$ cycling transition for Doppler cooling $^{25}Mg^+$ ions. The center frequency and natural linewidth of the transition are 1072.084547(5) THz (at 0 B field) and $\Gamma = 2\pi \times 41.3(3)$ MHz respectively [71]. Both beams are σ^+ polarized and have a $1/e^2$ beam intensity radius of $\sim 14\,\mu$m at the location of the ions. The wavevectors of both beams have components along every normal mode direction, allowing Doppler cooling in three dimensions.

The "blue Doppler" (BD) laser is red detuned by $\Delta \simeq \Gamma/2$ from the line center. In the weak binding regime, where $\Gamma/2 \gg \omega_m$, with ω_m the frequency of a particular motional mode, the steady

state temperature that is achieved by Doppler cooling is given by [60, 72]

$$T_D = \frac{\Gamma}{8k_B}(1+\xi)\left[(1+s)\frac{\Gamma}{2\Delta} + \frac{2\Delta}{\Gamma}\right], \tag{4.1}$$

where the saturation parameter is given by $s = 2|\Omega|^2/\Gamma^2$, with Ω the resonant Rabi frequency, and ξ is a geometric factor related to the average component of photon emission recoils along the axis of oscillation with a value of $\xi = 2/5$ for dipole radiation [60]. T_D is minimized for $\Delta = \Gamma\sqrt{s+1}/2$. For a single trapped $^{25}Mg^+$ ion with a radial trapping frequency of $\omega_m =\sim 2\pi \times 6\,\mathrm{MHz}$, and saturation parameter $s \simeq 0.5$ we measure an average thermal occupation of $\bar{n} \simeq 2.0$ after Doppler cooling and blue sideband analysis (chapter 3).

The second laser, labeled "blue Doppler detuned" (BDD), is shifted by 522 MHz below the BD frequency. For this beam we use a saturation parameter of $s \sim 10$, so that an ion Doppler shifted into resonance will see a power broadened line. This beam provides cooling for ions that are excited to high velocities by background gas collisions, where cooling with the BD is not efficient. Another important function of the BDD is to perform optical pumping, within the $F = 2$ manifold (and to some extend the $F = 3$ manifold as well), towards the towards the $|F = 3, m_F = 3\rangle$ state.

4.4.2 Repumping

Doppler cooling on the $^2S_{1/2}\,|3,3\rangle \leftrightarrow\ ^2P_{3/2}\,|4,4\rangle$ transition ideally optically pumps the ion into the $^2S_{1/2}\,|3,3\rangle$ state. However, polarization impurities in the BD beam result in population being transferred to other states within the $^2S_{1/2}$ manifold, predominantly to the $|3,2\rangle$ and $|2,2\rangle$ states. To transfer this population back to $|3,3\rangle$, we use coherent microwave pulses and a repump (RD) laser resonant with the $^2S_{1/2}\,|2,2\rangle \leftrightarrow\ ^2P_{3/2}\,|3,3\rangle$ transition. The RD is σ^+ polarized and is derived from the same laser source as the BD and BDD beams. The repumping sequence starts with microwave carrier π pulses on the $|3,3\rangle \leftrightarrow |2,2\rangle$ and $|3,2\rangle \leftrightarrow |2,2\rangle$ transitions. This is followed by an RD pulse, which effectively transfers population from $|2,2\rangle$ to both $|3,2\rangle$ and $|3,3\rangle$, and a microwave π pulse on the $|3,3\rangle \leftrightarrow |2,2\rangle$ transition. This dissipation sequence is repeated several times to transfer population from the $|3,3\rangle$ and $|2,2\rangle$ states to the $|3,2\rangle$ state. Finally, coherent

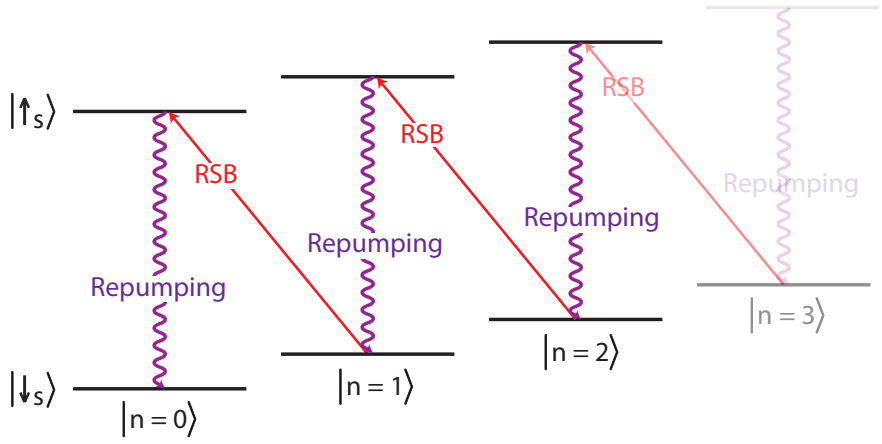

Figure 4.7: Ground state cooling. Red sideband (RSB) pulses induce transitions from $|\uparrow_s\rangle|n\rangle$ to $|\downarrow_s\rangle|n-1\rangle$. Dissipative repumping returns the internal state to $|\downarrow_s\rangle$. Population in $|n=0\rangle$ is trapped because a RSB transition from this state is not possible.

microwave pulses transfer the population to $|3,3\rangle$.

Dissipative repumping from the $|2,2\rangle$ to the $|3,3\rangle$ state is also used for resolved sideband cooling which is described in the next subsection.

4.4.3 Resolved sideband cooling

After preparing the ion(s) in the $^2S_{1/2}|3,3\rangle$ state, we use pulsed resolved sideband cooling [40, 73] to cool the ion(s) close to the motional ground state. The process is illustrated in Fig. 4.7. A pair of laser beams with a frequency difference of $\omega_s - \omega_m - \Delta_{ACS}$, where ω_m is the frequency of the mode being cooled and $\Delta_{ACS}/2\pi \sim 400\,\text{kHz}$ is the AC Stark shift from the laser fields, implement a red sideband (RSB) interaction (see Chapter 3) that induces transitions from $|\downarrow_s\rangle|n\rangle$ to $|\uparrow_s\rangle|n-1\rangle$. The Raman beams are derived from the same laser source and both are detuned from the $^2P_{3/2}$ state by $\sim 50\,\text{GHz}$ (Fig. 4.6). This detuning is chosen such that the rate of off-resonant scattering from the $^2P_{3/2}$ manifold is much less than the sideband Rabi rate. Interleaving RSB pulses with dissipative repumping results in a net flow of population towards the $|n=0\rangle$ motional state, which is a dark state (eigenstate with eigenvalue 0) of the RSB Hamiltonian.

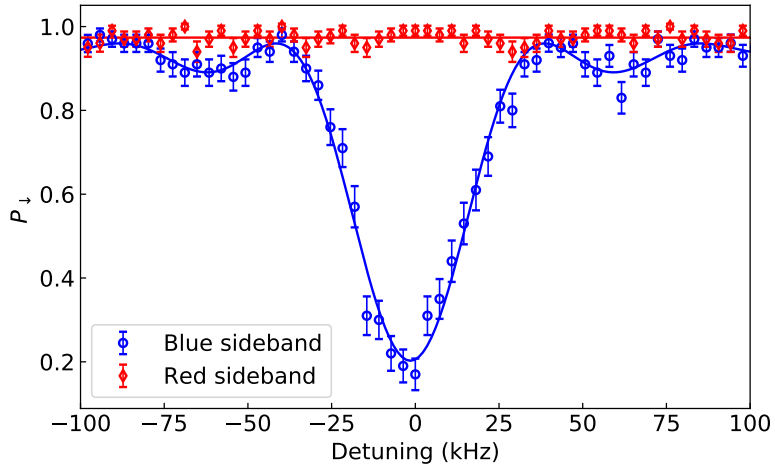

Figure 4.8: Fluorescence counts as a function of the Raman red and blue sideband detuning after ground state cooling. From the data we extract $\bar{n} = 0.03(2)$.

We measure the motional occupation after sideband cooling by comparing the probabilities of measuring $|\downarrow_s\rangle$, $P_{\downarrow_s}^{RSB}$ and $P_{\downarrow_s}^{BSB}$, after excitation with either the red or blue sideband respectively [40]. To eliminate systematic effects, an effective blue sideband (BSB) is implemented by first applying a microwave π pulse to flip the internal state from $|\downarrow_s\rangle$ to $|\uparrow_s\rangle$ and then applying an RSB pulse. A final carrier π pulse is applied before detection. As described in [60], the average motional occupation, assuming that the final state has a thermal distribution, is given by

$$\bar{n} = \frac{R}{1-R}, \tag{4.2}$$

where $R = \dfrac{P_{\downarrow_s}^{RSB}}{P_{\downarrow_s}^{BSB}}$. From the example data shown in Fig. 4.8, we calculate $\bar{n} = 0.03(2)$. Alternatively, we can measure $\bar{n}$ by using blue sideband analysis (see Chapter 3).

4.4.4 Imaging and detection

After ground state cooling, the ion is transferred to the $|\downarrow\rangle$ qubit state with resonant microwave π pulses, completing initialization for an experiment. To read out the qubit state after the experiment, we first apply microwave pulses to "shelve" the populations in $|\downarrow\rangle$ and $|\uparrow\rangle$ to $|3,3\rangle$

and $|2,-1\rangle$ respectively. We then apply a BD pulse resonant with the ${}^2S_{1/2}\,|3,3\rangle \leftrightarrow {}^2P_{3/2}\,|4,4\rangle$ cycling transition. Detection of scattered 280 nm light corresponds to projecting the qubit into the $|\downarrow\rangle$ state, whereas a lack of scattering corresponds to the $|\uparrow\rangle$ qubit state. Scattered photons are collected using an imaging system with a primary objective with a numerical aperture (NA) of 0.4 and magnification of ~ 4, followed by a secondary objective with magnification of ~ 13 and NA of ~ 0.13. Slits in the primary image plane system allow us to block stray light. We can choose to direct scattered photons to either an electron-multiplying charged-coupled device (EMCCD) camera[3] or to a photomultiplier tube (PMT)[4] for counting. In a detection duration of 200 μs with a saturation parameter of $s \sim 0.5$, we record on average $\simeq 50$ counts for a single ${}^{25}Mg^+$ in the bright state and $\simeq 5$ counts in the dark state (fig. 4.9) using the PMT. The dark counts result primarily from detection light scattering off the trap surface.

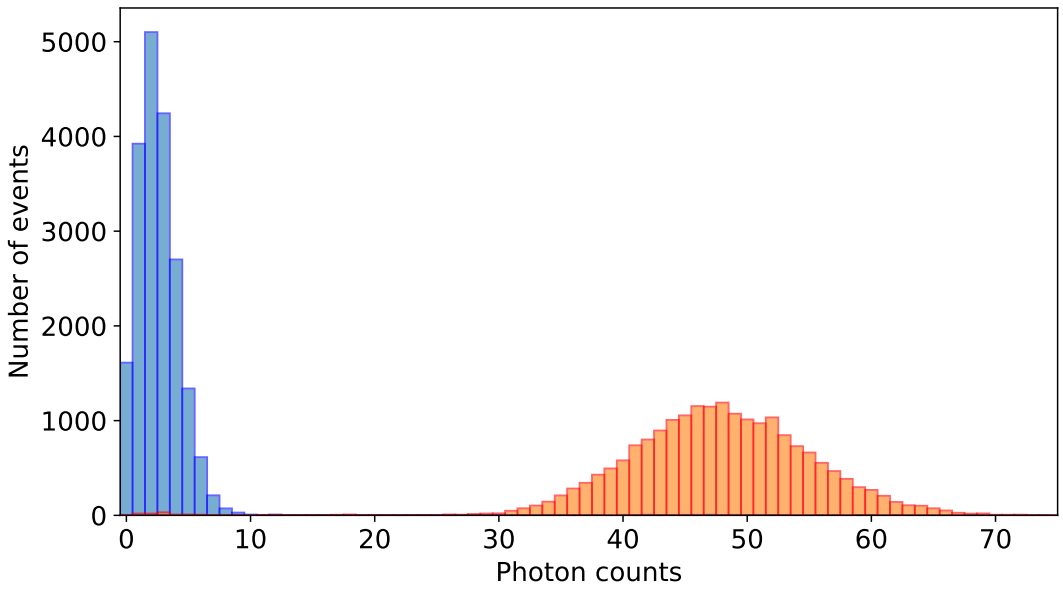

Figure 4.9: Typical detection histogram for a single ${}^{25}Mg^+$ ion for a detection time of 200 μs and a saturation parameter of $s \sim 0.5$. Bars correspond to population in $|\uparrow\rangle = {}^2S_{1/2}\,|2,1\rangle$) (blue) or $|\downarrow\rangle = {}^2S_{1/2}\,|3,1\rangle$ (orange).

[3] Andor DV887ECS-UVB
[4] Hammamatsu R7600U-203

4.4.5 Micromotion compensation

We detect micromotion in the y direction by monitoring the photon scattering rate as a function of the ion position along the y axis. The ion's position is systematically adjusting by changing potentials on the DC electrodes of the trap. As the ion moves away from the trap axis, the micromotion amplitude increases and the ion will start to spend a significant amount of time during a detection period Doppler shifted out of resonance with the detection beam, thus reducing the fluorescence count rate. The in-plane micro-motion is compensated by moving the ion to the position that maximizes the count rate. This method only allow us to know that we have nulled the micromotion parallel to the Doppler beam. Because we have some residual axial micromotion, this compensation technique will end up putting you in a place with some axial and some radial micromotion, such that the total is normal to the Doppler beam. This will be small, but non-zero.

Out-of-plane micromotion (in the z direction) is detected by applying a microwave tone at a frequency of $\omega_0 + \omega_{RF}$ [74]. This technique requires an oscillating magnetic field gradient. The microwave-gradient field will be resonant with the first micromotion sideband, and induce sideband transitions between the qubit states. By adjusting potentials on DC electrodes, we can change the ion's position along z to minimize the transition probability and hence the out-of-plane micromotion.

4.5 Laser systems

This section describes the laser systems used in the experiment. The orientation of the laser beams relative to the magnetic field direction and the trap axis are shown schematically in Fig. 4.10. The amplitude and frequency of the laser beams used for manipulation of trapped ions are controlled using acousto-optic modulators (AOMs). All RF signals used to drive the AOMs are derived from signals generated using direct digital synthesizers (DDSs)[5] that are controlled using a field-programmable gate array (FPGA) board[6] programmed using ARTIQ experimental control

[5] Analog device AD9914 clocked at 2.4 GHz
[6] Xilinx KC705

software [75].

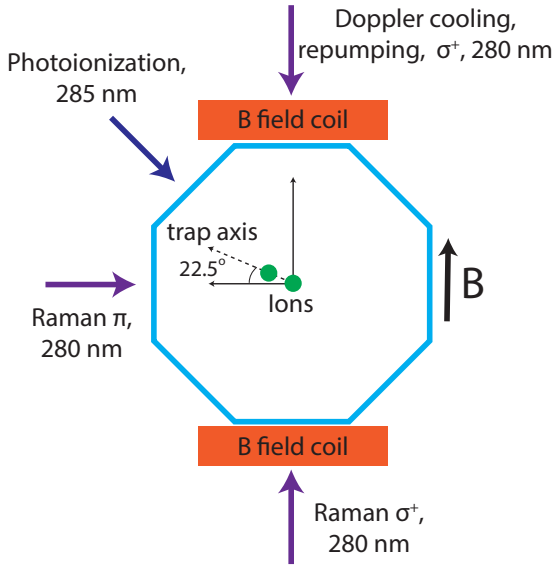

Figure 4.10: Schematic diagram indicating laser access to the vacuum chamber.

4.5.1 Photoionization

Our experiment uses photoionization of neutral ^{25}Mg to load ions into the trap. We generate a thermal beam of neutral magnesium using a resistively heated oven (see Fig. 4.3) containing a sample that is enriched with ^{25}Mg. Laser beams directed through the trapping region can then ionize the magnesium atoms via a two-stage process. In the first step, a 285 nm photon excites the $^1S_0 \leftrightarrow {}^1P_1$ electronic transition in ^{25}Mg. Subsequently, another photon at 285 nm or one at 280 nm (from the Doppler cooling laser) can promote the electron to the continuum.

For the experiments described in this thesis, a Raman-fiber-amplifier-based system was used to generate 285 nm light for photoionization. The fiber amplifier is seeded by an 1140 nm diode laser and outputs $\sim 2\,W$ which is frequency-doubled using a waveguide frequency doubler to produce $\sim 280\,mW$ at 570 nm. The visible light is converted to 285 nm using a build-up cavity containing a beta barium borate (BBO) crystal. Although this system is easily able to generate several hundred mW in the visible, the low efficiency of the subsequent resonant frequency doubling stage

required for generating 285 nm light typically limits the UV power to ~ 1 mW. Luckily, this is plenty for our purposes. The Raman fiber laser system is sufficiently stable that there is no need for active control of the laser frequency. We typically leave it free running and monitor the frequency on a wavemeter[7] , making manual adjustments when necessary (every ~ 5 hours).

4.5.2 Doppler cooling, detection, and repumping

The source of resonant light is a home-built vertical external-cavity surface-emitting laser (VECSEL) system which is described in detail in Appendix D. As shown in figure 4.11, the infrared light from the VECSEL at 1118 nm is converted to 559 nm using a commercial waveguide doubler (NTT-0559-000-A-B-C). With 700 mW from the VECSEL we typically generate 260 mW at 559 nm. The 559 nm beam is split into a main beam ($\sim$190 mW), which is directed to a resonant frequency doubler, and a weaker beam for analysis that is frequency shifted using an AOM in a double pass configuration and directed to a Doppler-free molecular iodine spectrometer (see Fig. 4.12). The Doppler-free absorption features of I_2 provide an absolute frequency reference, enabling us to lock the laser frequency to within 2 MHz. The I_2 spectrometer is based on the setup described in [76] and the error signal is generated using the modulation transfer spectroscopy technique [77]. In contrast to the traditional I_2 lock setup used in the Ion Storage group, which uses an acousto-optic modulator (AOM) for frequency dithering [78], our setup uses an electro-optic modulator (EOM) to phase modulate the pump beam after it is frequency shifted by an AOM. This allows both a higher modulation frequency and a larger moduation depth leading to higher signal-to-noise ratio in the error signal. We typically require ~ 5 mW of 559 nm to enter the spectrometer for a good lock. The error signal from the I_2 spectrometer provides the input to a proportional-integral (PI) controller which adjusts the voltage across the VECSEL piezo transducer (PZT) to stabilize the VECSEL cavity length and thus the laser frequency.

The main 559 nm beam is frequency doubled to 280 nm using an enhancement cavity containing a BBO crystal [79]. As shown in Figure 4.13 the UV light is split and frequency shifted

[7] HighFinesse GmbH WS6-200

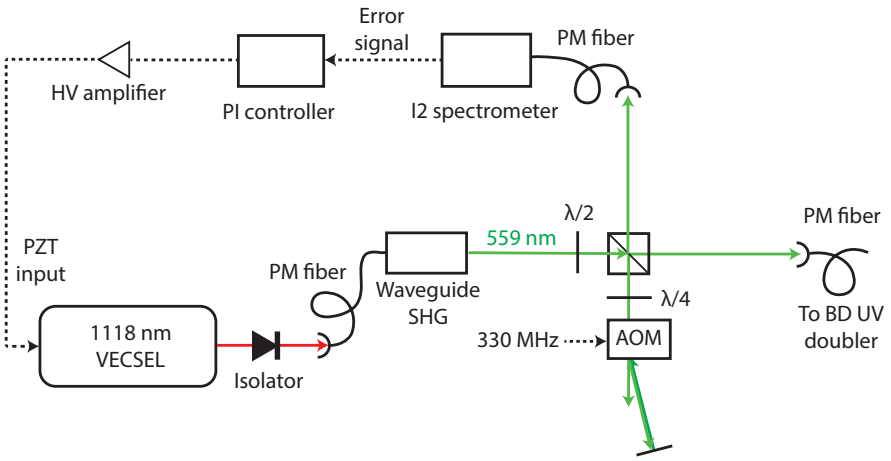

Figure 4.11: Frequency stabilized 559 nm system. Light at 1118 nm from a VECSEL laser is frequency doubled to 559 nm using a waveguide second harmonic generation (SHG) module. A fraction of the 559 nm light is frequency shifted using a double pass AOM for analysis using a Doppler-free iodine spectrometer. A proportional-intergal (PI) controller adjusts the VECSEL piezo (PZT) based on the error signal from the spectrometer. Dotted lines indicate electronic signals.

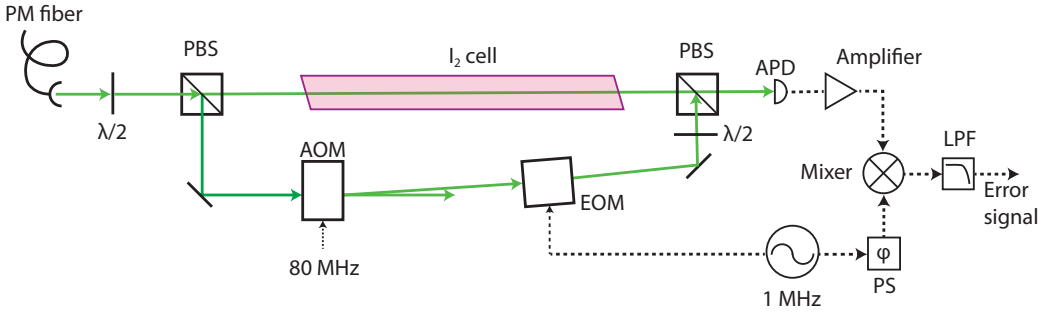

Figure 4.12: Doppler-free iodine spectrometer. Light at 559 nm is delivered via a polarization maintaining (PM) optical fiber. The light is split by polarizing beam splitter (PBS) into probe and pump beams that overlap and counterpropagate through the iodine cell. The pump beam is first shifted by 80 MHz using an AOM. The diffracted beam is phase modulated at 1 MHz using an electro-optical modulator (EOM). Absorption of the probe is detected on an avalanche photodetector (APD). The photodiode signal is amplified, demodulated and filtered to generate an error signal. LPF: Low pass filter, PS: phase shifter. Dotted lines indicate electronic signals.

using AOMs to generate the BD, BDD, and RD beams. Roughly 2% of the UV light is picked off and frequency shifted by 2×205 MHz to generate the RD light. The remaining UV light enters

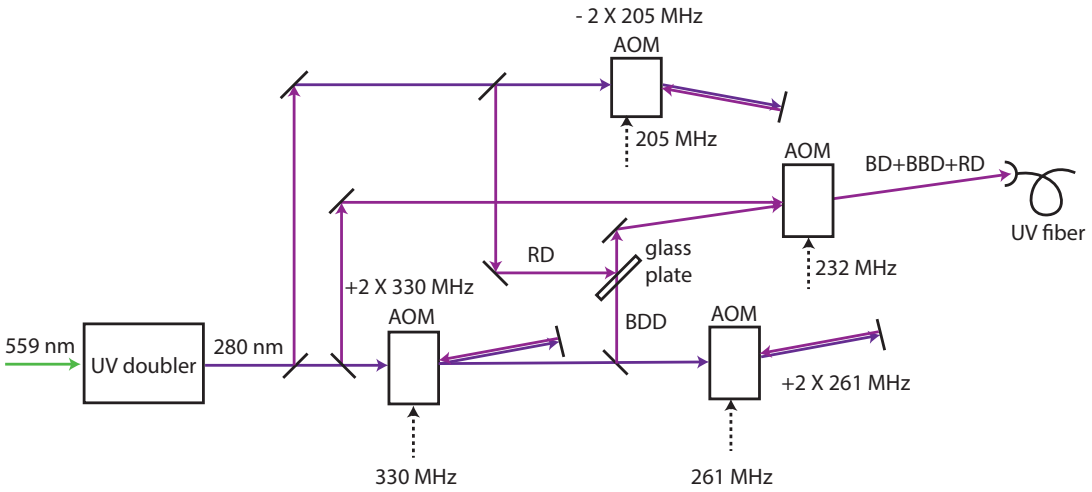

Figure 4.13: AOM switch yard for controlling Doppler cooling and detection (BD and BDD), and repump (RD) light. Dashed lines indicate rf signals for controlling AOMs. The RD, BD, and BDD beams are coupled into the same solarization resistant UV fiber and directed to the ion trap.

a double-pass AOM setup and is frequency shifted by $2 \times 330\,\mathrm{MHz}$. The diffracted light is further frequency shifted by 232 MHz to generate BD light. The residual undifracted light from the 330 MHz double pass AOM is shifted by $2 \times 261\,\mathrm{MHz}$ to produce BDD light. The BD, RD and BDD are coupled into the same solarization resistant UV fiber [80] and routed to the ion trap (see Fig. 4.10).

4.5.3 Raman lasers

As for the resonant laser source, the Raman laser system (see Fig. 4.14) is based a VECSEL emitting at 1118 nm. Infrared light from the VECSEL is frequency doubled twice to generate 280 nm light. The first stage uses a waveguide doubler to generate 559 nm light and the second stage uses a BBO enhancement cavity to produce light at 280 nm. From $\sim 290\,\mathrm{mW}$ of 559 nm light, we typically generate $\sim 10\,\mathrm{mW}$ at 280 nm. The 280 nm light is split into two beams, each of which is frequency shifted using an AOM in double-pass configuration to reach the the required frequency difference. Each Raman beam is coupled into a separate UV fiber and routed to the ion trap (see Fig. 4.10). Polarization optics near the vacuum chamber set the polarization of the lower-frequency Raman beam to σ^+ and that of higher-frequency Raman beam to π.

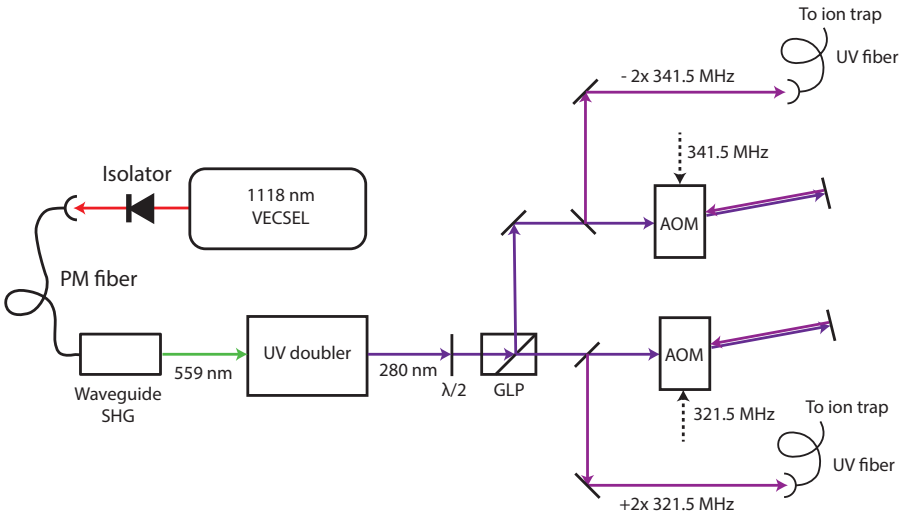

Figure 4.14: Raman laser system. Single-frequency 1118 nm light, generated using a VECSEL laser, is converted to 559 nm using a waveguide SHG module. The 559 nm light is frequency doubled to 280 nm using an enhancement cavity containing a BBO crystal. The UV light is split into two beams using a half-wave plate ($\lambda/2$) and a polarizing beam splitter (PBS) cube. Each beam is frequency shifted using acousto-optical modulators (AOMs) in a double pass configuration and coupled into UV fibers.

4.6 Electronic drives

In our system, we use use magnetic fields for coherent qubit manipulations and magnetic field gradients for spin-motion coupling. We also employ electric fields and electric field gradients to manipulate the motional states of trapped ions. All of these fields are generated by direct digital synthesis. Figure 4.15 shows the relevent portion of the surface trap with connections for the electronic drives. All drive signals are generated using DDSs[8] which are controlled using the same FPGA board and ARTIQ software as the laser AOMs. This enables precision control of the amplitude, frequency, and phase of each each signal.

4.6.1 Microwave drive system

Unlike most ion traps, our trap has integrated current-carrying structures for generating oscillating magnetic fields and near-field gradients[63, 81, 82]. The essential physics can be understood by considering the magnetic field generated by an infinitely long current carrying wire along the x direction (Fig. 4.16). Applying Ampere's law, the magnetic field in the $y-z$ plane is given by

$$\vec{B} = \frac{\mu_0 I}{2\pi}\left(\frac{y\vec{e}_z - z\vec{e}_y}{y^2+z^2}\right), \tag{4.3}$$

where μ_0 is the permeability of free space, and I is the current. At $(y,z)=(0,d)$, the components of the field are $B_y = -\frac{\mu_0 I}{2\pi d}$ and $B_z = 0$, and the magnetic field gradients are

$$\frac{\partial B_y}{\partial z} = \frac{\partial B_z}{\partial y} = \frac{\mu_0 I}{2\pi d^2}, \quad \text{and} \quad \frac{\partial B_y}{\partial y} = \frac{\partial B_z}{\partial z} = 0 \tag{4.4}$$

Coherent operations for state preparation, detection, and qubit manipulation require tones at multiple frequencies ranging from 1.326 to $\sim 2.0\,\mathrm{GHz}$. Depending on Δm_F between the levels of the particular transition, we require magnetic filed components either parallel to ($\Delta m_F = 0$) or transverse to ($\Delta m_F = \pm 1$) to the static quantization magnetic field. The $|{\downarrow}\rangle \leftrightarrow |{\uparrow}\rangle$ transition has

[8] Analog device AD9914 clocked at 2.4 GHz

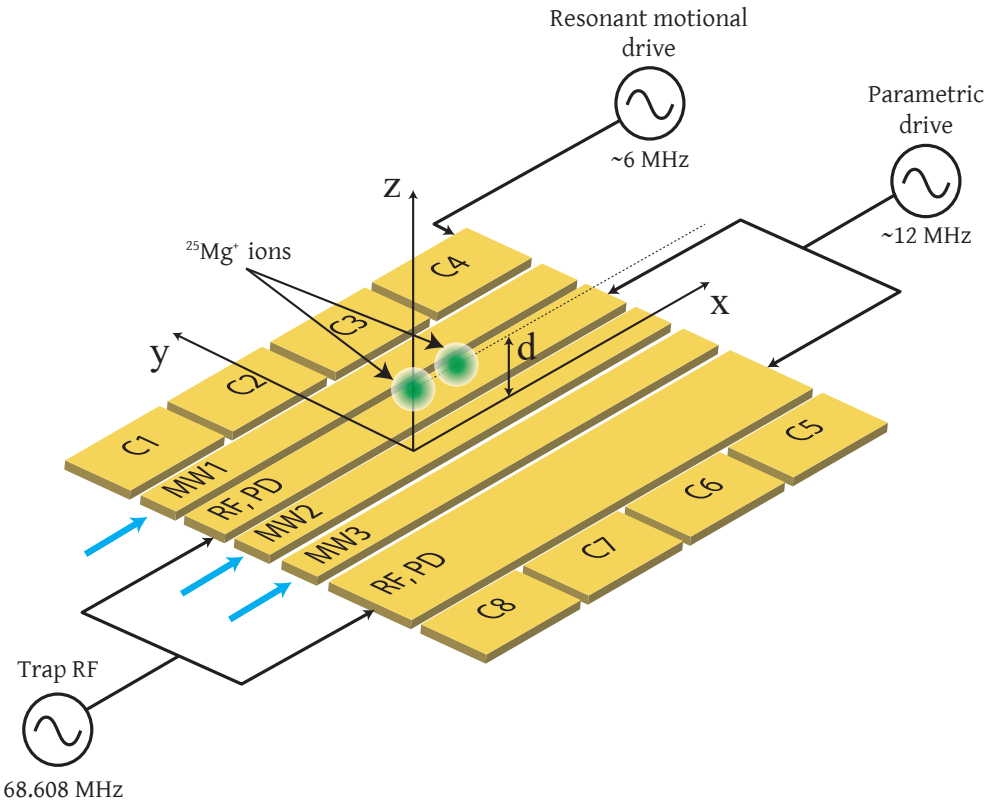

Figure 4.15: Schematic diagram of the relevant portion of the surface-electrode ion trap. Microwave currents (inidicated by blue arrows) in electrodes MW1, MW2 and, MW3 generate magnetic field gradients for spin-motion coupling. The resonant electric field drive signal is applied to DC electrode C4. The parametric drive (PD) is applied directly to the RF electrodes of the trap.

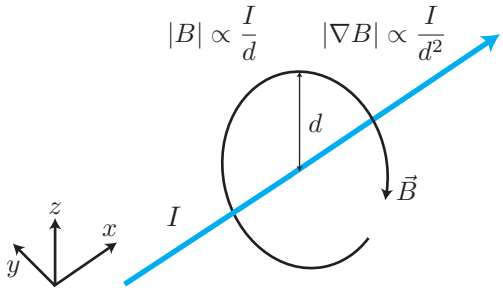

Figure 4.16: A current $I\vec{e}_x$ flowing along a wire of negligible transverse extent generates a magnetic field that curls around the wire. The magnitude of the field falls off like $1/d$, and the magnetic field gradients $\partial B_z/\partial y$ and $\partial B_y/\partial z$ fall off like $1/d^2$.

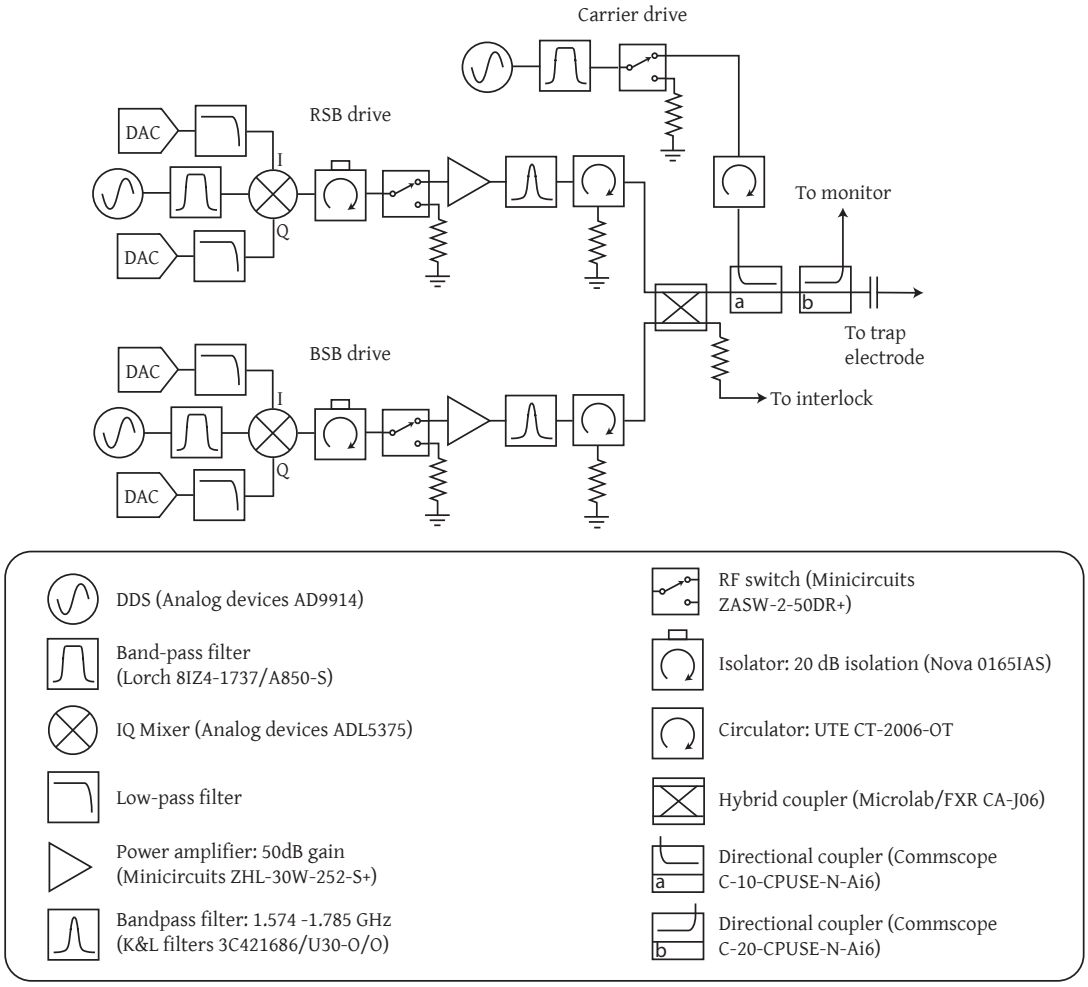

Figure 4.17: Microwaved drive system for generating carrier, red sideband, and blue sideband signals. This entire system is duplicated three times for each of the trap electrodes. Low pass filters are homebuilt Gaussian filters with a measured 3 dB cutoff frequency of ~ 30 MHz.

$\Delta m_F = 0$ and hence requires π polarized microwaves. As the currents in the trap are at a 67.5° angle to the quantization B field, the Rabi rate (Chapter 3 Eq. 3.14) for carrier transition on the clock qubit is roughly

$$\Omega_0 = \cos(67.5^\circ)\frac{\mu_{||}B_y}{\hbar} = \cos(67.5^\circ)\frac{\mu_{||}\mu_0 I}{2\pi\hbar d}, \tag{4.5}$$

with $\mu_{||} \approx 1\mu_B$ [83] and μ_B is the Bohr magneton. Plugging in the numbers shows that carrier Rabi frequncies of $\Omega_0/2\pi \sim 1$ MHz can be achieved with $\sim 10\,\text{mA}$ current amplitude. For spin-motion coupling, we need much higher currents to generate sufficiently strong near-field oscillating magnetic field gradients. Oscillating currents at $\omega_{RSB} = \omega_0 - \omega$ and $\omega_{BSB} = \omega_0 + \omega$ give sideband interactions (see Chapter 3) [9] . Assuming the motional-mode direction $\vec{q}$ is parallel to the y axis (Fig. 4.15), an order of magnitude estimate of the sideband interaction strength can be obtained from Eq.3.15

$$\Omega = \cos(67.5^\circ)\frac{\mu_{\|}(\nabla B.\vec{q})q_0}{\hbar} = \cos(67.5^\circ)\frac{\mu_{\|}\mu_0 q_0 I}{2\pi\hbar d^2} \tag{4.6}$$

which shows that we would need a factor of $d/x_0 \approx 6 \times 10^3$ more microwave current to achieve a Rabi frequency comparable to Ω_0. In experiments, we typically measure sideband Rabi rates of ~ 2 kHz corresponding to current amplitudes of $\sim 0.1\,\text{A}$ (from Eq. 4.6). Each sideband field also causes an AC Zeeman shift $\Delta_{ACZ} \propto -\Omega^2/(\omega_{SB} - \omega_0)$, where ω_{SB} is the sideband angular frequency [69]. The AC Zeeman shift can be measured using a Ramsey experiment, where the sideband fields are applied during the time between the Ramsey carrier $\pi/2$ pulses. For this measurement it is important to detune (by several Ω) the magnetic field gradients away from the sideband resonances ($\omega_0 \pm \omega$) so as not to excite the ion's motion. For typical settings we measure $|\Delta_{ACZ}/2\pi| \sim 15$ kHz for the blue sideband and $|\Delta_{ACZ}/2\pi| \sim 5$ kHz for the red sideband. Unless otherwise stated, in subsequent discussions, I will always include the AC Zeeman shift in the definition of the qubit frequency i.e. $\omega_0 \to \omega_0 + \Delta_{ACZ}$.

[9] Note the difference between the coordinate system used in this chapter and in chapter 3

A schematic of the microwave chain used to drive currents in one microwave electrode of the trap is sketched in Figure 4.17. Each chain has components for generating carrier, red sideband, and blue sideband signals. There is a separate chain for each of the three microwave electrodes. Each signal tone is generated by a DDS clocked at 2.4 GHz followed by a bandpass filter that selects the first Nyquist image. The temporal envelope of the sideband signals is modulated using an IQ mixer that is controlled by a 100 MSPS, arbitrary wave form generator [65]. The signal is then amplified by ∼47 dB and filtered using a narrow-band cavity filter. The two sideband signals are then combined with a hybrid coupler. The signal leaving one output port is attenuated and sent to an interlock circuit that shuts off the input signals to the power amplifiers if the reflected power from the trap exceeds a preselected value. The signal leaving the other port of the hybrid is combined with the carrier signal using a directional coupler and capacitively coupled to the trap through a 50 Ohm characteristic impedance SMA cable. On the trap chip, the microwave signals are coupled into 50 Ohm strip lines that taper down in the trap region (Fig. 4.2). Immediately after the trap, the electrodes are grounded to enforce a current anti-node boundary condition near the trapping region. In this configuration, almost all of the microwave power delivered to the trap is reflected.

4.6.2 Resonant motional drive

As described in Chapter 2, applying an oscillating force at the resonance frequency of a harmonic oscillator displaces the oscillator in a frame rotating at ω. We implement an oscillating force on a trapped ion by applying an oscillating potential (also known as a "tickle") to one of the DC electrodes of the surface trap (Fig. 4.15). The potential is generated using a switched, amplified DDS. The oscillating potential results in an oscillating electric field at the position of the ion which gives a force $F(t) = qE_0 \sin(\omega t + \phi)$, where E_0 is the component of the electric field along the direction of oscillation of the mode of interest. In the frame rotating at ω (after making the

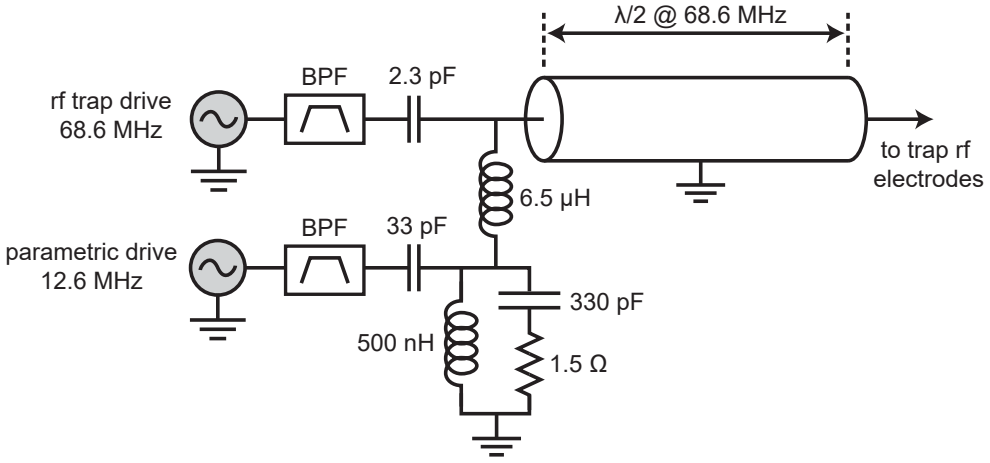

Figure 4.18: Circuit for combining the parametric drive with the trap rf drive. BPF: Band-pass filter

rotating wave approximation), the Hamiltonian is given by

$$\hat{H} = -\frac{\hbar\Omega}{2i}(\hat{a}e^{-i\phi} + \hat{a}^{\dagger}e^{i\phi}), \tag{4.7}$$

where $\Omega = \dfrac{qE_0x_0}{\hbar}$. The time evolution operator $\hat{U}(t) = e^{\frac{\Omega t}{2}(\hat{a}e^{-i\phi}+\hat{a}^{\dagger}e^{i\phi})} = \hat{D}(\alpha(t))$, is a displacement operator with displacement amplitude $\alpha(t) = \dfrac{\Omega t}{2}e^{-i\phi}$.

4.6.3 Parametric drive

Parametric modulation is implemented by applying an oscillating potential near 2ω to the rf electrodes of the surface trap (Fig. 4.15). This modulates the trapping potential in the radial plane. Applying the parametric drive to the rf electrodes ensures that the electric field curvature at the position of the ion can be strongly modulated with minimal residual electric field oscillating at the parametric drive frequency which might cause off-resonant excitation of the ion secular motion. The drive signal is filtered using a band-pass filter with a bandwidth of $\sim 2\,\mathrm{MHz}$ to prevent unwanted noise, particularly near ω, reaching the trap. We use a resonant tank circuit with series inductance (Fig. 4.18) to combine the parametric drive with the trap rf drive before the coaxial resonator.

As described in Chapter 2, modulation of the confining potential of a harmonic oscillator at

2ω realizes in the interaction Hamiltonian for degenerate parametric modulation

$$\hat{H} = \frac{\hbar g}{2}(\hat{a}^2 + \hat{a}^{\dagger 2}), \tag{4.8}$$

where g is the parametric coupling strength. Applying the Hamiltonian for a duration t implements the squeezing operator $\hat{U}(t) = e^{\frac{-igt}{2}(\hat{a}^2+\hat{a}^{2\dagger})} = \hat{S}(\xi)$, with the squeezing parameter $\xi = igt$. From an electric field simulation of the trap, we estimate that a parametric drive amplitude of $\sim 20\,\mathrm{mV}$ results in $g \sim 50\,\mathrm{kHz}$.

Chapter 5

Laser-free control of the trapped-ion quantum harmonic oscillator

The previous chapters described the theoretical and experimental tools required to generate and control non-classical states of trapped-ion motion using laser-free methods. This chapter presents the experimental implementation of these methods for the generation and analysis of thermal mixed states, number states, coherent states, squeezed states, and squeezed cat states. Furthermore, the calibration and analysis procedures described in this chapter are essential for the experiments presented in later chapters.

5.1 Motional state analysis

Since we cannot measure the motional state of our trapped ions directly, we need to map the motional state onto the ion's qubits states. As described in chapter 3 we can accomplish this using either sideband interactions or spin-dependent forces. Chapter 3 describes the theory of sideband analysis for the case where there is no decoherence of either the qubit or oscillator state. As the coherence time of our "clock" qubits is several orders of magnitude larger than the duration of our experiments (typically a few ms), qubit decoherence is usually negligible. The effects of motional decoherence are taken into account using either full numerical simulations from a master equation or by incorporating phenomenological decay factors following [19]. For the latter, Eq 3.24 which gives the probability of of finding the ion in the $|\downarrow\rangle$ state after applying a blue sideband for duration

t becomes

$$P_{\downarrow}(t) = \frac{1}{2}\left(1 + \sum_{n=0}^{\infty} P_n e^{-\gamma_n t}\cos\left(\sqrt{n+1}\Omega t\right)\right), \tag{5.1}$$

where we assume the phenomenological decay constants depends on n according to $\gamma_n = \gamma_0\sqrt{n+1}$ [20]. To avoid unnecessary exercise of the fingers of the reader, P_n are the probabilities of measuring the oscillator in Fock state n (before application of the sideband), and Ω is the Rabi rate. Similarly for red sideband analysis

$$P_{\downarrow}(t) = \frac{1}{2}\left(1 + \sum_{n=0}^{\infty} P_n e^{-\gamma_n t}\cos\left(\sqrt{n}\Omega t\right)\right). \tag{5.2}$$

5.2 Thermal distribution

After Doppler cooling, an ion's motion is (theoretically) thermally distributed. Indeed, red-sideband analysis after Doppler cooling a $^{25}Mg^{+}$ ion (5.1) shows that the measured population distribution is in good agreement with a thermal mixed state. Sideband-analysis using magnetic field gradients also allows us to extract the mean thermal occupation $\bar{n}$. For the data shown in Fig. 5.1, $\bar{n} = 2.89(3)$.

Doppler cooling is typically followed by resolved-sideband cooling to bring the motional occupation closer to zero. As $\bar{n}$ gets smaller, $P_{\downarrow}(t)$ measured using RSB analysis tends to 1 (Fig. 5.1 a). Furthermore, the high frequency oscillations present in the Doppler-cooled data are largely absent after ground state cooling, indicating that population in higher-order motional states has been transferred to the ground state. Numerical simulations suggest that the slow decay of $P_{\downarrow}(t)$ for the ground-state-cooled data results from motional decoherence during the analysis pulse.

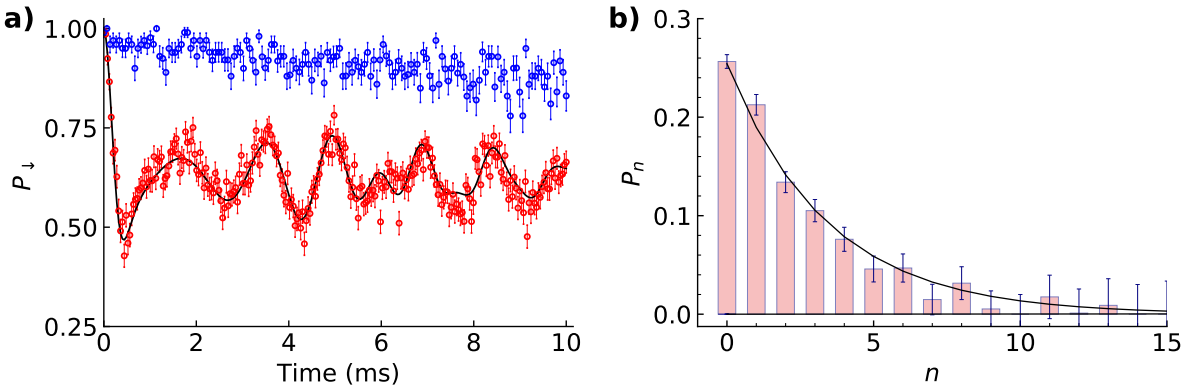

Figure 5.1: Red sideband analysis of a thermal state. a) $P_\downarrow$ as a function of the red sideband pulse duration t, after Doppler cooling (red points) and following ground sate cooling (blue points). The solid black curve is a theoretical fit to the data assuming a thermal distribution. The mean thermal occupation from the fit is $\bar{n} = 2.89(3)$. b) Number state populations obtained by fitting an unconstrained number state distribution to the data in a). The black line indicates P_n for a thermal distribution with $\bar{n} = 2.89$. Error bars indicate one standard deviation of the mean.

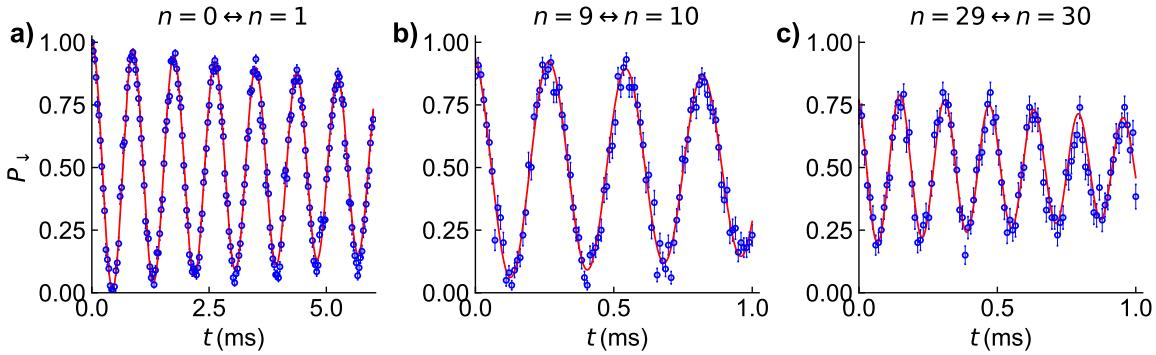

Figure 5.2: $P_\downarrow$ as a function of the blue sideband duration t, after preparing the system in Fock states with $n = 0$ (a), $n = 9$ (b), $n = 29$ (c). The solid red curves are fits of decaying sinusoids (Eq. 5.3) to the data. The fitted Rabi frequencies are $\Omega_0/2\pi = 1.1439(8)\,\mathrm{kHz}$, $\Omega_9/2\pi = 3.60(1)\,\mathrm{kHz}$, and $\Omega_{29}/2\pi = 6.20(2)\,\mathrm{kHz}$. Error bars indicate one standard deviation of the mean.

5.3 Number states

Once the ion has been prepared in the motional ground state, we can use sequences of sideband and carrier pulses to prepare higher-order number states. Starting in the state $|\downarrow\rangle\,|n = 0\rangle$, a sequence k blue sideband π pulses each followed by a carrier π pulse will prepare the state $|\downarrow\rangle\,|k\rangle$. Figure 5.2 shows BSB flopping data after preparing the number states $|0\rangle$, $|9\rangle$, and $|29\rangle$. The Rabi frequency Ω for each is obtained by fitting to the data an exponentially decaying sinusoid of the form

$$P_\downarrow(t) = \frac{1}{2}\left(1 + ae^{-\gamma t}\cos(\Omega t + \phi)\right), \tag{5.3}$$

where, a, γ, ϕ, and Ω are fitting parameters. For a sideband interaction generated using magnetic field gradients, we expect the Rabi frequency for flopping between $|n\rangle\,|\downarrow\rangle$ and $|n+1\rangle\,|\uparrow\rangle$ to depend on n according to $\Omega_n = \Omega_0\sqrt{n+1}$ (this assumes the magnitude of the magnetic field varies linearly over the spatial extent of the ion). The experimentally measured Rabi frequencies closely follow this relationship up to at least $n = 50$ (Fig. 5.3). The loss of contrast of the Rabi oscillations as n is increased (Fig. 5.2), results mainly from motional heating and dephasing during the time required to prepare the number state.

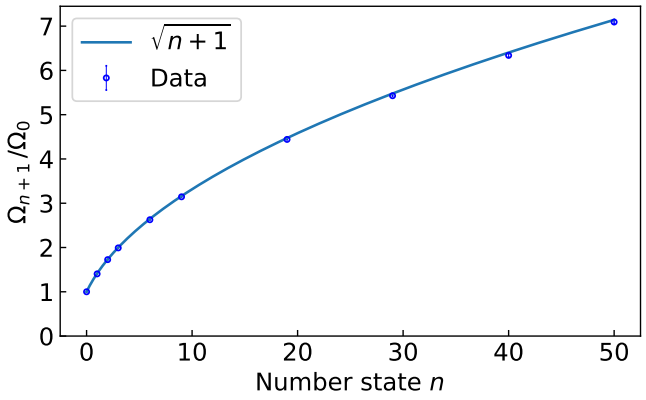

Figure 5.3: Sideband Rabi frequencies as a function of n, corresponding to the initially prepared number state $|n\rangle$. Points indicate experimentally measured values. Error bars are smaller than the data points. The solid curve plots $\sqrt{n+1}$.

5.4 Coherent states

In section 2.4 I described how coherent states of motion can be generated from the ground state by applying an oscillating electric field at ω for a duration t. Example data for sideband analysis of a coherent state is shown in Fig. 5.4. $P_{\downarrow}(t)$ clearly shows a revival similar to the "Jaynes Cummings revival" [30] at $\sim$ 2.4 ms BSB pulse duration. This revival is a signature of a two-level system (TLS) coupled to an oscillator which is initially prepared in a coherent state. The Jaynes Cummings interaction is usually discussed in context of cavity quantum electrodynamics, where the coupling between an electric field mode and the TLS is mediated by the cavity. Here the coupling between the trapped-ion mechanical oscillator and its internal states is achieve using the sideband interaction (strictly speaking the Jaynes Cummings interaction is equivalent to the red sideband interaction). The coherent state amplitude α is extracted by fitting Eq. 5.1 to the data, assuming a coherent state distribution for P_n (Eq. 2.15). The Fock state populations extracted from the fit (Fig. 5.4 b) show good agreement with the theoretically expected Poisson distribution with amplitude $|\alpha| = \Omega_r t/2$.

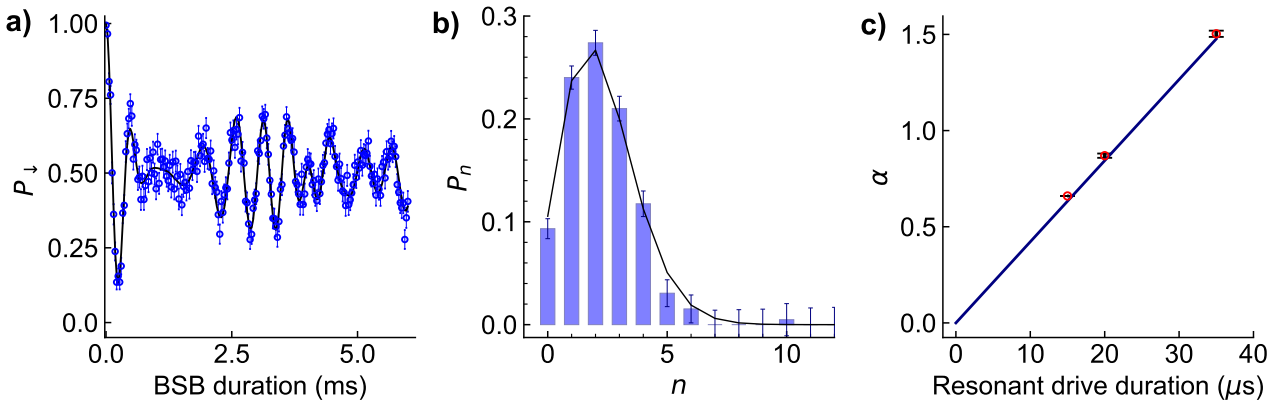

Figure 5.4: Blue-sideband analysis of a coherent state. a) $P_\downarrow$ as a function of the blue sideband pulse duration. The solid black curve is a theoretical fit to the data assuming a coherent state distribution giving $\alpha = 1.50(2)$. b) Number state populations obtained by fitting an unconstrained number state distribution to the data in a). The black line indicates P_n for a coherent state with $\alpha = 1.50$. Error bars indicate one standard deviation of the mean. c) Displacement amplitude $|\alpha|$ as a function of the resonant drive duration. Points indicate values of α obtained using BSB analysis as in a). A straight line fit to the data gives the resonant drive coupling strength $\Omega_r/2\pi = 6.71(7)$ kHz.

5.5 Squeezed states

Squeezed states are prepared by applying the electronic parametric drive at 2ω for a fixed duration duration t_s. If the ion is initially prepared in the motional ground state, the resulting state is know as a squeezed ground or vacuum state. A signature of a squeezed ground state is that it should contain only even Fock state populations (see chapter 2). We see this clearly in the Fock state populations determined using BSB analysis (Fig5.5 b). BSB flopping data (Fig5.5 a) can be used to extract the magnitude of the squeezing parameter r and also the parametric coupling strength g. The parametric coupling strength g, determines how fast a squeezed state can be prepared. Since $r = gt_s$, a plot of r vs t_s should give a straight line with a slope given by g. An example calibration plot is shown in Fig 5.5 c.

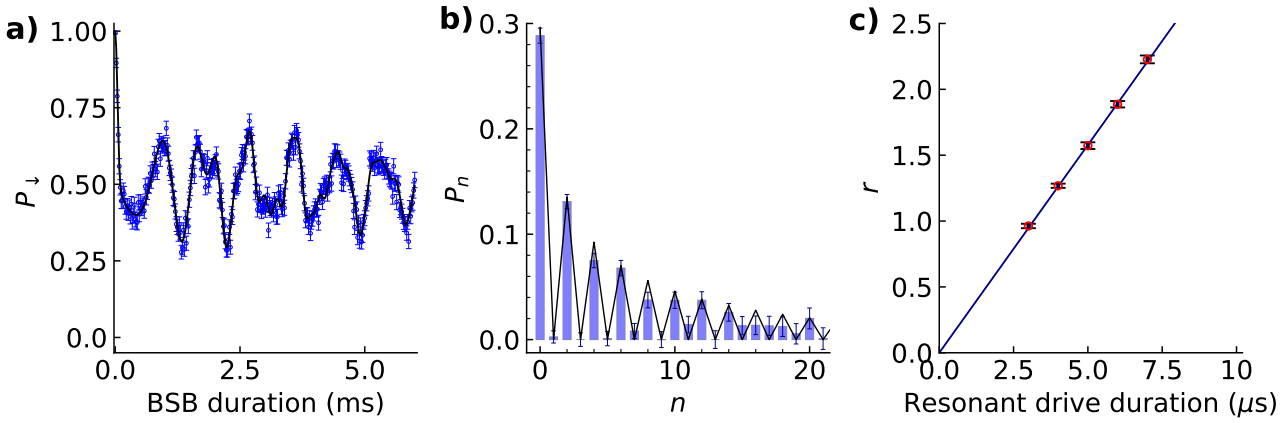

Figure 5.5: Blue-sideband analysis of a squeezed state. a) $P_\downarrow$ as a function of the blue sideband pulse duration. The solid black curve is a theoretical fit to the data assuming a squeezed state distribution giving $r = 1.89(2)$. b) Number state populations obtained by fitting an unconstrained number state distribution to the data in a). The black line indicates P_n for a squeezed ground state with $r = 1.89$. Error bars indicate one standard deviation of the mean. c) Squeezing parameter r as a function of the resonant drive duration. Points indicate values of r obtained using BSB analysis as in a). A straight line fit to the data gives the parametric drive coupling strength $g/2\pi = 50(2)\,\mathrm{kHz}$.

5.6 Squeezed cat states

While sideband analysis of squeezed states allows us to extract the magnitude of the squeezing parameter, it does not provide information about the coherence or orientation of squeezed states in phase space. The phase-sensitive nature of squeezing can be clearly revealed by using spin-dependent forces (SDFs) to generate superpositions of oscillator wavepackets. Depending of the orientation of the initial squeezed state and the direction of the SDF, measurements of the qubit state can have very different outcomes (Chapter 3). For the situation shown in Fig 5.6, a SDF that acts in the $\hat{\sigma}_x$ basis is applied to an ion initially prepared in $|\downarrow\rangle|\xi = re^{i\theta}\rangle$. The final overlap of the wavepackets associated with the $|+\rangle$ and $|-\rangle$ spin states is larger if the squeezing phase is $\theta = \pi$ (SDF along the antisqueezed direction) than if $\theta = 0$ (SDF along the squeezed direction). The probability of finding the ion in $|\downarrow\rangle$ is clearly larger if $\theta = \pi$.

The generation of squeezed Schrödinger cat states and squeezed-state analysis using SDFs has been demonstrated by the ETH group [84]. In their experiment, the initial squeezed state was prepared by a dissipative method [20] and the SDF was generated using lasers. Motivated by these results, we decided to generate squeezed cat states in our system using laser-free methods. We prepare an ion in the $|\downarrow\rangle|\xi = re^{i\theta}\rangle$, where the squeezing is performed using parametric modulation of the trapping potential. We then apply the SDF, which is generated using magnetic field gradients, for a duration t, and finally we detect. As expected (see Chapter 3), the probability of finding the ion in $|\downarrow\rangle$ depends on the phase of the parametric drive relative to the spin-dependent force (Fig. 5.7). For comparison we also performed the experiment for an initial ground state ($r = 0$). While the data for the squeezed and the ground state cases gives good agreement with analytical theory, the antisqueezed case does not. Numerical simulations suggest that motional decoherence from fast dephasing and heating (see section 3.5), and shot-to-shot fluctuations of the motional mode frequency can account for some of the discrepancy. The physical picture is that the wavpacket overlap is more sensitive to small phase-space rotations if the squeezed wavepackets are nominally aligned along their major axes. I suspect that the remaining discrepancy is present because the spin-

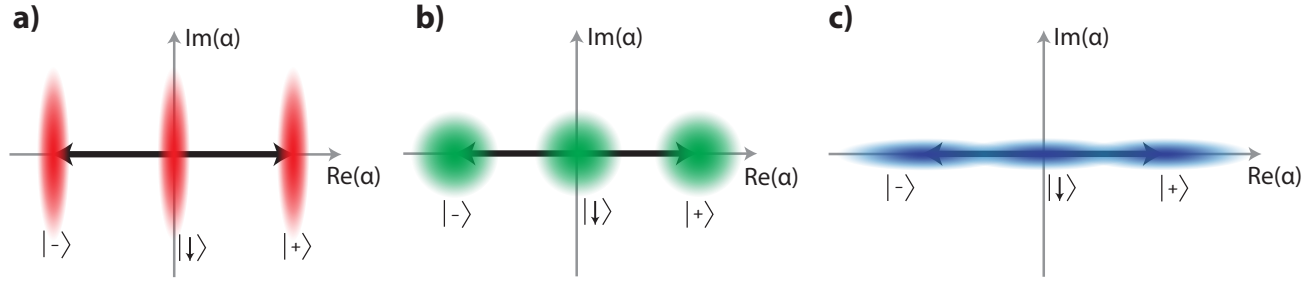

Figure 5.6: Squeezed cat states in phase spaces. In each panel an identical spin-dependent displacement (indicated by black arrows) is applied along the real axis to an ion initially prepared in the $|\downarrow\rangle$ qubit state and in a motional state with a) squeezing along Re(α) axis ($\theta = 0$) , b) the ground state ($r = 0$), and c) squeezing along the Im(α) axis ($\theta = \pi$).

dependent force was not configured correctly when these data were taken. For the data shown here, the SDF force was generated using the Bermudez scheme [85] where a single sideband is applied together with a strong carrier field. For reasons we don't fully understand, we found it difficult to reliably set the carrier amplitude to give a reproducible spin-dependent force (Numerical analysis by Harty et al. [86], shows that the fidelity of two-qubit gates implemented using the Bermudez scheme can be very sensitive to the carrier to sideband Rabi frequency ratio).

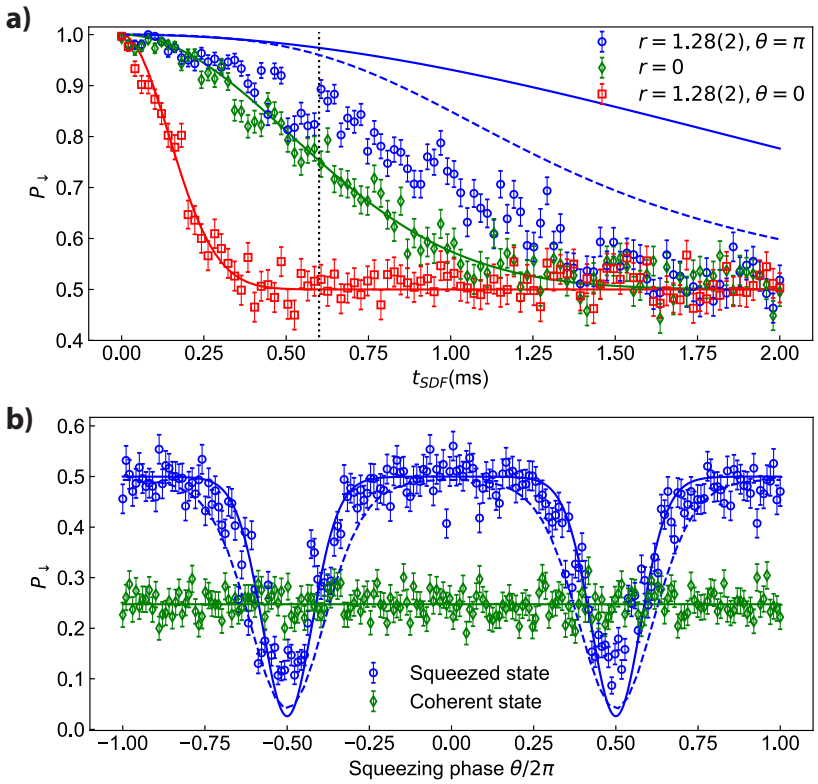

Figure 5.7: Squeezed cat state experimental data. a) $P_\downarrow$ as a function of the spin-dependent force duration t_{SDF} for a Shrödinger cat state with and without squeezing. The solid curves are analytical theory (Eq. 3.37). The value of the squeezing parameter ($r = 1.28(2)$) was obtained from the fit of the analytical theory to the red data points (with $\theta = 0$). The dashed curve is from a numerical model incorporating known motional decoherence mechanisms. b) $P_\downarrow$ as a function of the parametric drive phase θ at $t_{SDF} = 60\,\mu s$ (dashed black line in a).

Chapter 6

Quantum amplification of trapped-ion motion

In this chapter and in [87], I describe a technique for amplifying coherent displacements of a mechanical oscillator with initial magnitudes well below the zero-point fluctuations. By applying two orthogonal squeezing interactions, before and after a small displacement, the displacement can be amplified, ideally with no added quantum noise. We have implemented this protocol with a trapped-ion oscillator and measured an increase by a factor of up to 7.3(3) in sensitivity to small displacements. This technique could aid the detection of weak forces and the search for new physics, in particular a dark matter axion-like field [88, 89].

Mechanical oscillators are essential components in an increasing variety of precision sensing applications including gravitational wave detection [90], atomic force microscopy [91], cavity optomechanics [92], and measurement of weak electric fields [93]. However, the attainable knowledge of an oscillator's motional state is limited by unavoidable quantum fluctuations that are present even if the oscillator is in its ground state. By squeezing the oscillator's motional state improved measurement precision for one observable can be achieved at the expense of increased fluctuations of the conjugate observable [6]. Although squeezed states have been created in a variety of physical systems (See Chapter 1), exploiting squeezing for enhanced metrology has been challenging. In particular, noise added during the detection process limits the metrological enhancement unless it is smaller than the squeezed noise. The requirement of low-noise detection can be overcome by increasing the magnitude of the signal to be measured, provided the noise does not significantly increase. In optical interferometry [94] and in spin systems [95], it has been shown that reversal of

squeezing interactions can magnify small phase shifts, relaxing detection requirements [96]. Photon field displacements in microwave cavities have also been amplified using similar phase-sensitive amplification schemes [97, 98].

6.1 Noiseless amplification of displacements

Here I describe a protocol based on reversible squeezing for ideally noiseless phase-sensitive amplification [6] of mechanical oscillator displacements. This amplification method (Fig. 6.1) is applicable to any harmonic oscillator where reversible squeezing can be implemented faster than system decoherence. By first squeezing the motional ground state, quantum fluctuations along a particular phase space quadrature are suppressed. A small test displacement $\hat{D}(\alpha_i)$ (to be amplified) is then applied along the squeezed axis. At this stage, although the signal-to-noise ratio for measuring α_i has been improved by squeezing, resolution below the zero-point fluctuations would require a detection method with yet lower noise. Finally, by reversing the squeezing interaction, the oscillator returns to a minimum-uncertainty coherent state with a larger amplitude $\alpha_f = G\alpha_i$, where G is the gain. Ideally, this process adds no noise in either quadrature. For an oscillator described using creation and annihilation operators $\hat{a}^\dagger$ and $\hat{a}$, the amplification is given by the expression [99]

$$\hat{D}(\alpha_f) = \hat{S}^\dagger(\xi)\hat{D}(\alpha_i)\hat{S}(\xi), \tag{6.1}$$

where $\hat{D}(\alpha) = \exp(\alpha\hat{a}^\dagger - \alpha^*\hat{a})$ is the displacement operator, and $\hat{S}(\xi) = \exp(\frac{1}{2}(\xi^*\hat{a}^2 - \xi\hat{a}^{\dagger 2}))$ is the squeezing operator with the complex squeezing parameter $\xi(r,\theta) = re^{i\theta}$ (see chapter 2). For arbitrary orientations of the displacement α_i with respect to the initial squeezing axis, $\alpha_f = \alpha_i \cosh(r) + \alpha_i^* e^{i\theta}\sinh(r)$. Maximum amplification is achieved if the displacement is along the squeezed axis (where $\arg(\alpha_i) = \theta/2$), giving $G = e^r$.

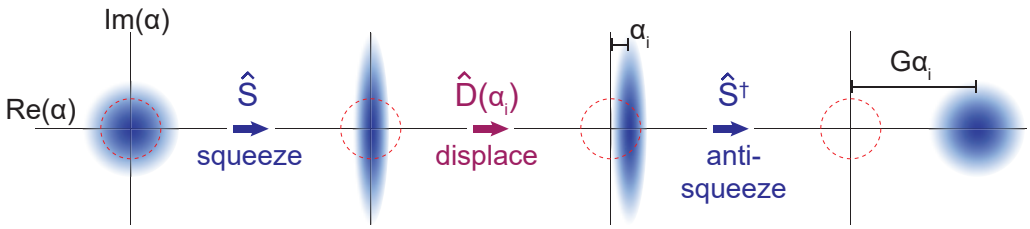

Figure 6.1: Conceptual illustration of the amplification protocol. Each panel shows a cartoon phase space quasiprobability distribution in a frame rotating at the oscillator frequency. A displacement α_i of an initially squeezed ground state is amplified by subsequent reversed squeezing ("anti-squeezing"), resulting in a final coherent state with amplitude $G\alpha_i$ with no added noise. Dashed red circles indicate the characteristic extent of the initial ground state fluctuations.

6.2 Experimental implementation

This amplification technique was demonstrated using a single trapped $^{25}Mg^{+}$ ion as the mechanical oscillator (details of the experimental apparatus are given in chapter 4). Experiments were performed on a radial motional mode of the ion with frequency $\omega_r \simeq 2\pi \times 6.3\,\mathrm{MHz}$ and zero-point wavefunction extent of $\simeq 5.7\,\mathrm{nm}$. To analyze the motional state, we use the "clock" qubit states $|\downarrow\rangle \equiv |F = 3, m_F = 1\rangle$ and $|\uparrow\rangle \equiv |F = 2, m_F = 1\rangle$ within the $^2S_{1/2}$ manifold. In each experiment, the ion was initialized in the electronic ground state $|\downarrow\rangle$ and close to the motional ground state $|n = 0\rangle$ with optical pumping, resolved-sideband laser cooling, and microwave pulses as described in chapter 4. The motional state of the ion was analysed using blue sideband analysis (see chapters 3 and 5). The sideband interactions were generated using oscillating magnetic field gradients (see chapters 3 and 4). Applying a sideband interaction for various durations results in qubit Rabi oscillations with multiple frequency components whose amplitudes depend on the Fock state populations. Squeezing and displacement operations are implemented using electronic drives as described in chapters 2-5.

To characterize the unitarity of the squeezing operations, we measured the ground state population using a red sideband π pulse after squeezing and anti-squeezing, which would ideally yield perfect overlap $\langle 0|\,\hat{S}^\dagger \hat{S}\,|0\rangle = 1$ (Fig. 6.2). Imperfections of the operation lead to a decrease in

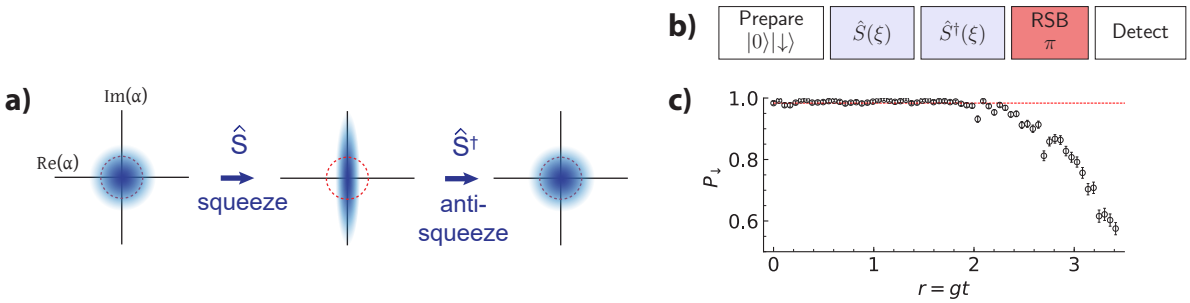

Figure 6.2: Unitary squeezing. a) Illustration of the experiment. The ion is initially prepared in the motional ground state. A squeezed state is then generated by parametric modulation. Finally the inverse squeezing interaction is applied to bring the oscillator back to the ground state. b) Pulse sequence. After squeezing and anti-squeezing a red sideband (RSB) analysis π pulse can flip the qubit state from $|\downarrow\rangle$ to $|\uparrow\rangle$ if oscillator is not returned to the ground state. c) Probability of measuring $|\downarrow\rangle$ after the RSB pulse. Even without squeezing, there is $\sim 2\,\%$ residual population in $|\uparrow\rangle$ after the RSB pulse due to imperfect state preparation and motional heating during the analysis pulse. This background is indicated by the red line.

the observed overlap as r is increased. For $r < 2$, $P_\downarrow \approx 0.98$, which is consistent with the measured value without squeezing and anti-squeezing ($r = 0$). The population in $n = 0$ remains above 0.93 for $r < 2.37(3)$, or $20.6(3)$ dB of squeezing[1] .

After each operation of the amplification process, the Fock state composition of the ion's motional state was analyzed using sideband analysis (Fig. 6.3). The ion is first prepared in the motional and electronic ground state $|0\rangle|\downarrow\rangle$. Interactions ($\hat{S}(\xi)$, $\hat{D}(\alpha_i)$, and $\hat{S}^\dagger(\xi)$) that transform the motional state are then applied in sequence. A blue sideband pulse is then applied for a variable duration and the internal state is detected. Fitting Eq. 5.1 to the data as a function of the interaction duration, and assuming an underlying distribution for P_n from Eq. 2.15, 2.36, or 2.49 as appropriate, allows us to extract best fit values for parameters characterizing the assumed form of the motional state. We also separately fit Eq. 5.1 to the data assuming no particular underlying distribution for P_n, giving the Fock state populations of the motional state being analyzed. Error bars for fitting parameters are calculated as the square root of the corresponding diagonal elements of the least-squares covariance matrix. We repeated this process for several different values of the squeezing strength and calculate the measured amplification gains as the ratio α_f/α_i. The measured gain for various values of the squeezing parameter $r = gt$ closely follows the theoretically expected exponential growth of the coherent state amplitude (Fig. 6.4).

[1] The conversion from r to decibels of squeezing is calculated according to $\mathrm{dB}_{\mathrm{squeezing}} \equiv 20\log_{10}(e^r)$ [100].

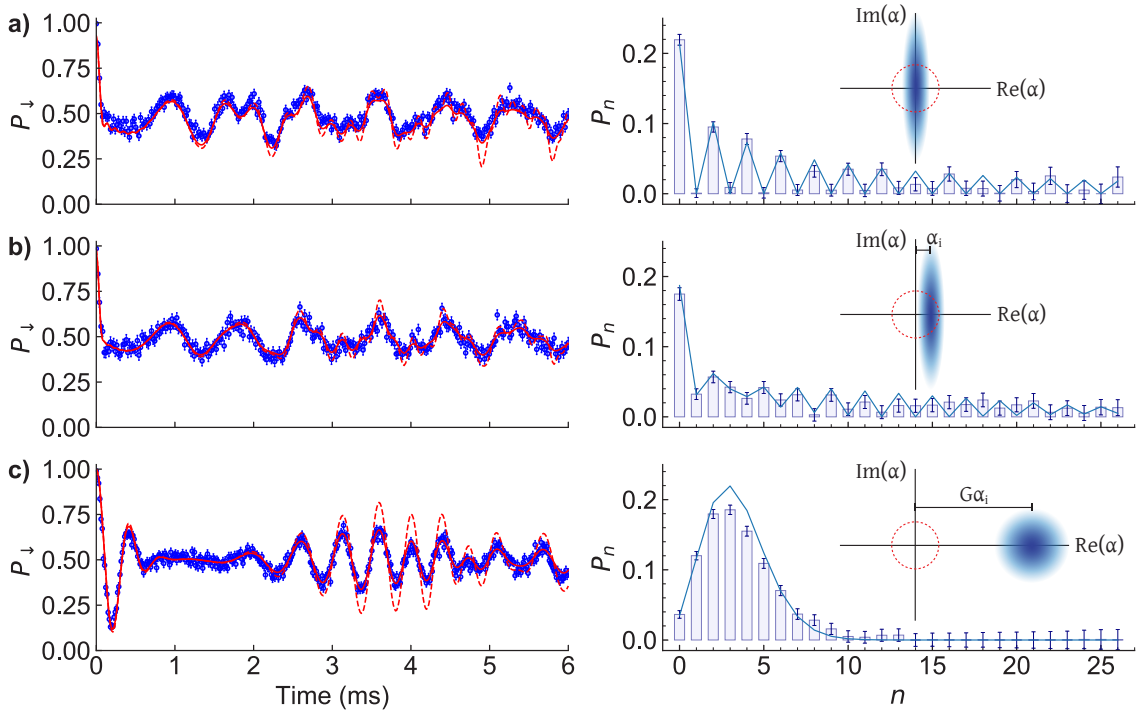

Figure 6.3: Fock state population analysis. a), b), and c) show BSB Rabi oscillations (left column) and corresponding fitted Fock state population histograms (right column). Solid red lines are fits assuming parameterized functional forms of the ideal Fock state populations, yielding values of r, α_i, and as described in the main text. Dashed red lines are parameterized functional forms that do not include decoherence. Histograms are derived by fitting to an unconstrained population distribution. Insets show Wigner function illustrations of the corresponding motional states. a) Initial squeezed motional ground state with $r = 2.26(2)$. b) After displacing this state by $\alpha_i = 0.200(2)$. c) Final coherent state with amplitude $\alpha_f = 1.83(1)$, following the reversed squeezing operation. The initial displacement is amplified by $G = \alpha_f/\alpha_i = 9.17(9)$. Error bars in the first column indicate one standard deviation of the mean, and in the second column 68% confidence intervals.

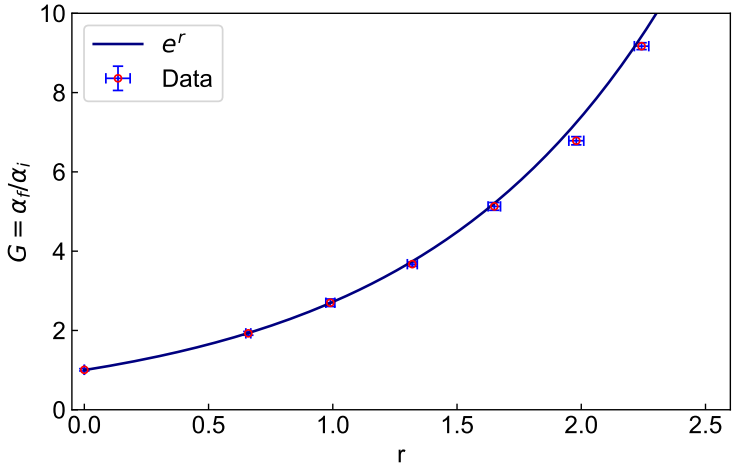

Figure 6.4: Measured gain as a function of the squeezing parameter r. The solid line is the theoretical gain $G = e^r$. Error bars in all figures indicate 68% confidence intervals.

6.3 Quantum-enhanced displacement measurements

Using this amplification technique, we achieve increased sensitivity when measuring displacements much smaller than the zero-point fluctuations. To map the final displacements α_f onto the qubit states, we use a phase-sensitive red sideband (PSRSB) method [47] (Fig. 6.6a). For displacements with $|\alpha| \ll 1$, this method gives measurement sensitivities proportional to $|\alpha|$, which is the standard quantum limit for a displacement measurement. The linear scaling enables straightforward measurement of the amplification gain and is desirable for measuring small displacements. I first give a intuitive description of the PSRSB method that is valid for small displacements, and then give a derivation that is valid for all orders of $|\alpha|$. The ion is first prepared in the motional ground state $|\psi\rangle = |\downarrow\rangle|0\rangle$. A small displacement of the motional ground state ($|\alpha| \ll 1$) results in a small population transfer out of the ground state, predominantly to the $n = 1$ Fock state. In the interaction picture with respect to the qubit and the harmonic oscillator [41] :

$$|\psi\rangle \rightarrow \hat{D}(\alpha)|0\rangle|\downarrow\rangle \tag{6.2}$$

$$= (\hat{I} + \alpha\hat{a}^\dagger - \alpha^*\hat{a} + ...)|0\rangle|\downarrow\rangle \tag{6.3}$$

$$\approx (|0\rangle + \alpha|1\rangle)|\downarrow\rangle\,. \tag{6.4}$$

The subsequent red sideband π pulse maps the the population in $|1\rangle|\downarrow\rangle$ onto $|0\rangle|\uparrow\rangle$, but leaves the population in $|\downarrow\rangle|0\rangle$ unchanged. The state becomes

$$|\psi\rangle \approx (|\downarrow\rangle - |\alpha||\uparrow\rangle)|0\rangle \tag{6.5}$$

for the case where the phase of the beatnote between the RSB pulse and the displacement has been set to give a qubit rotation about the $\phi = 0$ axis on the Bloch sphere as shown in Fig 6.5. A carrier $\pi/2$ rotation about the ϕ axis then gives

$$|\psi\rangle \approx \frac{1}{\sqrt{2}}\left[(1 - |\alpha|e^{+i\phi})|\downarrow\rangle - (|\alpha| + e^{-i\phi})|\uparrow\rangle\right]|0\rangle\,, \tag{6.6}$$

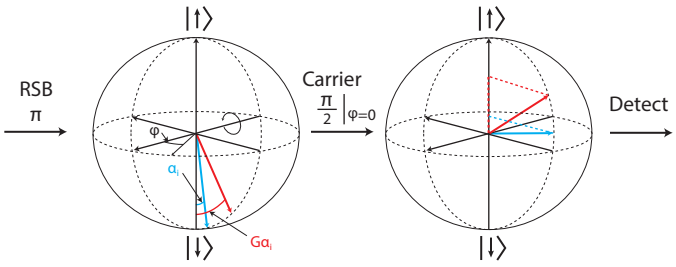

Figure 6.5: Bloch sphere illustration of the phase-sensitive red sideband readout scheme.

showing that the state vector has a phase-sensitive projection onto the polar axis of the Bloch sphere. The probability of finding the system in $|\downarrow\rangle$ is

$$\begin{aligned} P_{\downarrow} &\approx \frac{1}{2}\left|1-|\alpha|e^{i\phi}\right|^2 \\ &= \frac{1+|\alpha|^2}{2} - |\alpha|\cos(\phi) \\ &\approx \frac{1}{2} - |\alpha|\cos(\phi). \end{aligned} \tag{6.7}$$

which shows that $P_{\downarrow}$ sinusoidally oscillates as a function of ϕ with contrast $2|\alpha|$. If the displacement is amplified, then the contrast becomes $2|G\alpha|$ with the requirement that $|G\alpha| \ll 1$. Therefore G can be extracted by measuring the slope of the contrast as a function of $|\alpha|$ provided $|G\alpha|$ is sufficiently small.

Next, I derive the state $|\psi\rangle$ of the ion at the end of the PSRSB sequence for all orders of $|\alpha|$. The state of the ion after the displacement, sideband interaction, and carrier pulse is given by

$$|\psi\rangle = \hat{R}(\pi/2,\phi)\hat{U}_{RSB}\hat{D}(\alpha)\,|\downarrow\rangle\,|0\rangle\,, \tag{6.8}$$

where $\hat{R}(\pi/2,\phi)$ is a spin rotation matrix describing the $\pi/2$ carrier pulse and $\hat{U}_{RSB}$ is the resonant red sideband time evolution operator

$$\hat{U}_{RSB} = e^{-\frac{i\Omega t}{2}(\hat{\sigma}_+\hat{a}+\hat{\sigma}_-\hat{a}^\dagger)}, \tag{6.9}$$

where Ω is the sideband Rabi frequency. The duration t of the RSB interaction is set to give $\Omega t/2 = \pi/2$. The component in $|\downarrow\rangle$ is

$$\begin{aligned} \langle\downarrow|\psi\rangle &= \langle\downarrow|\hat{R}(\pi/2,\phi)\hat{U}_{RSB}\hat{D}(\alpha)|\downarrow\rangle|0\rangle \\ &= \frac{1}{\sqrt{2}}\left(\langle\downarrow| + \langle\uparrow| e^{i\phi}\right)\hat{U}_{RSB}|\alpha\rangle|\downarrow\rangle . \end{aligned} \tag{6.10}$$

The probability of measuring $|\downarrow\rangle$ is therefore

$$\begin{aligned} P_\downarrow &= \frac{1}{2}\Big[1 + e^{i\phi}\langle\downarrow|\langle\alpha|\hat{U}^\dagger_{RSB}|\downarrow\rangle\langle\uparrow|\hat{U}_{RSB}|\alpha\rangle|\downarrow\rangle \\ &\quad + e^{-i\phi}\langle\downarrow|\langle\alpha|\hat{U}^\dagger_{RSB}|\uparrow\rangle\langle\downarrow|\hat{U}_{RSB}|\alpha\rangle|\downarrow\rangle\Big] . \end{aligned} \tag{6.11}$$

Evaluating the matrix elements gives:

$$\langle\uparrow|\hat{U}_{RSB}|\alpha\rangle|\downarrow\rangle = \sum_{l=0}^{\infty}\frac{(-i\frac{\pi}{2})^{2l+1}(1+\hat{n})^l}{(2l+1)!}\alpha|\alpha\rangle , \tag{6.12}$$

and

$$\langle\downarrow|\hat{U}_{RSB}|\alpha\rangle|\downarrow\rangle = \sum_{l=0}^{\infty}\frac{(i\frac{\pi}{2})^{2l}(\hat{n})^l}{(2l)!}|\alpha\rangle , \tag{6.13}$$

where $\hat{n} = \hat{a}^\dagger\hat{a}$ is the harmonic oscillator number operator. Setting the phase of the beatnote between the RSB pulse and the displacement so that the initial rotation is about the $\phi = 0$ axis as before, and inserting equations 6.12 and 6.13 into 6.11 gives

$$\begin{aligned} P_\downarrow &= \frac{1}{2}(1 - |\alpha|f(|\alpha|)e^{i\phi} - |\alpha|f(|\alpha|)e^{-i\phi}) \\ &= \frac{1}{2} - |\alpha|f(|\alpha|)\cos(\phi), \end{aligned} \tag{6.14}$$

where

$$f(|\alpha|) = \sum_{n=0}^{\infty}\frac{e^{-|\alpha|^2}|\alpha|^{2n}}{n!}\left(\frac{\cos(\frac{\pi}{2}\sqrt{n})\sin(\frac{\pi}{2}\sqrt{n+1})}{\sqrt{n+1}}\right). \tag{6.15}$$

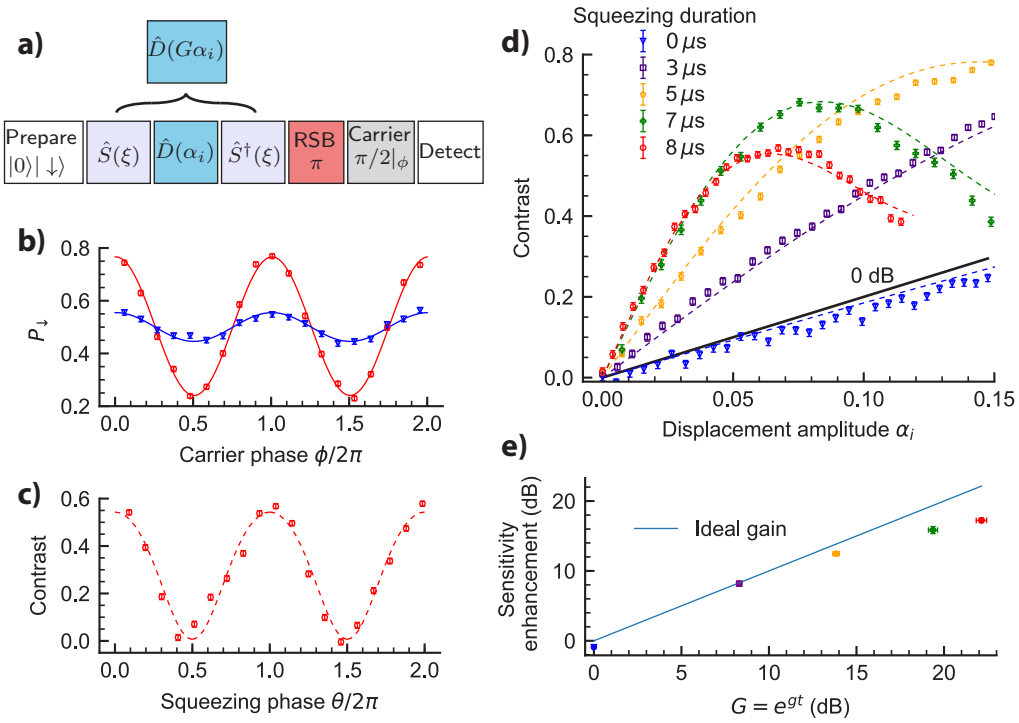

Figure 6.6: Measurement sensitivity enhancement for oscillator displacements. a) Pulse sequence for displacement sensing using phase-sensitive red-sideband (PSRSB) detection. b) Population in $|\downarrow\rangle$ as a function of the carrier $\pi/2$ pulse phase. Blue diamonds are data with no squeezing and red circles are data with amplification. Solid lines show sinusoidal fits to the data. c) Contrast of the carrier phase scan, as shown in b), as a function of the squeezing phase θ for a fixed displacement. d) Contrast as a function of the displacement amplitude $|\alpha_i|$ for different initial squeezing pulse durations. Each data point is calculated from $\approx 10^4$ experiments. The data shown in b) and c) have initial $|\alpha_i| = 0.0578(6)$ and a squeezing duration of $t = 8\,\mu$s (nominally $r = 2.54(3)$). The solid black line is the maximum theoretical contrast without squeezing. Dashed lines in c) and d) are derived from a numerical model that includes motional decoherence. e) Measurement sensitivity enhancement in the linear small-displacement regime as a function of the ideal gain $G = e^{gt}$. For each squeezing duration, the enhancement is determined by dividing the slope of the contrast for $C \leq 0.25$ (obtained by fitting a straight line to data points in d) with $C \lesssim 0.25$) by the slope of the 0 dB black line, which represents the standard quantum limit for a displacement measurement. All error bars represent one standard deviation of the mean.

Equation 6.14 shows that $P_\downarrow$ oscillates sinusoidally with contrast $C(|\alpha|) = 2|\alpha|f(|\alpha|)$ as a function of ϕ. The contrast of the oscillation reaches a maximum value of 0.84 for $|\alpha|$=0.69. If squeezing is used to amplify the displacement, $|\alpha_i| \to G|\alpha_i| = |\alpha_f|$. For $|\alpha_f| \ll 1$, $C(\alpha_f) \approx 2|\alpha_f|$. In comparison, simply measuring the qubit directly after the RSB π-pulse gives a signal $P_\downarrow \propto |\alpha_f|^2$. Without amplification, $\alpha_f = \alpha_i$ and the PSRSB contrast is $C(|\alpha_i|)$. With amplification, the initial displacement amplitude α_i is ideally increased by a factor of G and the PSRSB contrast becomes $C(|G\alpha_i|)$. This increase in contrast is shown in Fig. 6.6b, where the presence of oscillations for the state after amplification indicates that it has a well-defined motional phase. The theory curves in Fig. 6.6b are functions of the form $b + a\cos(\phi)$, with b and a as the fitting parameters. With $8\,\mu$s parametric drive duration for each squeezing pulse and $|\alpha_i| = 0.055(2)$, the fitting parameters are $b = 0.503(3)$ and $a = 0.263(4)$. For the scan with no amplification, the fitting parameters are $b = 0.500(2)$ and $a = 0.055(3)$. The carrier phase dependence in Fig. 6.6b is a feature of the PSRSB method, not of the amplification protocol. Fig. 6.6c highlights the phase-sensitive nature of the amplification protocol by plotting the contrast C of the PSRSB fringe against the squeezing phase θ for a fixed displacement and with $\phi = 0$. Maximum amplification is achieved when the displacement is oriented along the squeezed axis of the initial squeezed state in motional phase space (see Fig. 6.1).

For various parametric drive durations, we measure the contrast of the carrier phase scan signal (Fig. 6.6b), as a function of the displacement amplitude, with the squeezing phase set to maximize the contrast ($\theta = 0$). Experimental data and theory curves are shown in Fig. 6.6d. The displacement amplitude is varied by changing the amplitude of the digital synthesizer that generates the resonant drive. The resonant drive pulse duration is fixed at $5\,\mu$s. For each displacement, the contrast is defined as $C \equiv P_{\downarrow,max} - P_{\downarrow,min}$, where $P_{\downarrow,max}$ and $P_{\downarrow,min}$ are the maximum and minimum values of $P_\downarrow$ of the fringes shown in Fig. 6.6b. The projection noise [101] associated with measuring the contrast is $\sigma(C) = \sqrt{\sigma(P_{\downarrow,max})^2 + \sigma(P_{\downarrow,min})^2}$, where $\sigma(P_{\downarrow,max}) = \sqrt{P_{\downarrow,max}(1 - P_{\downarrow,max})/N_{max}}$ and $\sigma(P_{\downarrow,min}) = \sqrt{P_{\downarrow,min}(1 - P_{\downarrow,min})/N_{min}}$, where $N_{max(min)}$ is the number of measurements taken at the fringe maximum (minimum). The signal-to-noise ratio (SNR) for a displacement measure-

ment is then $s(G) = C(\alpha_f)/\sigma(C(\alpha_f))$. For the case where $|\alpha_f| \ll 1$, the contrast is $C = 2|\alpha_f|$, $P_{\downarrow,min} = P_{\downarrow,max} \approx 0.5$, and $N_{max} = N_{min} = N/2$. The total projection noise is $\sigma(C) = 1/\sqrt{N}$, and hence, the signal-to-noise ratio is $s(G) = 2|\alpha_f|\sqrt{N}$. This is the SNR for a displacement measurement at the standard quantum limit [102].

For a given number of experiments, amplification allows the SNR for a displacement measurement to be improved in comparison to the ideal PSRSB measurement with no squeezing (black solid line in Fig. 6.6d), giving a measurement sensitivity enhancement of $s(G)/s(G = 1)$. For measurements where $C \lesssim 0.25$, the contrast varies linearly with $|\alpha_i|$, and the gain in contrast $C(G\alpha_i)/C(\alpha_i)$ sets a lower bound (which becomes exact as $|\alpha_i| \to 0$) on the measurement sensitivity enhancement, because the projection noise decreases monotonically with increasing contrast. Increasing the squeezing results in increased contrast for $|\alpha_f| \ll 1$, up to a squeezing time of approximately $8\,\mu$s (corresponding to $r = 2.54(3)$, and ideally $22.0(3)\,$dB of squeezing). Here we achieve a contrast gain of 7.3(3), corresponding to a factor of 53(4) reduction in the number of measurements required to achieve a given SNR. The reduction in contrast for larger squeezing durations is attributed mainly to motional heating and motional dephasing. The theory curves (dashed lines) shown in the Figs. 6.6c and d are from numerical simulations incorporating these effects (see section 3.5). The motional heating rate was independently measured to be $\dot{n} = 20(3)\,\text{quanta/s}^{-1}$ and the motional dephasing rate $\Gamma = 18(6)\,\text{s}^{-1}$ was obtained from a least-squares fit to the $8\,\mu$s squeezing duration curve shown in Fig. 6.6d. This motional decoherence is not a limitation of the amplification process or our squeezing method.

The amplification technique described in this chapter can enhance measurement sensitivity in protocols that use phase-stable displacements, such as photon-recoil spectroscopy [47, 103], where the phase of momentum kicks from photon absorption can be controlled by modulating the photon source. Moreover, our method can be extended to amplify displacements of unknown frequency or phase and for amplifying spin-dependent forces to enhance phonon-mediated spin-spin interactions [104, 105], which are used to generate entanglement in quantum simulation and quantum information processing experiments. These advanced parametric amplification protocols

are the subject of the next two chapters.

Chapter 7

Hamiltonian amplification

The Hamiltonian is an operator of fundamental importance in quantum physics. According to Schrödinger's equation,

$$i\hbar\frac{\partial}{\partial t}\left|\psi\right\rangle = \hat{H}\left|\psi\right\rangle, \tag{7.1}$$

the Hamiltonian ($\hat{H}$) determines how a quantum state $|\psi\rangle$ will evolve in time. In experimental quantum physics, it is often desirable to control the rate at which a quantum system evolves from an initial state to a target state. This is often achieved by directly adjusting the strength of $\hat{H}$. For example, if we wish to generate a Bell state in a specific duration t starting from the initial state $|\downarrow\downarrow\rangle$ using the geometric phase gate Hamiltonian (see Chapter 3)

$$\hat{H} = \frac{\hbar\Omega}{2}(\hat{a}e^{i\delta t} + \hat{a}^{\dagger}e^{-i\delta t})(\hat{\sigma}_{x1} - \hat{\sigma}_{x2}), \tag{7.2}$$

we require the coupling strength $\Omega = \frac{2\pi}{t}$. The coupling strength must be set experimentally by adjusting the intensity of the lasers or the magnitude of the magnetic field gradients that are used to implement the gate interaction. However, technical limits prevent arbitrary increases in Ω. Furthermore, the increase in Ω may be accompanied by increased noise that can lead to decoherence or reduced fidelity of the target state.

The recent proposal of Arenz et al.[105] describes an alternative approach for increasing coupling strengths in a broad class of Hamiltonians involving harmonic oscillator interactions. The method uses a sequence of rapid squeezing pulses along alternating quadratures to effectively

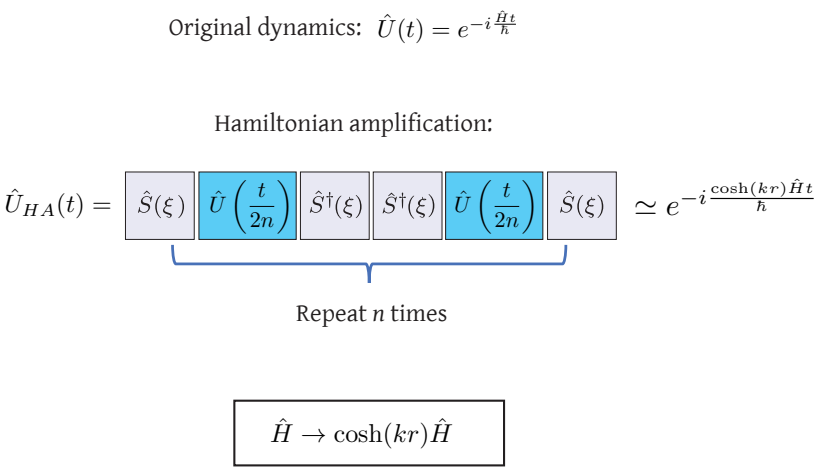

Figure 7.1: Hamiltonian amplification pulse sequence. The Hamiltonian to be amplified ($\hat{H}$ of the form given in Eq. 7.3) is applied within a sequence of squeezing interactions. The overall sequence is repeated n times. If n is sufficiently large, the effective Hamiltonian will converge to $\cosh(kr)\hat{H}$.

amplify the Hamiltonian of interest. The operator sequence required to implement the discrete version of Hamiltonian amplification (HA) is shown in Figure 7.1. Here I will consider Hamiltonians $\hat{H}$ of the form

$$\hat{H} = \beta_1 \hat{x}^k + \beta_2 \hat{p}^k, \tag{7.3}$$

where $\beta_{1,2}$ are constants or operators that do not depend on $\hat{a}$ or $\hat{a}^\dagger$, and k is an integer. For more complicated Hamiltonians refer to [105]. We will assume that the squeezing pulses are configured to give a squeezing parameter of $\xi = r$ so that

$$\begin{aligned} \hat{S}^\dagger(r)\hat{x}\hat{S}(r) &= \hat{x}e^r \\ \hat{S}^\dagger(r)\hat{p}\hat{S}(r) &= \hat{p}e^{-r}. \end{aligned} \tag{7.4}$$

The Hamiltonian amplification process consists of n repetitions of the sequence

$$\hat{S}(\xi)\hat{U}\left(\frac{t}{2n}\right)\hat{S}^\dagger(\xi)\hat{S}^\dagger(\xi)\hat{U}\left(\frac{t}{2n}\right)\hat{S}(\xi), \tag{7.5}$$

where t is the total duration for which $\hat{H}$ is applied and $\hat{U}(\frac{t}{2n}) = e^{-i\hat{H}t/2n\hbar}$. The overall process can be described by the unitary operator

$$\begin{aligned}
\hat{U}_{HA} &= \left[\hat{S}(\xi)\hat{U}\left(\frac{t}{2n}\right)\hat{S}^{\dagger}(\xi)\hat{S}^{\dagger}(\xi)\hat{U}\left(\frac{t}{2n}\right)\hat{S}(\xi)\right]^{n} \\
&= \left[e^{-\frac{it}{2\hbar n}\left(\beta_1\hat{x}^k e^{-r}+\beta_2\hat{p}^k e^{r}\right)}e^{-\frac{it}{2\hbar n}\left(\beta_1\hat{x}^k e^{r}+\beta_2\hat{p}^k e^{-r}\right)}\right]^{n} \\
&= \left[1-\frac{it}{\hbar n}\cosh kr\left(\beta_1\hat{x}^k+\beta_2\hat{p}^k\right)+...\right]^{n} \\
&\simeq e^{\frac{i}{\hbar}\cosh(kr)\hat{H}}, \qquad (7.6)
\end{aligned}$$

for sufficiently large n, becoming exact as $n \to \infty$ by the Trotter theorem [106]. This shows that the Hamiltonian (Eq. 7.3) is effectively amplified by a factor of $\cosh(kr)$. Moreover, the amplification factor does not depend on the phase relationship between the squeezing interactions and the Hamiltonian of interest.

7.1 Amplification of displacements

As described in Chapter 2, displacements of a trapped ion's motional state can be implemented using an oscillating electric field with a frequency ω equal to the frequency of one of the ion's normal modes. After making the rotating wave approximation and transforming into the interaction picture with respect to $\hat{H}_0 = \frac{\hbar\omega_0}{2}\hat{\sigma}_z + \frac{\hbar\omega}{2}\hat{a}^{\dagger}\hat{a}$, the Hamiltonian for the driven oscillator is given by

$$\hat{H}_D = \frac{\hbar\Omega}{2}(\hat{a}e^{-i\theta} + \hat{a}^{\dagger}e^{i\theta}), \qquad (7.7)$$

where $\Omega = qEz_0/\hbar$ is the coupling strength and θ is the relative phase between the co-rotating part of the electric field amplitude and the real axis in the interaction picture. If we choose $\theta = \pi/2$ and the Hamiltonian is applied for a time $\Delta t = t/2n$, the time evolution operator is given by

$$\hat{U}(t) = e^{-i\frac{\hat{H}\Delta t}{\hbar}} = e^{-i\frac{x\hat{p}}{2}} = \hat{D}\left(\frac{x}{2}\right), \qquad (7.8)$$

which is a displacement operator giving a translation of $\frac{x}{2} = \frac{\Omega \Delta t}{4}$ along the real axis in phase space. Applying the squeezing sequence given in Eq. 7.4

$$\hat{S}^{\dagger}(r) e^{-i\frac{x\hat{p}}{2}} \hat{S}(r) = e^{-i\frac{xe^{r}\hat{p}}{2}}, \tag{7.9}$$

and

$$\hat{S}^{\dagger}(-r) e^{-i\frac{x\hat{p}}{2}} \hat{S}(-r) = e^{-i\frac{xe^{-r}\hat{p}}{2}}. \tag{7.10}$$

If we combine these sequences, we get

$$\begin{aligned} \hat{S}(r)\hat{U}(t)\hat{S}(-2r)\hat{U}(t)\hat{S}(r) &= \hat{S}(r)^{\dagger} e^{-i\frac{x\hat{p}}{2}} \hat{S}(r)\hat{S}(-r)^{\dagger} e^{-i\frac{x\hat{p}}{2}} \hat{S}(-r) \\ &= \hat{S}^{\dagger}(r) e^{-i\frac{x\hat{p}}{2}} \hat{S}(r)\hat{S}(r) e^{-i\frac{x\hat{p}}{2}} \hat{S}^{\dagger}(r) \\ &= e^{-ix\frac{(e^{r}+e^{-r})}{2}\hat{p}} \\ &= e^{-ix\cosh(r)\hat{p}}, \end{aligned} \tag{7.11}$$

which is equivalent to a displacement operator $\hat{D}(\cosh(r)x)$. Note that the amplification is formally exact for $n = 1$ and also for any larger values of n. For an arbitrary displacement $\hat{D}(\alpha)$ and a general squeezing interaction $\hat{S}(\xi = re^{i\phi})$, we have

$$\hat{S}^{\dagger}(\xi)\hat{D}(\alpha)\hat{S}(\xi) = \hat{D}(\gamma_1), \tag{7.12}$$

where $\gamma_1 = \alpha \cosh r + \alpha^{*} e^{i\phi} \sinh r$. Similarly,

$$\hat{S}^{\dagger}(-\xi)\hat{D}(\alpha)\hat{S}(-\xi) = \hat{D}(\gamma_2), \tag{7.13}$$

with $\gamma_2 = \alpha \cosh r - \alpha^{*} e^{i\phi} \sinh r$. The combined sequence is given by

$$\begin{aligned}\hat{S}^{\dagger}(\xi)\hat{D}(\alpha)\hat{S}(\xi)\hat{S}^{\dagger}(-\xi)\hat{D}(\alpha)\hat{S}(-\xi)\\ = \hat{D}(\gamma_1)\hat{D}(\gamma_2)\\ = \hat{D}(\gamma_1+\gamma_2)e^{(\gamma_1\gamma_2^{*}-\gamma_2\gamma_1^{*})/2}.\end{aligned} \tag{7.14}$$

which is an overall displacement of $\gamma_1+\gamma_2 = 2\alpha\cosh r$, **independent** of the angle of the squeezing interaction with respect to the displacement direction. The overall geometric phase factor would not affect the outcome of measurements of the spin (the only observable that we measure directly with ions) unless the displacement is spin dependent.

We have performed preliminary experiments with a single trapped ion that demonstrate Hamiltonian amplification of displacements. The ion is initially prepared close to the ground state $|n=0\rangle$ of a radial motional mode with frequency $\omega/2\pi \times 6.8\,\mathrm{MHz}$ and in the $|\downarrow\rangle$ clock qubit state (details about the experimental setup are given in chapter 4). Displacements are implemented by applying an oscillating electric field at ω. Squeezing pulses are implemented by modulating the trapping potential at 2ω, using the electronic parametric drive. The magnitude of the squeezing parameter is set by varying the squeezing pulse time t_s ($r = gt_s$) or by changing the amplitude of the parametric drive. A sequence of squeezing and displacement pulses are applied to give a Hamiltonian amplification sequence with $n = 3$ (see Fig. 7.1). At the end of the amplification sequence, we apply a blue sideband analysis pulse for varying durations to map the resulting motional state onto the ion's qubit states (see chapter 3) which we can measure using fluorescence detection. The sideband is implemented using oscillating magnetic field gradients. We first perform a control experiment where we apply a HA sequence with $n = 3$, but with $r = 0$. For the control, we measure a coherent state amplitude of $\alpha = 0.50(2)$ (Fig. 7.2 a). When the squeezing is turned on, with $r \sim 1.9$, we measure a displacement amplitude of $\alpha = 1.68(3)$ (Fig. 7.2 b). Note that the amplitude and total duration of the resonant drive pulses are the same for both experiments ($20\,\mu\mathrm{s}$). The amplification gain is 3.4(2) in good agreement with the theoretically expected gain of $\cosh(1.9) = 3.4$.

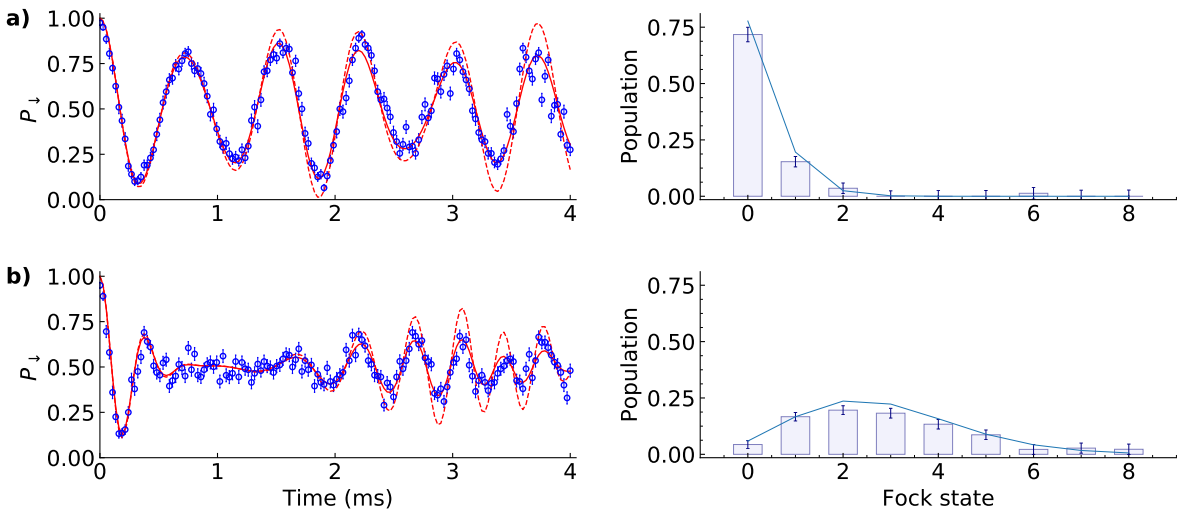

Figure 7.2: Amplification of a coherent displacement. BSB analysis after Hamiltonian amplification with $n = 3$ (see Fig. 7.1), with squeezing parameters of $r = 0$ in a) and $r = 1.9$ in b). In the left column, populations in $|\downarrow\rangle$ are plotted as function of the BSB analysis pulse duration. Blue circles are experimental data. Error bars indicate the standard error of the mean. The solid red curves are fits of Eq. 5.1 to the data assuming a coherent state Fock state distribution (Eq. 2.15) with the displacement amplitude α and the phenomenological decoherence rate γ_0 as the fitting parameters. The dashed red lines are plots of Eq. 5.1 using the fitted value of α, but with the decoherence rate γ_0 set to zero. The panels on the right indicate the Fock state populations obtained from fitting unconstrained Fock state distribution to the data. The solid blue lines indicate the populations of coherent states expected from the fitted values of α.

7.2 Amplification of the Jaynes-Cummings interaction

The Jaynes-Cummings (JC) model gives a fully quantum-mechanical description of the interaction of a two-level system and a single-mode bosonic field [32]. It is of great theoretical and experimental interest in quantum optics, atomic physics, and solid-state physics. An important extension is the Tavis-Cummings model [107] which describes the interaction of a multiple two-level systems with a single bosonic mode. This model describes the generation of entanglement between the two-level systems mediated by the boson field. As discussed in Chapter 2, JC-type interactions are used extensively in trapped-ion experiments. Applications include resolved-sideband cooling, qubit entangling gates, and motional state analysis.

In trapped-ion systems, Jaynes-Cummings dynamics can be implemented by applying the

red sideband interaction Hamiltonian (see chapter 3)

$$\hat{H}_{RSB} = \frac{\hbar\Omega}{2}(\hat{a}^\dagger\hat{\sigma}_- + \hat{a}\hat{\sigma}_+). \tag{7.15}$$

The time evolution operator for this Hamiltonian is given by

$$\hat{U}_{RSB}(\Delta t) = \exp\left[-i\frac{\Omega\Delta t}{2}(\hat{a}\hat{\sigma}_+ + \hat{a}^\dagger\hat{\sigma}_-)\right]. \tag{7.16}$$

Applying squeezing pulses for the Hamiltonian amplification protocol gives

$$\begin{aligned}&\hat{S}^\dagger(\xi)\hat{U}_{RSB}(\Delta t)\hat{S}(\xi)\\ &= \exp\left[-i\frac{\Omega\Delta t}{2}\left((\hat{a}\cosh r - \hat{a}^\dagger e^{i\phi}\sinh r)\hat{\sigma}_+ + (\hat{a}^\dagger\cosh r - \hat{a}e^{-i\phi}\sinh r)\hat{\sigma}_-\right)\right]\end{aligned} \tag{7.17}$$

and

$$\begin{aligned}&\hat{S}^\dagger(-\xi)\hat{U}_{RSB}(\Delta t)\hat{S}(-\xi)\\ &= \exp\left[-i\frac{\Omega\Delta t}{2}\left((\hat{a}\cosh r + \hat{a}^\dagger e^{i\phi}\sinh r)\hat{\sigma}_+ + (\hat{a}^\dagger\cosh r + \hat{a}e^{-i\phi}\sinh r)\hat{\sigma}_-\right)\right].\end{aligned} \tag{7.18}$$

Combined, the overall sequence is

$$\begin{aligned}&\hat{S}^\dagger(\xi)\hat{U}_{BSB}(\Delta t)\hat{S}(\xi)\hat{S}^\dagger(-\xi)\hat{U}_{RSB}(\Delta t)\hat{S}(-\xi)\\ &= \hat{S}^\dagger(\xi)\hat{U}_{RSB}(\Delta t)\hat{S}(2\xi)\hat{U}_{RSB}(\Delta t)\hat{S}^\dagger(\xi)\\ &= \hat{I} + \left(\frac{\Omega\Delta t}{2}2\cosh r(\hat{a}\hat{\sigma}_+ + \hat{a}^\dagger\hat{\sigma}_-)\right) + ...\end{aligned} \tag{7.19}$$

With $\Delta t = \frac{t}{2n}$, in the limit that $n \to \infty$ becomes

$$\begin{aligned}\hat{U}_{HA}(t) \quad &= \lim_{n\to\infty}\left[\hat{I} + \left(\frac{\Omega t}{2n}\cosh r(\hat{a}\hat{\sigma}_- + \hat{a}^\dagger\hat{\sigma}_+)\right) + ...\right]^n\\ &= \exp\left(-i\frac{\cosh r\hat{H}_{RSB}t}{\hbar}\right)\end{aligned} \tag{7.20}$$

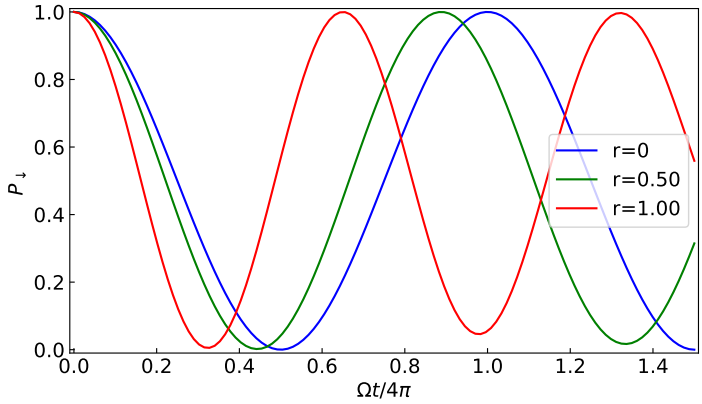

Figure 7.3: Numerical simulations of Hamiltonian amplification of the Jaynes-Cummings interaction (assuming a $\sqrt{n+1}$ scaling of the sideband Rabi frequency) for various values of the squeezing parameter r. Solid curves are numerical simulations of the population in $|\downarrow_s\rangle$ after initially preparing the system in $|\uparrow_s\rangle|0\rangle$. In all cases, $n = 6$.

The Jaynes-Cummings interaction results in Rabi flopping between states $|\uparrow\rangle|0\rangle$ and $|\downarrow\rangle|1\rangle$ with Rabi frequency Ω. Figure 7.3 shows numerical simulations [1] for amplification with $n = 6$. The reduction of contrast of the Rabi oscillations for increasing r is a result of the finite value of n. With Hamiltonian amplification and n sufficiently large, the Rabi frequency increases to $\cosh(r)\Omega$ (Fig. 7.4).

We implement the Jaynes-Cummings interaction using stimulated Raman transitions (see chapter 4). The difference frequency between the Raman lasers is set to $\omega_s - \omega - \Delta_{ACS}$, where $\omega_s/2\pi = 1.326\,\text{GHz}$ is the frequency of the $|\downarrow_s\rangle \equiv |3,3\rangle \leftrightarrow |\uparrow_s\rangle \equiv |2,2\rangle$ "stretch" transition and $\Delta_{ACS}/2\pi \sim 400\,\text{kHz}$ is the AC Stark shift from the laser fields. Hamiltonian amplification is implemented by interleaving the Raman pulses with squeezing pulses (each with $6\,\mu$s duration) as described previously. With the squeezing parameter $r \simeq 1$, we observe an increase in the Rabi frequency (not including the time required for squeezing) for flopping on the $|\uparrow_s\rangle|0\rangle \leftrightarrow |\downarrow_s\rangle|1\rangle$ transition (Fig. 7.5). The increase in Rabi rate by a factor of 1.5 is consistent with the calibrated value of the squeezing parameter $r \simeq 1.0$. With faster squeezing, the increased sideband Rabi

[1] Here I am assuming a $\sqrt{n+1}$ scaling of the sideband Rabi frequency which is only valid in the Lamb-Dicke limit for laser-based sidebands [41].

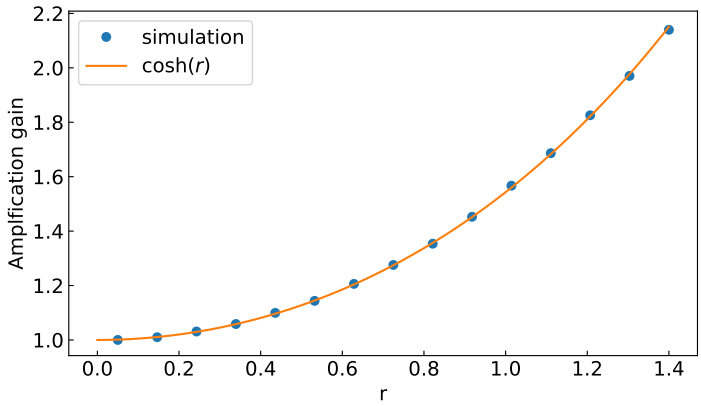

Figure 7.4: Amplification gain for Hamiltonian amplification of the Jaynes-Cummings interaction (assuming a $\sqrt{n+1}$ scaling of the sideband Rabi frequency) as a function of the squeezing parameter r and $n = 6$ sequences. Blue circles give the ratio of the numerically calculated Rabi rate for a given value of r to the Rabi rate with $r = 0$. The solid line is the theoretical gain $\cosh(r)$ in the limit $n \to \infty$.

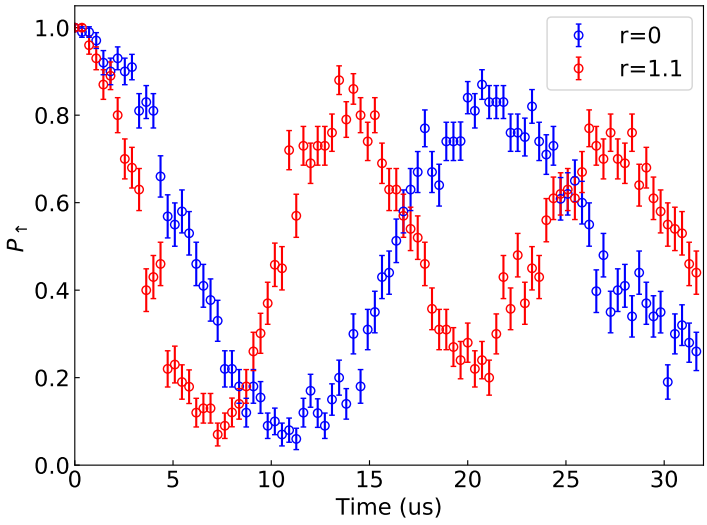

Figure 7.5: Population in $|\uparrow_s\rangle$ as a function of the total RSB pulse duration (not including the duration of the squeezing pulses) in a HA sequence with $n = 6$. The x axis indicates the total duration of the Raman sideband pulses in the amplification sequence.

frequency could enable faster ground-state cooling, and faster generation of entanglement between trapped-ion qubits.

Chapter 8

Parametric amplification of boson-mediated interactions

Strong and precisely controlled interactions between quantum objects are essential for quantum information processing [49, 108], simulation [24], and sensing [12, 13]. However, in many experimental platforms for quantum physics, direct interactions between quantum objects can be weak or difficult to control. Furthermore, increasing the direct coupling of some interactions simultaneously increases coupling to the environment. In many systems strong, controllable interactions are achieved by coupling the individual quantum objects through a shared harmonic oscillator mode. The interactions can then be modeled as being mediated by bosons — excitations of the shared harmonic oscillator. Important physical implementations include photon-mediated interactions between atoms [30, 32], superconducting qubits [109], and color centers in diamond [110], and phonon-mediated interactions between trapped ions [41, 48, 111] and optical and microwave photons [112]. However, the fidelity of these interactions is typically constrained by both the effective interaction strength and the ratio of the interaction strength to characteristic rates of decoherence in the system. Moreover, quantum objects can suffer additional decoherence when coupled to the bosonic degree of freedom (see section 3.5). Recently, numerous theoretical proposals have described how boson-mediated interactions can be amplified by parametric modulation of the shared harmonic interaction in systems such as trapped ions [104], cavity optomechanics [113], superconducting circuit QED systems [109], and atom-cavity systems [114, 115]. Crucially, the parametric drive need not couple directly to the effectively-coupled quantum objects. Parametric amplification can allow for higher fidelities if the dominant source of decoherence affects the quantum objects

and not the boson channel.

In this chapter I describe the theory (based on [104]) and experimental demonstration of parametric amplification of phonon-mediated interactions between trapped ion qubits. The amplified interaction enables a 3.2-fold increase of the effective interaction strength as determined by measuring the speedup of two-qubit entangling gates. Furthermore, I describe experiments demonstrating that parametric modulation can improve the gate fidelity if random qubit frequency fluctuations are the dominant source of decoherence of the system.

8.1 Boson-mediated interactions

The excitations of practically used harmonic oscillators obey the commutation relations and statistics of bosons (typically photons or phonons). Bosonic interactions have been used to demonstrate high-fidelity quantum logic gates [116, 117, 118], spin-squeezed states of atoms and ions [11, 12, 13, 14], and the formation of novel phases of matter [119, 120]. Often, boson-mediated

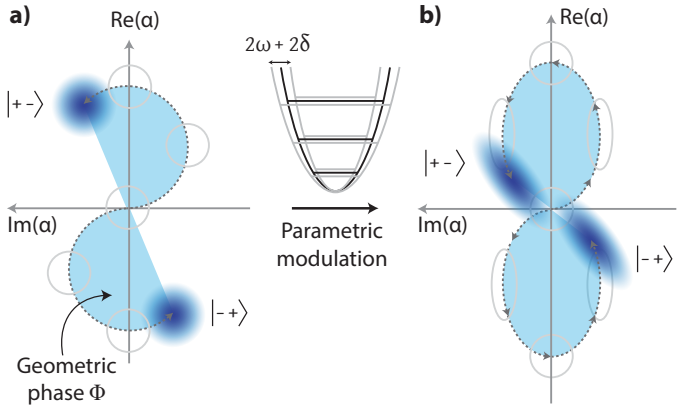

Figure 8.1: Phase space illustration of boson-mediated interactions. I show the case of two qubits ($\hat{S} = \hat{\sigma}_x^1 - \hat{\sigma}_x^2$) coupled by a harmonic oscillator mode with frequency ω. a) Without parametric modulation, the harmonic oscillator quasi-probability distributions (blue fuzzy disks) associated with the $|+-\rangle$ and $|-+\rangle$ spin states follow circular trajectories in a frame rotating at $\omega + \delta$. The enclosed area (shown in light blue) is the geometric phase Φ. b) When the harmonic oscillator is parametrically modulated at a frequency of $2\omega + 2\delta$, in a frame rotating at $\omega + \delta$ the trajectories become elliptical and the motional wave packets (represented by grey and black ellipses) are alternately squeezed and anti-squeezed. More geometric phase is acquired per unit time, increasing the effective interaction strength.

interactions offer longer-range coupling than direct interactions and can be described by a generic Hamiltonian given in the interaction picture rotating at $\omega + \delta$ by

$$\hat{H}_M = \frac{\hbar\Omega}{2}(\hat{S}^\dagger \hat{a} + \hat{S}\hat{a}^\dagger) - \hbar\delta\hat{a}^\dagger\hat{a}. \tag{8.1}$$

Here Ω is the coupling strength between the bosonic degree of freedom, with annihilation and creation operators $\hat{a}$ and $\hat{a}^\dagger$ and frequency ω, and the quantum objects to be coupled described by $\hat{S} \equiv \sum_{i=1} \beta_i \hat{s}_i$, where the $\hat{s}_i$ can be bosonic or fermionic operators on the individual quantum objects coupled by the interaction. The physical significance of δ, a frequency detuning between the harmonic oscillator and the coupling described by the first term in Eq. 8.1, depends on the details of the system. For the case of atoms coupled to a single electromagnetic field mode in a cavity, $\hat{s}_i = \hat{\sigma}_+^i$, where $\hat{\sigma}_+^i$ is the atomic raising operator for the i^{th} atom and δ is the atom-cavity detuning [107]. $\hat{H}_M$ is then the Tavis-Cummings Hamiltonian [107]. In an optomechanical system, the $\hat{s}_i$ are bosonic creation or annihilation operators for photon or phonon fields, depending on the exact implementation. For interactions between trapped-ion qubits, typically $\hat{s}_i = \hat{\sigma}_j^i$—effective fermionic spin 1/2 Pauli operators—and δ is the detuning of an external drive field from the phonon mode used to implement the interaction. The β_j depend on the eigenvector of the phonon mode and $j = x, y$ [48, 49] or $j = z$ [51, 60] depending on the specific implementation. To understand how Eq. 8.1 leads to coupling between the $\hat{s}_i$, consider two trapped-ion qubits coupled through a shared mode of motion such that $\hat{S} = \hat{\sigma}_x^1 - \hat{\sigma}_x^2$. $\hat{H}_M$ is then the Mølmer-Sørensen (MS) interaction described in detail in Chapter 3. Applying $\hat{H}_M$ will result in spin-dependent displacements in phase space of the normal mode that is near resonantly driven by lasers or oscillating magnetic fields. In this case, the two-qubit spin states $|{+}{+}\rangle$ and $|{-}{-}\rangle$, where $|\pm\rangle \equiv \frac{1}{\sqrt{2}}(|\uparrow\rangle \pm |\downarrow\rangle)$, are not displaced and will remain at the origin, whereas $|{+}{-}\rangle$ and $|{-}{+}\rangle$ traverse circular trajectories in phase space (Fig. 8.1 a). The area enclosed by these trajectories gives rise to a state-dependent geometric phase Φ. Applying $\hat{H}_M$ for a duration $\tau = 2\pi/\delta$ returns the harmonic oscillator to its initial state and

disentangles it from $\hat{S}$. This results in the unitary transformation[48]

$$\hat{U}(\tau) = \exp\left(i\frac{\Phi}{4}\hat{S}^2\right), \tag{8.2}$$

which describes an effective spin-spin interaction. When $\delta = \Omega$ and $\tau = \pi/\Omega$, Φ is $\pi/2$, and this interaction allows the generation of maximally entangled states: $\hat{U}(\tau)\,|{\downarrow\downarrow}\rangle \rightarrow \frac{1}{\sqrt{2}}(|{\downarrow\downarrow}\rangle + i\,|{\uparrow\uparrow}\rangle)$.

8.2 Parametric amplification

Boson mediated interactions can be amplified by parametrically modulating the boson mode at a frequency $2\omega + 2\delta$ simultaneously with $\hat{H}_M$. In a frame rotating at $\omega + \delta$, the interaction Hamiltonian becomes

$$\begin{aligned}\hat{H}_M \;\rightarrow\; & \frac{\hbar\Omega}{2}(\hat{S}^\dagger\hat{a} + \hat{S}\hat{a}^\dagger) - \hbar\delta\hat{a}^\dagger\hat{a} \\ & + \frac{\hbar g}{2}(\hat{a}^2 e^{-i\theta} + \hat{a}^{\dagger 2} e^{i\theta}).\end{aligned} \tag{8.3}$$

The third term in Eq. 8.3 describes a parametric modulation of the boson channel with parametric coupling strength g and phase θ between the parametric drive and the coupling interaction in the first term. Insight into the dynamics resulting from Eq. 8.3 can be gained by making the Bogoliubov transformation

$$\hat{b} \equiv \hat{a}\cosh r - \hat{a}^\dagger e^{i\theta}\sinh r, \tag{8.4}$$

$$\hat{b}^\dagger \equiv \hat{a}^\dagger\cosh r - \hat{a}e^{-i\theta}\sinh r. \tag{8.5}$$

where r is to be determined. The inverse transformations are

$$\hat{a} = \hat{b}\cosh r + \hat{b}^\dagger e^{i\theta}\sinh r, \tag{8.6}$$

$$\hat{a}^\dagger = \hat{b}^\dagger\cosh r + \hat{b}e^{-i\theta}\sinh r. \tag{8.7}$$

Applying these transformations yields

$$\hat{a}^\dagger \hat{a} = \cosh(2r)\hat{b}^\dagger \hat{b} + \frac{1}{2}\sinh(2r)[\hat{b}^{\dagger 2} e^{i\theta} + \hat{b}^2 e^{-i\theta}] - \sinh^2(2r), \tag{8.8}$$

$$e^{-i\theta}\hat{a}^2 = \cosh^2(r) e^{-i\theta}\hat{b}^2 + \sinh^2(r) e^{i\theta}\hat{b}^{\dagger 2} + \frac{1}{2}\sinh(2r)[2\hat{b}^\dagger \hat{b} + 1], \tag{8.9}$$

and

$$e^{i\theta}\hat{a}^{\dagger 2} = \cosh^2(r) e^{i\theta}\hat{b}^{\dagger 2} + \sinh^2(r) e^{-i\theta}\hat{b}^2 + \frac{1}{2}\sinh(2r)[2\hat{b}^\dagger \hat{b} + 1]. \tag{8.10}$$

After substituting Eq. 8.8 to 8.10 into Eq. 8.3, to eliminate terms proportional to $\hat{b}^2$ and $\hat{b}^{\dagger 2}$, we require

$$\frac{g}{2}\cosh(2r) = -\frac{\delta}{2}\sinh(2r). \tag{8.11}$$

or

$$\tanh(2r) = -\frac{g}{\delta}. \tag{8.12}$$

Collecting terms proportional to $\hat{b}^\dagger \hat{b}$ gives

$$\delta' \equiv \delta\cosh(2r) + g\sinh(2r) = \sqrt{\delta^2 - g^2} \tag{8.13}$$

Finally, the interaction Hamiltonian becomes

$$\hat{H}_M = \hbar\frac{\Omega}{2}\left(\hat{S}^\dagger[\cosh r\hat{b} + e^{i\theta}\sinh r\hat{b}^\dagger] + \hat{S}[\cosh r\hat{b}^\dagger + e^{-i\theta}\sinh r\hat{b}]\right) - \hbar\delta'\hat{b}^\dagger\hat{b}, \tag{8.14}$$

where constant terms have been dropped. For cases where $\hat{S} = \hat{S}^\dagger$, we have

$$\hat{H}_M = \hbar\frac{\Omega}{2}\hat{S}\left(\hat{b}f(r,\theta) + \hat{b}^\dagger f^*(r,\theta)\right) - \hbar\delta'\hat{b}^\dagger\hat{b}, \tag{8.15}$$

where,

$$\begin{aligned} f(r,\theta) &= \cosh r + e^{i\theta}\sinh r \\ &= \sqrt{\cosh 2r + \cos\theta \sinh 2r}\; e^{i\Phi} \\ &= \left(\frac{\delta - g\cos(\theta)}{\sqrt{\delta^2 - g^2}}\right)^{1/2} e^{i\Phi} \end{aligned} \tag{8.16}$$

with

$$\Phi = \tan^{-1}\left(\frac{\sin\theta \sinh r}{\cosh r + \cos\theta \sinh r}\right). \tag{8.17}$$

Maximum amplification occurs when $\theta = 0$ and the transformed Hamiltonian becomes

$$\hat{H}_M = \hbar\frac{\Omega e^r}{2}\left(\hat{S}^\dagger\hat{b} + \hat{S}\hat{b}^\dagger\right) - \hbar\delta'\hat{b}^\dagger\hat{b}, \tag{8.18}$$

where $e^r = \left(\frac{\delta - g}{\delta + g}\right)^{1/4}$. The transformed Hamiltonian has exactly the same form as Eq. 8.1, but the interaction strength is multiplied by a factor of e^r and δ is replaced by δ'. We can derive the time evolution operator Eq. 8.2 in the same manner as before, but the time to acquire a given geometric phase Φ is multiplied by a factor of e^{-r} and the detuning required δ' is e^r larger. Parametric modulation causes the $|+-\rangle$ and $|-+\rangle$ states to traverse elliptical, rather than circular, trajectories in the phase space of $\hat{a}$ and $\hat{a}^\dagger$ rotating at $\omega + \delta$ (Fig. 8.1 b). For $e^r > 1$, the area enclosed by the trajectories is larger for a given duration of $\hat{H}_M$, due to the increased coupling strength. Physically, the parametric modulation alternately squeezes and anti-squeezes the oscillator quasi-probability distributions as they follow their elliptical trajectories, resulting in amplification of the spin-dependent displacements [87].

In other physical systems, where $\hat{S} \neq \hat{S}^\dagger$, the dynamics resulting from parametric modulation depend on the details of the specific implementation. For the important case of atoms coupled to a cavity, the terms proportional to $\sinh(r)$ in Eq. 8.15 describe excitation of the atom that is accompanied by the addition of a photon to the cavity field. These processes do not conserve energy and will typically be greatly suppressed. After dropping off-resonant terms, the interaction strength is given by $\Omega \to \Omega\cosh(r)$, and the amplification does not depend on θ [115].

8.3 Experimental implementation with trapped-ions

In our experiment, we amplify boson-mediated interactions between two trapped $^{25}Mg^{+}$ hyperfine ion qubits. Details of the experimental apparatus are given in chapter 4. The harmonic oscillator mode is an out-of-phase radial motional mode ("rocking mode") with frequency $\omega \simeq 2\pi \times 5.9\,\mathrm{MHz}$. We use qubit states $|\downarrow\rangle \equiv |F = 3, m_F = 1\rangle$ and $|\uparrow\rangle \equiv |F = 2, m_F = 1\rangle$ (with qubit frequency $\omega_0 \simeq 2\pi \times 1.686\,\mathrm{GHz}$). The MS interaction is implemented by applying oscillating magnetic field gradients at frequencies $\omega_0 \pm (\omega + \delta)$, generated by currents in the microwave electrodes of the trap. Generating the MS interaction in this way allows straightforward phase synchronization with the parametric modulation at $2\omega + 2\delta$ [1] , which is implemented by applying an oscillating potential directly to the rf trapping electrodes.

I will now show explicitly that the combined MS and parametric interactions can be described by Eq. 8.3. As described in chapter 3, after transforming into an interaction picture with respect to

$$\hat{H}_0 = \hbar\omega\hat{a}^\dagger\hat{a} + \hbar\frac{\omega_0}{2}(\hat{\sigma}_z^1 + \hat{\sigma}_z^2), \tag{8.19}$$

the MS Hamiltonian is given by

$$\hat{H}_{MS} = \hbar\frac{\Omega}{2}(\hat{a}e^{i\delta t} + \hat{a}^\dagger e^{-i\delta t})(\hat{\sigma}_x^1 - \hat{\sigma}_x^2), \tag{8.20}$$

and the parametric drive Hamiltonian by

$$\hat{H}_p = \frac{\hbar g}{2}(\hat{a}^2 e^{2i\delta t - i\theta} + \hat{a}^{\dagger 2} e^{-2i\delta t + i\theta}). \tag{8.21}$$

Applying the MS fields and parametric drive simultaneously yields:

[1] A nifty trick for checking that the phase between the MS fields and the parametric drive is stable is to compare the parametric drive voltage signal with a signal containing the difference frequency of the MS fields, which is also at $2\omega + 2\delta$, on an oscilloscope. In our experiment, the difference frequency signal is obtained by from a diode power detector (which acts as a multiplier) connected to the monitor port shown in Fig. 4.17.

$$\begin{aligned}\hat{H}_I &= \hat{H}_{MS} + \hat{H}_P \\ &= \hbar\frac{\Omega}{2}(\hat{a}e^{i\delta t} + \hat{a}^\dagger e^{-i\delta t})(\hat{\sigma}_x^1 - \hat{\sigma}_x^2) + \frac{\hbar g}{2}(\hat{a}^2 e^{2i\delta t - i\theta} + \hat{a}^{\dagger 2} e^{-2i\delta t + i\theta}).\end{aligned} \tag{8.22}$$

If we transform into another interaction picture with respect to $\hat{H}_1 = \hbar\delta\hat{a}^\dagger\hat{a}$, the time dependence can be eliminated

$$e^{-i\frac{\hat{H}_1 t}{\hbar}}\hat{H}_I e^{i\frac{\hat{H}_1 I t}{\hbar}} = \hbar\frac{\Omega}{2}(\hat{a} + \hat{a}^\dagger)(\hat{\sigma}_x^1 - \hat{\sigma}_x^2) + \frac{\hbar g}{2}(\hat{a}^2 e^{-i\theta} + \hat{a}^{\dagger 2} e^{i\theta}) - \hbar\delta\hat{a}^\dagger\hat{a}, \tag{8.23}$$

which is equivalent to Eq. 8.3 with $\hat{S} = \hat{\sigma}_x^1 - \hat{\sigma}_x^2$.

8.3.1 Calculation of the gate time and detuning for parametrically amplified gates without decoherence

The preparation of the Bell state $|\psi_B\rangle = \frac{1}{\sqrt{2}}(|\downarrow\downarrow\rangle + i\,|\uparrow\uparrow\rangle)$ from the initial state $|\downarrow\downarrow\rangle$ requires the closure of an integer number of phase space loops and the accumulation of a geometric phase of $\Phi = \pi/2$. The closure of a single loop occurs when τ is given by:

$$\tau = \frac{2\pi}{\delta'} = \frac{2\pi}{\sqrt{\delta^2 - g^2}} \tag{8.24}$$

The geometric phase acquired in that loop, Φ, must be equal to $\pi/2$:

$$\Phi = 2\pi\left(\frac{\Omega|f(g,\delta,\theta)|}{\delta'}\right)^2 = 2\pi\left(\frac{\Omega|f(g,\delta,\theta)|}{\sqrt{\delta^2 - g^2}}\right)^2 = \frac{\pi}{2} \tag{8.25}$$

Given g, θ, and Ω_0, we can determine the correct values of τ and δ by numerically solving Eqs. 8.24 and 8.25 simultaneously. All values of τ, δ, and δ' calculated from analytical theory that are presented below are calculated in this manner.

8.3.2 Calibrating sideband Rabi rates

To quantify the increased interaction strength resulting from parametric modulation, it is necessary to characterize the bare MS interaction strength Ω. Preliminary estimates of the MS

interaction strength are obtained from sideband Rabi flopping with a single ion prepared close to the motional ground state. These measurements also allow us to adjust the microwave power delivered to the trap to balance the Rabi rate of each sideband to within 5%. More accurate calibration of the sideband Rabi rate is performed by sideband analysis with two ions using the gate mode. The ions are initially prepared close to the $|0\rangle$ motional state using resolved sideband cooling. A series of microwave pulses is then used to prepare the internal state of the ions in $|\uparrow\rangle|\uparrow\rangle$. A red sideband analysis pulse is then applied at $\omega_0 + \Delta_{ACZ} + \omega$, where Δ_{ACZ} is the AC Zeeman shift from the sideband pulse, for duration t_{RSB}, followed by detection. The process is repeated several hundred times for each t_{RSB} to gather statistics. By fitting a numerical model to the data, we can extract the Rabi frequency, the differential AC Zeeman shift of each ion, and the residual initial thermal occupation $\bar{n}$. Example data are shown in Fig. 8.2. The fitting parameters are listed in table 8.1.

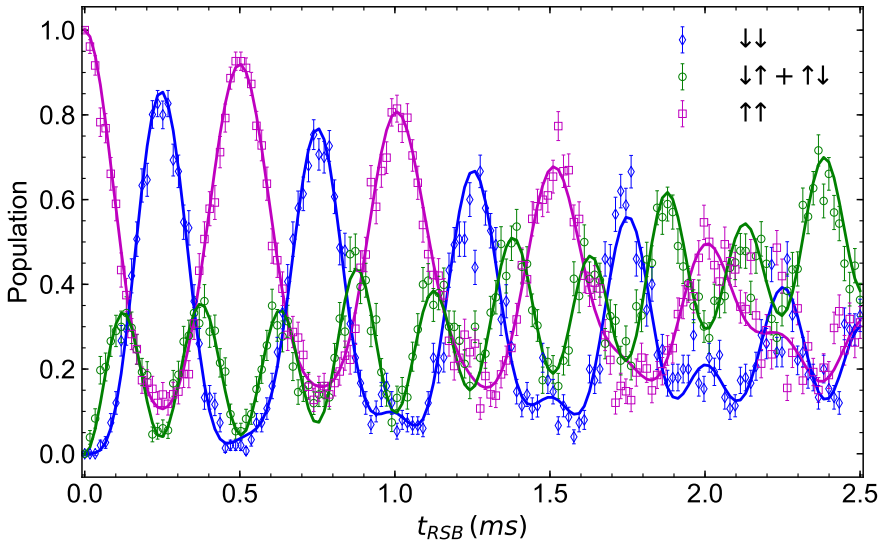

Figure 8.2: Two-ion populations as a function of the red sideband analysis pulse duration. The ions are initially prepared in $|\uparrow\rangle|\uparrow\rangle$ spin state and the radial rocking mode is cooled close to the motional ground state using resolved sideband cooling. The solid curves are a least squares fit of a numerical model to the data.

More accurate measurements of the AC Zeeman shift Δ_{ACZ} that arises when both sidebands

Table 8.1: Fit parameters for sideband Rabi flopping shown in Fig. 8.2

Parameter	Symbol	Value
Sideband Rabi rate for ion 1	$\Omega_1/2\pi$ (kHz)	1.987(4)
Sideband Rabi rate for ion 2	$\Omega_2/2\pi$ (kHz)	2.107(4)
AC Zeeman shift for ion 1	$\Delta_{AC1}/2\pi$ (kHz)	0.15(4)
AC Zeeman shift for ion 2	$\Delta_{AC2}/2\pi$ (kHz)	0.15(4)
Initial average thermal occupation	$\bar{n}$	0.057(8)

are applied simultaneously are obtained using a Ramsey experiment (on the clock qubit) with the MS fields appropriately detuned from the motional resonance.

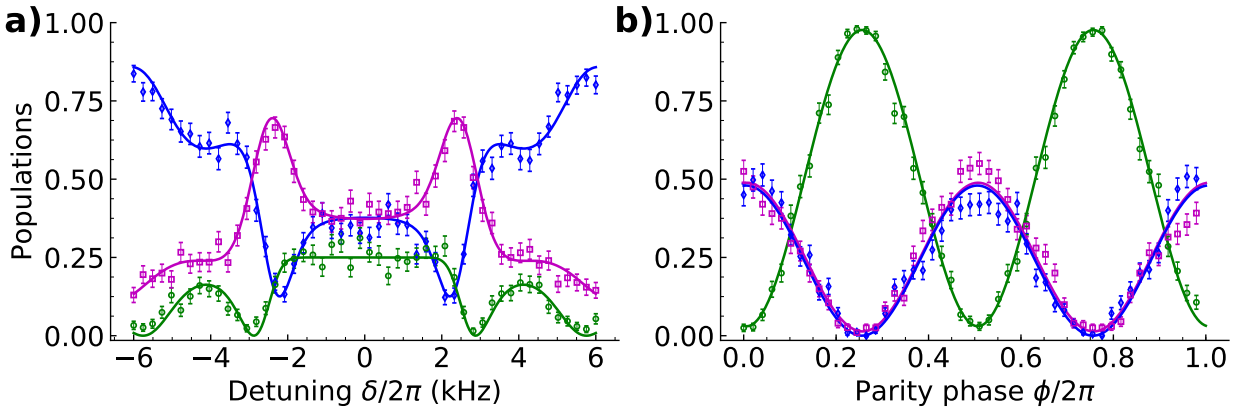

Figure 8.3: Mølmer-Sørensen interaction. a) Two-ion qubit populations of $|\downarrow\downarrow\rangle$ (blue diamonds), $|\uparrow\uparrow\rangle$ (magenta squares), and anti-aligned spin states $|\downarrow\uparrow\rangle$ and $|\uparrow\downarrow\rangle$ combined (green circles) as a function of the gate detuning δ. The gate time is $t_g = 350\,\mu$s. Solid curves are from an analytical model (Eqs. 3.59 and 3.60) fitted to the data. The fitting parameters are the gate coupling strength $\Omega/2\pi = 2.07(3)\,$kHz and the residual thermal occupation $\bar{n} = 0.046(3)$. b) Two-qubit populations as a function of the parity phase ϕ. For this data, $\delta/2\pi = -2.9\,$kHz. Solid curves are sinusoidal fits to the data. Error bars indicate the standard error of the mean.

8.3.3 Mølmer-Sørensen (MS) gate

For gate experiments, the ions are initialized near the motional and electronic ground state $|\downarrow\downarrow\rangle\,|0\rangle$ with optical pumping, resolved-sideband laser cooling [121], and microwave pulses. We then apply the gate pulses for a duration t_g and detuning δ. The qubits are read out by detecting state-dependent ion fluorescence (see section 4.4). A detuning scan is shown in Fig. 8.3. The data show good agreement with the theoretically expected behavior (Eqs. 3.59, 3.60), with the coupling strength Ω and the residual thermal occupation as free parameters. The gate ideally creates the Bell state $|\Phi\rangle_{Bell} = \frac{1}{\sqrt{2}}(|\downarrow\downarrow\rangle - i\,|\uparrow\uparrow\rangle)$, and the fidelity of the state that is generated experimentally is characterized by measuring the state fidelity $\langle\Phi_{Bell}|\,\hat{\rho}_{exp}\,|\Phi_{Bell}\rangle$, where $\hat{\rho}_{exp}$ is the experimentally generated density matrix. The diagonal elements of the density matrix $P_{\downarrow\downarrow}$ and $P_{\uparrow\uparrow}$ are determined from independent measurements of the populations at a given interaction time and detuning. The off-diagonal elements of $\hat{\rho}_{exp}$, can be determined by scanning the phase of an analysis carrier $\pi/2$ pulse before detection (Fig 8.3 b)). The parity amplitude A is determined by fitting the function $A\sin(2\phi+\phi_0)$ to the parity $P_{\downarrow\downarrow} + P_{\uparrow\uparrow} - P_{\uparrow\downarrow} - P_{\downarrow\uparrow}$. The Bell-state fidelity is then given

by $\mathcal{F} = (P_{\downarrow\downarrow} + P_{\uparrow\uparrow} + A)/2$ [49]. Using this method, the Bell-state fidelity for the data shown in 8.3) is 0.97(1). While this method is easy to implement, and serves to illustrate the basic concept, it does not correct for state preparation and measurement (SPAM) errors. A more rigorous method (which we call the "Keith" method) that uses maximum likelihood to calculate the state fidelity in the presence of SPAM errors, is described in [122]. Besides parity and population data, the method requires fluorescence count histograms measured after preparing the ions in different initial spin states (see Fig.8.4) to evaluate the SPAM error. For the gate data shown in Fig. 8.3, the Keith method gives a mean fidelity of 0.974 with a 95% confidence interval between 0.968 and 0.976 . All fidelity measurements in the remainder of this chapter were obtained using the Keith method.

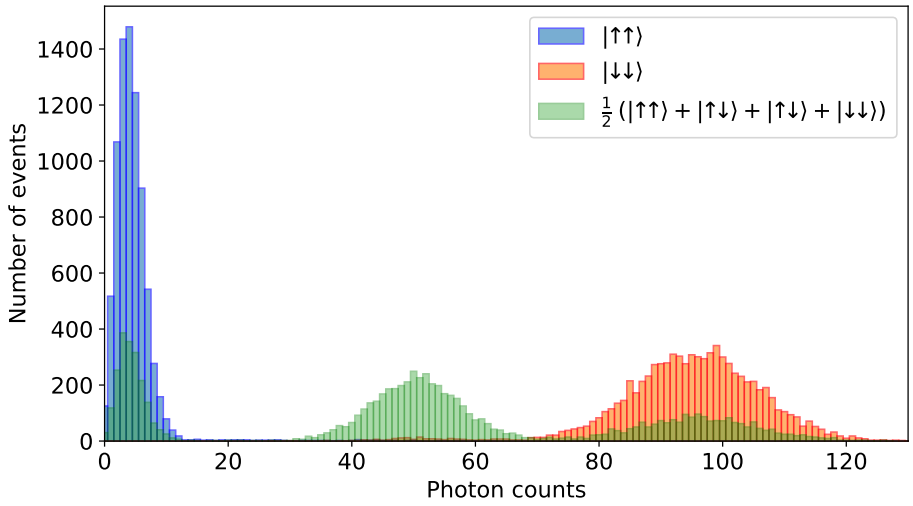

Figure 8.4: Histograms used to evaluate state preparation and measurement error contributions to the state fidelity. Bars indicate fluoresence counts measured after preparing the the two-ion qubit state as $|\uparrow\uparrow\rangle$ (blue), $|\downarrow\downarrow\rangle$ (orange), and after applying a global $\pi/2$ pulse on the $|\downarrow\downarrow\rangle$ state (green).

8.3.4 Calibrating the parametric drive

To investigate the relationship between the increased interaction strength and the parametric coupling strength g, we need to be able to accurately measure g. The procedure is the same as described above for measuring the sideband Rabi rates, but in this case, the motional state is prepared as a squeezed state by applying the parametric drive on resonance (at 2ω) for a duration

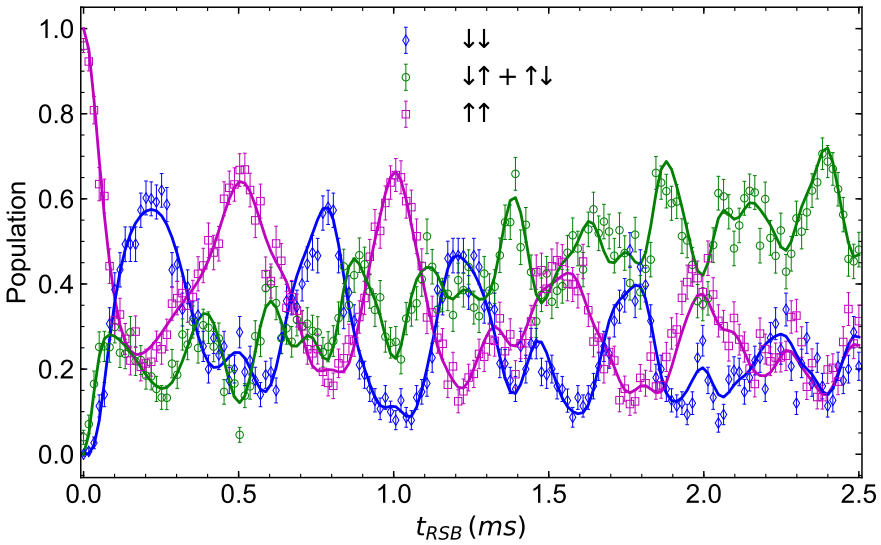

[!h]

Figure 8.5: Two-ion populations as a function of the red sideband analysis pulse duration. The ions are initially prepared in $|\uparrow\rangle|\uparrow\rangle$ spin state and the radial rocking mode is prepared in a squeezed state using parametric modulation. A least squares fit of a numerical model to the data gives a squeezing parameter of $r = 1.19(2)$.

t_s before the analysis pulse. The squeezing parameter r can then be extracted by fitting a numerical model with only r as a free parameter, as all other relevant parameters of the model can be measured by performing the same experiment without squeezing as described in section 8.3.2. The parametric coupling strength is then $r = gt_s$.

The value of g depends on the frequency of the parametric drive ω_P. This is expected, as a resonant circuit is used to couple the parametric drive to the trap RF source circuit (see Fig. 4.18). To account for the frequency dependence, we measured g at various values of the rocking mode frequency ω. Since $\omega_P = 2\omega$ for the calibration experiment, we find that g depends on the mode frequency (Fig. 8.6). The mode frequency was changed by adjusting the DC shim potentials of the surface trap. At each frequency, we perform sideband flopping analysis to measure Rabi rates, AC Zeeman shifts, $\bar{n}$, and g as described above. The frequency dependence of g is well-described by a quadratic polynomial. The polynomial coefficients are obtained using a least-squares fit. This calibration function is used in experiments described below to assign g based on measurements of the rocking mode frequency. This is particularly useful for measuring changes in g resulting from

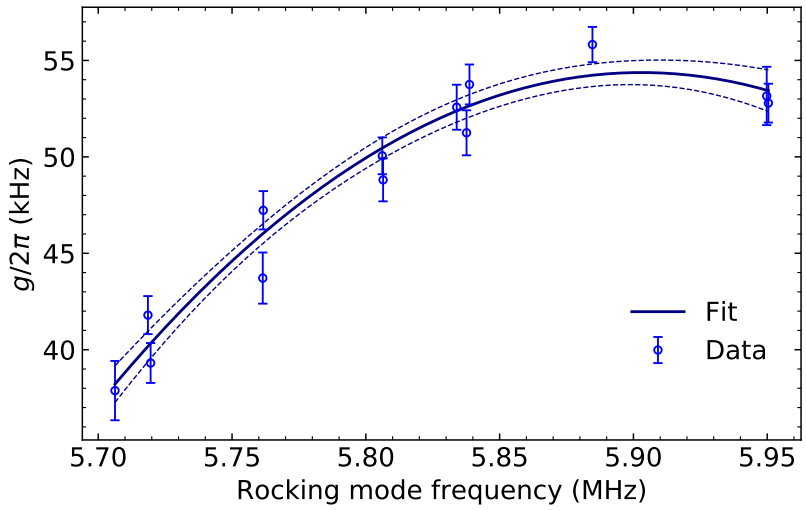

Figure 8.6: Parametric drive strength g as a function of the rocking mode frequency. The solid line is a quadratic fit to the data giving $\bar{\Delta}_{AC}/2\pi = 4.588(7)$ and and $\sigma_{AC}/2\pi$=0.322(5) kHz. Error bars indicate 68% confidence intervals. Dashed lines indicates 68% functional prediction bands [123].

drifts of ω, since we measure ω before every gate experiment.

8.4 Parametrically amplified entanglement generation

To determine the enhancement in the interaction strength due to parametric modulation, we find the maximum Bell state fidelity as a function of the interaction time t_I and the detuning δ, for various values of g. This is ideally equivalent to fixing the area enclosed by the phase-space trajectories of the oscillator wavepackets (Fig. 8.1) such that a maximally-entangled Bell state is generated at the end of the interaction. Fig. 8.7 shows example data of the two-qubit populations and parity analysis for $t_I = 90\mu$s, and $g/2\pi = 50(1)$ kHz. The fidelity is measured over a grid of typically more than 25 t_I and δ pairs (Fig. 8.8). The effective detuning $\delta' = \sqrt{\delta^2 - g^2}$ is calculated from δ and the calibrated value of g for each experiment. The time and effective detuning at which the maximum fidelity occurs is then determined by fitting a low-order two-dimensional polynomial to the grid of (t_I, δ') pairs[2] (Fig. 8.8), to find the duration t_{max} at which maximum fidelity occurs.

The maximum measured fidelity, as a function of δ for each t_I, for various values of g is

[2] We find that using δ' instead of δ gives better conditioned fits. This is because the transformation $\delta' = \sqrt{\delta^2 - g^2}$ suppresses common shifts in g and δ resulting from drifts in the rocking mode frequency

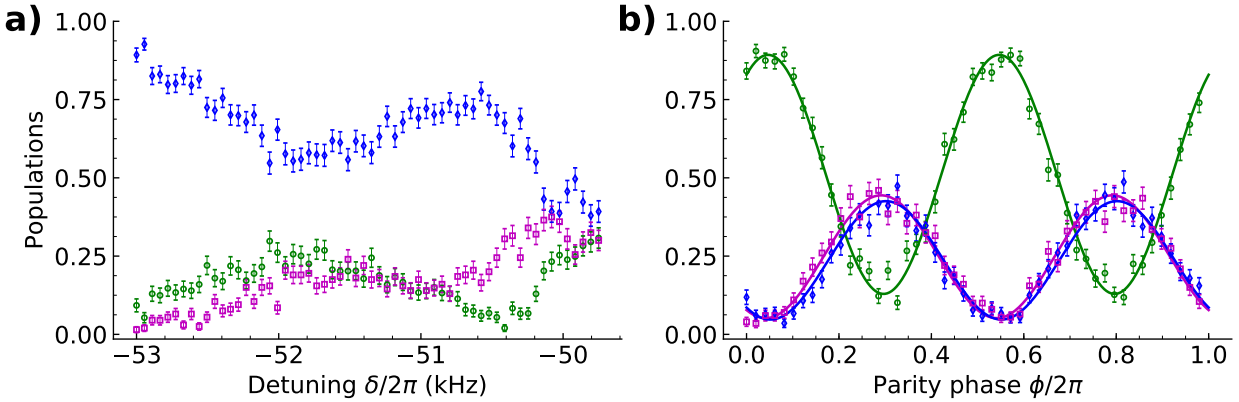

Figure 8.7: Parametrically amplified Mølmer-Sørensen interaction. a) Two-ion qubit populations of $|\downarrow\downarrow\rangle$ (blue diamonds), $|\uparrow\uparrow\rangle$ (magenta squares), and anti-aligned spin states (green circles) as a function of the gate detuning δ for $g/2\pi = 50(1)\,\mathrm{kHz}$. The interaction time is $t = 90\,\mu\mathrm{s}$. b) Two-qubit populations as a function of the parity phase ϕ. The detuning is $\delta/2\pi = -50.3\,\mathrm{kHz}$ and the interaction time is $t_I = 90\,\mu\mathrm{s}$. Solid curves are sinusoidal fits to the data. Data points represent the mean of 200 experimental trials. Error bars indicate the standard deviation of the mean.

shown in Fig. 8.9. As g is increased, the interaction time at which the maximum fidelity occurs (t_{Imax}) is reduced (Fig. 8.10). However, the measured maximum fidelities tend to occur at shorter durations than would be theoretically predicted in the absence of imperfections. The reduction results from amplification of motional decoherence by the parametric modulation and we find good agreement with numerical simulations incorporating motional dephasing[3] (see section 3.5). The amplified motional decoherence also causes the maximum fidelity to diminish as g is increased. For a parametric coupling strength of $g/2\pi = 50(1)\,\mathrm{kHz}$, we measure a maximum fidelity of 0.860(8)% (Fig. 8.7 b) at an interaction time of $90\,\mu\mathrm{s}$ a factor of 3.8(2) lower than the un-amplified gate duration $t_0 = 342(3)\mu\mathrm{s}$. From the numerical simulation incorporating motional dephasing, this would correspond to an increase in the interaction strength by a factor of $e^r = 3.2$.

[3] Motional heating does not play a significant role due to the low heating rate of the rocking mode, which was measured to be $\sim 1\,\mathrm{q/s}$

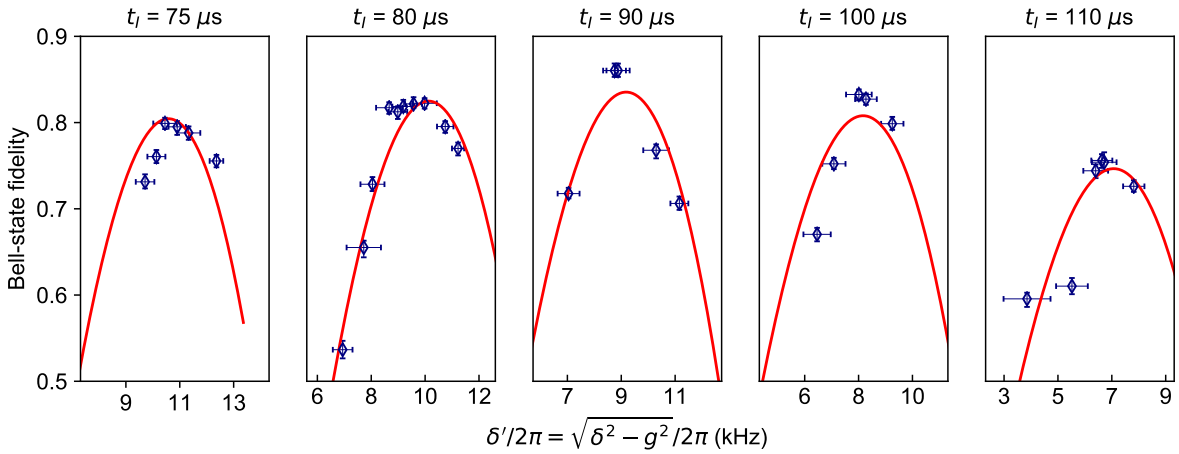

Figure 8.8: Fidelity as a function of $\delta'/2\pi$ for various values of t_I for a calibrated value of the parametric coupling strength of $g/2\pi = 49.7\,\text{kHz}$. Data points are fidelities obtained using the Keith code 122. Vertical error bars indicate 68 % confidence intervals for the fidelity. Horizontal error bars indicate 68 % confidence intervals for $\delta'/2\pi$ calculated from error propagation of the measured uncertainties in δ and g within a given experiment. Red curves are slices of the 2D polynomial fitting function at the corresponding interaction times.The maximum of the fitted quadratic occurs at a duration of $88(1)\,\mu\text{s}$.

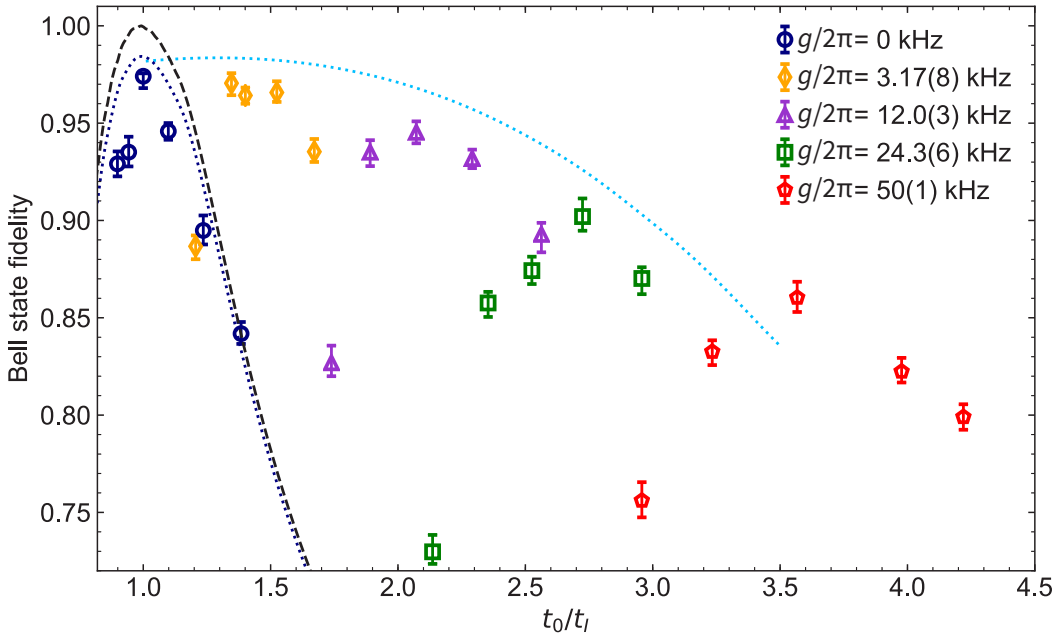

Figure 8.9: Bell state fidelity as a function of t_0/t_I, the ratio of the gate time without parametric modulation t_0 to the interaction time t_I at which the fidelity is measured, for various values of the parametric coupling strength g. Data points indicate the maximum measured fidelity for that t_I. Error bars indicate 95 % confidence intervals. The dashed black curve is a numerical simulation of the maximum achievable fidelity for a given t_I without parametric modulation and without decoherence. The light blue and navy dotted curves are simulations, including motional decoherence, of the maximum achievable fidelity at a given t_I with and without parametric modulation respectively.

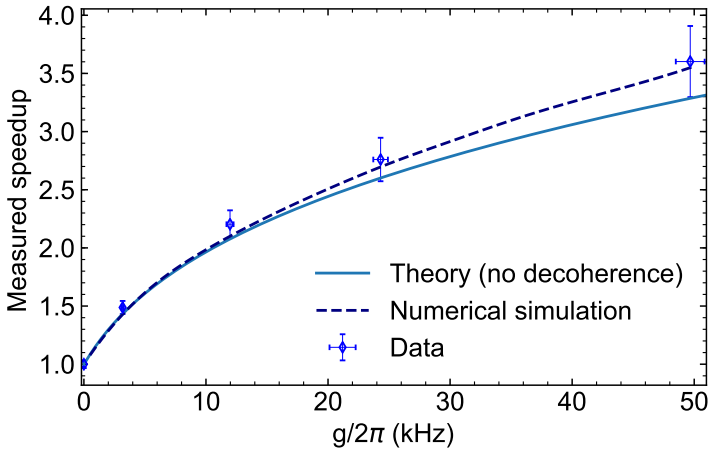

Figure 8.10: Speedup as a function of the parametric drive amplitude g. The speedup is the ratio of the initial gate duration t_0 to t_{Imax} the interaction duration at which we find the maximum fidelity. Error bars correspond to 95 % confidence intervals. The solid line is the theoretically predicted speedup in the absence of decoherence. The dashed line is a numerical simulation including motional decoherence.

8.5 Speed up and enhanced fidelity in the presence of qubit decoherence

As parametric driving only couples to the boson mode and does not directly affect the qubits, effective spin-spin interactions can be enhanced without increasing qubit decoherence. Furthermore, in the presence of noise that gives rise to qubit decoherence, parametric amplification can enable both a reduction in the interaction time and an improvement in the fidelity. To demonstrate this effect, we deliberately introduce fluctuating qubit frequency shifts to decohere our qubits. Since the $|F = 3, m_F = 1\rangle \leftrightarrow |F = 2, m_F = 1\rangle$ "clock" transition of $^{25}Mg^{+}$ is first-order magnetic field insensitive at our operating magnetic field, ambient magnetic field fluctuations do little to decohere our qubits. In the absence of applied noise, we measure no significant decay of contrast in a single-ion qubit Ramsey experiment up to a 200 ms Ramsey delay time. To introduce qubit decoherence we apply a current to one of the trap electrodes that oscillates near the quibt frequency ω_0. The current is sufficiently detuned that the probability of a qubit transition is negligible. However, there is an AC Zeeman shift $\sim \frac{\Omega_n^2}{\delta_n}(\hat{\sigma}_z^1 + \hat{\sigma}_z^2)$, where Ω_n is the Rabi rate that would be measured if the frequency of the current were tuned onto resonance and δ_n is the detuning. We change the amplitude of the current every ms so as to produce a Gaussian distribution of AC zeeman shifts. This is on the order of the duration of one of our gate experiments including cooling, state preparation and detection. To calibrate the noise we first apply the oscillating current with an applied amplitude (I_n) to produce a static AC Zeeman shift which can be measured using a single-ion Ramsey experiment. By repeating the experiment for several values of the current amplitude, we measure the AC zeeman shift as a function of the applied amplitude. Since $\Omega_n \propto I_n$, to get a Gaussian distribution of AC Zeeman shifts we set the current $I_n \propto \sqrt{\Delta_{ACZ}}$, where Δ_{ACZ} is randomly chosen from a Gaussian distribution with mean $\bar{\Delta}_{AC}$ and standard deviation σ_{AC}. We also perform two-ion Ramsey experiments with the noise on for different settings of σ_{AC} (example data for one setting of σ_{AC} is shown in Fig. 8.11). The decay in contrast is well described by a $e^{-\frac{t^2}{2\tau}}$ decay, where τ is the decay time (Fig. 8.5). For the gate experiments described below, the noise settings were $\bar{\Delta}_{AC} = 4.59(8)$ kHz, and $\sigma_{AC} = 0.47(2)$ kHz.

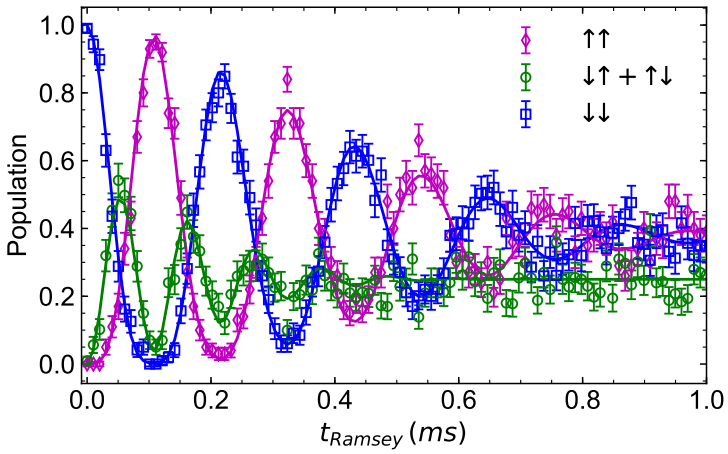

Figure 8.11: Ramsey experiment in the presence of induced qubit decoherence. Two-ion populations are plotted as a function of the Ramsey delay time t_{Ramsey}. Solid curves are from a numerical fit to the data giving $\bar{\Delta}_{AC}/2\pi = 4.59(8)$ and and $\sigma_{AC}/2\pi$=0.421(7) kHz. Error bars indicate the standard deviation of the mean.

In the presence of this decoherence, the maximum fidelity we measure without parametric modulation is 78.7(8)% at an interaction time of 310 μs, whereas with parametric modulation we measure a fidelity of 91.2(5)% at an interaction time of 160 μs with a parametric coupling strength of $g/2\pi = 12.1(3)$ kHz (Fig. 8.5). The fidelity decreases with further increases in g as parametrically amplified motional dephasing becomes the dominant error mechanism.

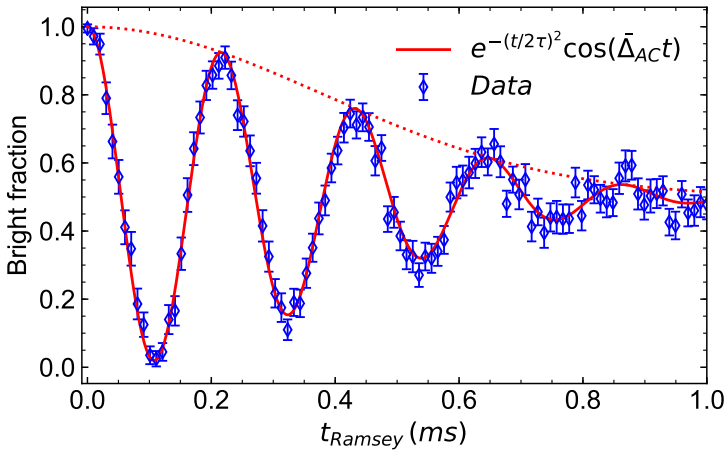

Figure 8.12: Ramsey experiment in the presence of induced qubit frequency decoherence. The bright fraction is plotted as a function of the Ramsey delay time. The solid red curve is a fit to the function $e^{-\frac{t^2}{2\tau}}\cos(\bar{\Delta}_{AC}t)$giving $\bar{\Delta}_{AC}/2\pi = 4.61(1)\,\text{kHz}$ and $\tau = 0.379(8)$ ms. The dashed line indicates the $e^{-\frac{t^2}{2\tau}}$ decay envelope.

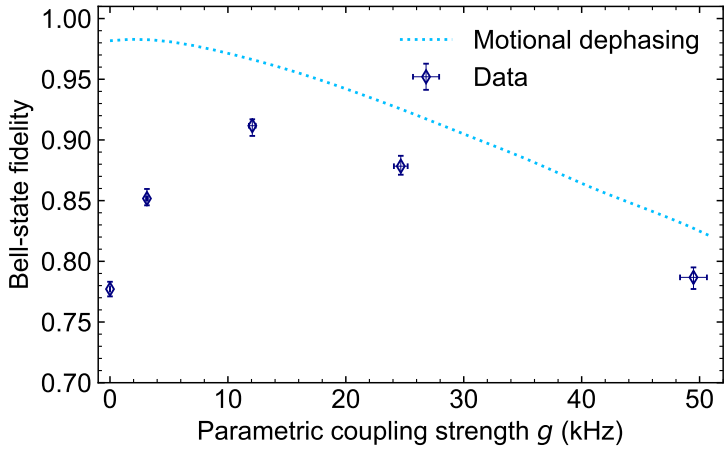

Figure 8.13: Bell-state fidelity as a function of the parametric coupling strength g in the presence of qubit dephasing with $\sigma_{AC} = 0.47(2)\,\text{kHz}$. The light-blue dotted line is a numerical simulation (including motional decoherence, but not qubit decoherence mechanisms) of the maximum possible single-loop fidelity (for any time or detuning) as a function of g. Error bars indicate 95% confidence intervals.

8.6 Phase dependence

For the previous results, the phase of the parametric drive relative to the MS phase was nominally set to give maximum amplification ($\theta = 0$). To further verify the physics of the parametric

amplification process, we vary the phase of the parametric drive θ relative to the phase of the MS fields for a fixed parametric coupling strength of $g/2\pi = 12.3(3)$ kHz (Fig. 8.14). At each phase setting we locate the maximum Bell-state fidelity (as before) for each interaction duration t_I as a function of the detuning δ. The parametric amplification process is first-order insensitive to changes in the parametric drive phase [104] and we measure no significant reduction in the interaction time at which maximum fidelity occurs or the maximum fidelity over the range $\theta/2\pi = 0$ to 0.14. Changing θ further from its optimum value results in an increase in t_{Imax} that is well described by theory. The required increased interaction time is accompanied by a reduction in F_{max} from 0.95 to 0.76 as $\theta/2\pi$ changes from 0 to 0.39 as parametric amplification of motional decoherence (which is independent of θ) affects the process more strongly over a longer duration. Measurements of the fidelity as a function of θ for fixed g, t_I, and δ also show the first-order insensitivity to θ (Fig. 8.15). However, numerical simulations show that the presence of motional decoherence tends to reduce the phase insensitivity to some extent.

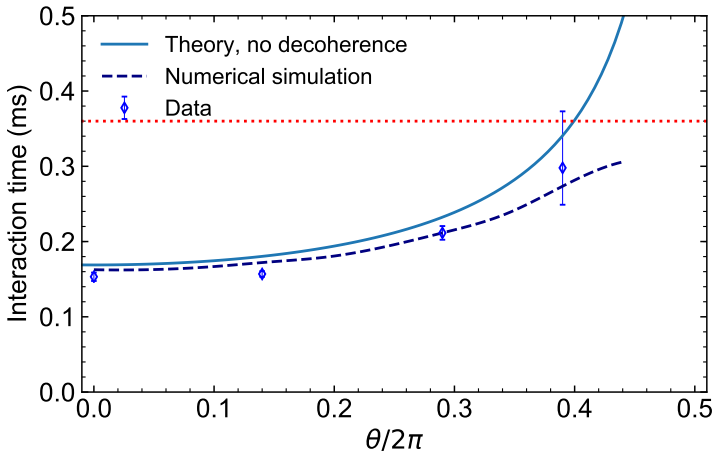

Figure 8.14: Interaction duration of maximum fidelity t_{Imax} as a function of the parametric drive phase θ for $g/2\pi = 12.75(4)$ kHz. The dotted red line indicates the gate duration without parametric modulation ($g = 0$). The solid blue line is analytical theory with no decoherence. The dashed blue line is a numerical simulation including motional dephasing. Error bars indicate 68% confidence intervals

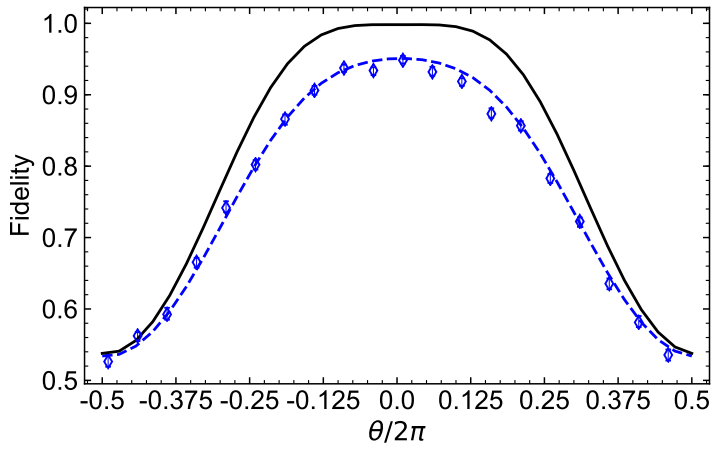

Figure 8.15: Fidelity as as function of the parametric drive phase θ for fixed parametric coupling strength g, interaction time t_I and detuning δ. The solid black line is a numerical simulation with no decoherence and with t_I and δ set to give maximum fidelity at $\theta = 0$ for the calibrated value of g. The dashed blue line is a numerical simulation incorporating motional decoherence. Error bars indicate 68% confidence intervals.

Chapter 9

Conclusion and outlook

Perhaps the most ubiquitous and elementary quantum-mechanical models are the two-level system (also known as a spin 1/2 or a qubit) and the harmonic oscillator. Improved control of over real systems that are adequately described by these models has facilitated advances in quantum information processing and metrology and led to deeper understanding of quantum mechanics. Trapped atomic ions, where select pairs of internal electronic states comprise qubits, and the motion of the ions constitutes a harmonic oscillator, form an almost ideal platform for studying these models and the physics emerging if several such elementary systems are coupled together. In this thesis I have explored new applications of parametric driving for controlling trapped-ion oscillators and subsequently altering the coupling between qubit degrees of freedom mediated by these oscillators. Experimentally, parametric modulation was implemented by periodic distortion of the ion trap potential at MHz frequencies. This laser-free method enables the reversible generation of large squeezed states of trapped-ion motion which can be useful for quantum-enhanced metrology. Furthermore, I have presented experiments demonstrating that reversible squeezing also permits nearly noise-free, phase-sensitive amplification of harmonic oscillator displacements, which has allowed us to resolve displacements well below the zero-point fluctuations of the oscillator. Extensions of this protocol can be used for amplification of a broad class of interactions involving both harmonic oscillators and spins. In particular, I have presented experiments describing parametric amplification of phonon-mediated interactions between trapped-ion qubits, as demonstrated by a reduction in the time required to implement two-ion entangling gates. These new tools could benefit quantum

metrology, quantum simulation, and quantum information processing in systems where harmonic oscillators are essential components. There are many possible directions in which this work can be extended in the future. Below I give a perspective of some interesting possibilities: Two-mode operations, continuous variable quantum information processing, and improving the performance of trapped-ion systems that are limited by spontaneous emission errors.

9.1 Two-mode operations

For the squeezing and amplification experiments described in this thesis, the parametric modulation frequency was set to (or relatively close to) twice the frequency of a normal mode of motion of a trapped ion crystal (see section 2.6). This is known as degenerate parametric modulation and implements single-mode squeezing. Coupling of the parametric drive to other normal modes was neglected due to the large detuning ($\sim 5\,\mathrm{MHz}$) of the parametric drive from the degenerate parametric resonance of the nearest spectator modes. With a parametric coupling strength of $g/2\pi \sim 50\,\mathrm{kHz}$, the effect of the parametric drive on the nearest mode is suppressed by a factor $\sim 10^{-2}$. However, parametric driving can also be used to couple different modes together. If we considered coupling two modes described by annihilation operators $\hat{a}$ and $\hat{b}$ with frequencies ω_a and ω_b respectively, by appropriately setting the parametric drive frequency, two important interactions can be implemented: two mode squeezing and beam splitting.

9.1.1 Beam splitting

If we set the parametric drive frequency to $\omega_a - \omega_b$, the resulting interaction in a frame rotating at $\omega_a - \omega_b$, after making a rotating wave approximation,[1] can be written as [35]

$$\hat{H} = \frac{\hbar g}{2}(\hat{a}\hat{b}^\dagger e^{i\theta} - \hat{a}^\dagger \hat{b} e^{-i\theta}), \tag{9.1}$$

[1] For both the beamsplitter and two-mode squeezing interactions, I assume that there is a component of the potential curvature tensor that allows coupling of the two modes. I also assume that the mode frequencies ω_a and ω_b, are chosen so that the rotating wave approximation is valid

where θ is the relative phase of the parametric drive. Eq. 9.1 is formally equivalent to the Hamiltonian for an optical beam splitter [30]. This interaction enables exchange of quanta between the modes. If mode a is prepared in the ground state and mode b is prepared in a number state with n quanta, so that the initial state is $|0\rangle_a |n\rangle_b$, after an interaction duration $t = 2\pi/g$, the final state will be $|n\rangle_a |0\rangle_b$. The beamsplitter interaction is required for most continuous-variable quantum information processing protocols as discussed in the next section and has been implemented using laser-free parametric modulation in various trapped-ion systems [124, 125, 126]

9.1.2 Two-mode squeezing

If we set the parametric drive frequency to $\omega_a + \omega_b$ (non-degenerate parametric modulation), after making a rotating wave approximation, in a rotating frame at $\omega_a + \omega_b$ we can realize an interaction given by

$$\hat{H} = \frac{\hbar g}{2}(\hat{a}\hat{b}e^{i\theta} + \hat{a}^\dagger\hat{b}^\dagger e^{-i\theta}), \tag{9.2}$$

If this Hamiltonian is applied for a duration t to an oscillator prepared in the ground state of both modes, $|0\rangle_a |0\rangle_b$ the resulting state is know as a two-mode squeezed vacuum (TMSV) state:

$$|\chi\rangle \equiv \hat{S}_2(\chi) |0\rangle_a |0\rangle_b = \exp(\chi\hat{b}\hat{a} - \chi^*\hat{a}^\dagger\hat{b}^\dagger) |0\rangle_a |0\rangle_b , \tag{9.3}$$

where $\hat{S}_2(\chi)$ is the two-mode squeezing operator and $\chi = re^{i\theta}$, with $r = gt$, is the two-mode squeezing parameter. In the number state basis, the TMSV state can be written as [35]

$$|\chi\rangle = \frac{1}{\cosh(r)} \sum_{n=0}^{\infty} (-e^{i\theta} \tanh r)^n |n\rangle_a |n\rangle_b \tag{9.4}$$

which shows that the two modes are highly correlated (if one mode were measured to have n quanta, the other mode would also be found to contain n quanta with certainty). Because of this, two-mode squeezed states are important for continuous-variable entanglement and for investigations

the Einstein-Rosen-Podolsky paradox [35, 127]. If only one of the modes is considered (i.e. if we trace over the other mode), the density matrix for the system is given by

$$\begin{aligned}\hat{\rho}_a &= \sum_{l=0}^{\infty} \langle l|_b \left[|\chi\rangle \langle\chi|\right] |l\rangle_b \\ &= \frac{1}{\cosh^2(r)} \sum_{n=0}^{\infty} \tanh^{2n}(r) \, |n\rangle \langle n| \,, \end{aligned} \tag{9.5}$$

which describes a thermal distribution. Two-mode squeezed states also appear in the theory of the Unruh effect [128] where an observer accelerating uniformly through empty space (the vacuum state of an arbitrary electric field mode according to non-accelerating observers), will instead observe a thermal distribution of photons. This is because the accelerating observer can only receive signals from a restricted portion of space-time. The Unruh effect is closely related to Hawking radiation from black holes [129], which is one of the few connections between quantum field theory and gravity. While two-mode squeezing has been implemented with optical systems[130] and in superconduting systems [131], to the best of my knowledge, it has not been demonstrated with trapped ions. I am confident that laser-free parametric modulation will enable investigations of two-mode squeezing in trapped ions in the near future.

9.2 Continuous-variable quantum information processing

There are several distinct paradigms for quantum information processing. The main approach is known as discrete-variable QIP, where the observables of the quantum processor have a discrete spectrum. Such systems are usually composed of qubits (two level systems), and unitary operations are used to perform operations on the qubits. Alternatively, the continuous degrees of freedom of quantum systems can be used for encoding and processing information. This approach is known as continuous variable (CV) QIP. A requirement for a universal CV quantum processor is a universal set of continuous quantum operations. For a particular set of transformations, a set of continuous operations is universal if any transformation in the set can be approached arbitrarily closely by a finite number of applications of the operations [132]. For a CV quantum computer, where the

quadrature operators of an oscillator are the observables, a universal set consists of linear (or Gaussian) operations: displacement, squeezing, beam splitting, and phase-shifting and a single nonlinear (non-Gaussian) operation [132, 133, 134]. In the context of trapped ions, all of the linear operations can be implemented using laser-free modulation schemes. The nonlinear operation could be realized by using higher-order parametric modulation, which would require reasonably strong nonlinearities in the trapping potential. For example, if the trap potential has an appropriate cubic component, a Hamiltonian of the form $\hat{H} \propto \hat{a}^3 + a^{\dagger 3}$ can be implemented by modulating the potential at 3 times the mode frequency. Alternatively, a nonlinear operation can be realized by coupling the ion motion to its qubit state, to take advantage of the intrinsic nonlinearity of the two level system [135].

Another approach for using continuous degrees of freedom for quantum information processors is to encode a qubit in an higher-dimensional quantum system such as a harmonic oscillator. This approach has advantages for quantum error correction. One proposed oscillator code due to Gottesman, Kitaev and Preskill [136] (GKP), encodes qubits on grid states (multi-component superpositions of displaced squeezed states). This encoding was demonstrated on an approximation to ideal grid state by the ETH group [137], where preparation of squeezed states was achieved using laser-based reservoir engineering. The amount of squeezing was found to be a limiting factor for this experiment. Parametric modulation could enable stronger squeezing, permitting the construction of more ideal grid states and further investigations of the GKP code for error-corrected QIP[137].

9.3 Improving coherence in trapped-ion systems limited by qubit decoherence

In trapped-ion systems where effective spin-spin interactions are generated using laser beams, off-resonant light scattering can be the largest source of decoherence [4, 24, 117, 118]. While it is possible to suppress photon scattering by using more laser power and increasing the detuning of the laser from atomic resonances, other errors can come into play [138]. In chapter 8, we presented experiments where parametric modulation was used to improve the fidelity of a two-qubit gate in

the presence of qubit decoherence [104]. However, we also determined that parametric amplification can significantly amplify motional decoherence, and that there is an optimal parametric coupling strength for achieving maximum fidelity. This result motivates further investigation of parametric amplification in to systems limited by photon scattering. We are planning to implement a parametric drive in the NIST Penning trap, where increased coherence enabled by parametric modulation could allow improved spin squeezing [14] and sensing [139] with hundreds of ions.

Bibliography

[1] I. Bloch, J. Dalibard, and W. Zwerger, Rev. Mod. Phys. **80**, 885 (2008).

[2] A. D. Ludlow, M. M. Boyd, J. Ye, E. Peik, and P. O. Schmidt, Rev. Mod. Phys. **87**, 637 (2015).

[3] S. Slussarenko and G. J. Pryde, Appl. Phys. Rev. **6**, 041303 (2019).

[4] C. D. Bruzewicz, J. Chiaverini, R. McConnell, and J. M. Sage, Appl. Phys. Rev. **6**, 021314 (2019).

[5] A. Blais, S. M. Girvin, and W. D. Oliver, Nat. Phys. , 1 (2020).

[6] C. M. Caves, Phys. Rev. D **23**, 1693 (1981).

[7] D. J. Wineland, J. J. Bollinger, W. M. Itano, F. L. Moore, and D. J. Heinzen, Phys. Rev. A **46**, R6797 (1992).

[8] D. J. Wineland, J. J. Bollinger, W. M. Itano, and D. J. Heinzen, Phys. Rev. A **50**, 67 (1994).

[9] M. Kitagawa and M. Ueda, Phys. Rev. A **47**, 5138 (1993).

[10] R. E. Slusher, L. W. Hollberg, B. Yurke, J. C. Mertz, and J. F. Valley, Phys. Rev. Lett. **55**, 2409 (1985).

[11] V. Meyer, M. A. Rowe, D. Kielpinski, C. A. Sackett, W. M. Itano, C. Monroe, and D. J. Wineland, Phys. Rev. Lett. **86**, 5870 (2001).

[12] O. Hosten, N. J. Engelsen, R. Krishnakumar, and M. A. Kasevich, Nature **529**, 505 (2016).

[13] K. C. Cox, G. P. Greve, J. M. Weiner, and J. K. Thompson, Phys. Rev. Lett. **116**, 093602 (2016).

[14] J. G. Bohnet, B. C. Sawyer, J. W. Britton, M. L. Wall, A. M. Rey, M. Foss-Feig, and J. J. Bollinger, Science **352**, 1297 (2016).

[15] L. Pezzè, A. Smerzi, M. K. Oberthaler, R. Schmied, and P. Treutlein, Rev. Mod. Phys. **90**, 035005 (2018).

[16] E. E. Wollman, C. U. Lei, A. J. Weinstein, J. Suh, A. Kronwald, F. Marquardt, A. A. Clerk, and K. C. Schwab, Science **349**, 952 (2015).

[17] F. Lecocq, J. B. Clark, R. W. Simmonds, J. Aumentado, and J. D. Teufel, Phys. Rev. X **5**, 041037 (2015).

[18] J.-M. Pirkkalainen, E. Damskägg, M. Brandt, F. Massel, and M. A. Sillanpää, Phys. Rev. Lett. **115**, 243601 (2015).

[19] D. M. Meekhof, C. Monroe, B. E. King, W. M. Itano, and D. J. Wineland, Phys. Rev. Lett. **76**, 1796 (1996).

[20] D. Kienzler, H.-Y. Lo, B. Keitch, L. de Clercq, F. Leupold, F. Lindenfelser, M. Marinelli, V. Negnevitsky, and J. P. Home, Science **347**, 53 (2015).

[21] J. Aasi et al., Nat. Photon. **7**, 613 (2013).

[22] Y. Wu, R. Krishnakumar, J. Martínez-Rincón, B. K. Malia, O. Hosten, and M. A. Kasevich, "Retrieval of cavity-generated atomic spin-squeezing after free-space release," (2019), arXiv:1912.08334 [quant-ph] .

[23] B. Braverman, A. Kawasaki, E. Pedrozo-Peñafiel, S. Colombo, C. Shu, Z. Li, E. Mendez, M. Yamoah, L. Salvi, D. Akamatsu, Y. Xiao, and V. Vuletić, Phys. Rev. Lett. **122**, 223203 (2019).

[24] J. W. Britton, B. C. Sawyer, A. C. Keith, C.-C. J. Wang, J. K. Freericks, H. Uys, M. J. Biercuk, and J. J. Bollinger, Nature **484**, 489 (2012).

[25] D. J. Heinzen and D. J. Wineland, Phys. Rev. A **42**, 2977 (1990).

[26] V. Natarajan, F. DiFilippo, and D. E. Pritchard, Phys. Rev. Lett. **74**, 2855 (1995).

[27] N. Yu, H. Dehmelt, and W. Nagourney, J. Appl. Phys **73**, 8650 (1993).

[28] G. Maslennikov, S. Ding, R. Hablützel, J. Gan, A. Roulet, S. Nimmrichter, J. Dai, V. Scarani, and D. Matsukevich, Nat. Commun. **10**, 1 (2019).

[29] J. J. Sakurai and J. Napolitano, Modern quantum mechanics (Pearson Harlow, 2014).

[30] C. C. Gerry and P. L. Knight, Introductory Quantum Optics (Cambridge University Press, 2005).

[31] E. Wigner, Phys. Rev. **40**, 749 (1932).

[32] S. Haroche and J.-M. Raimond, Exploring the quantum: atoms, cavities, and photons (Oxford university press, 2006).

[33] P. Carruthers and M. Nieto, Am. J. Phys **33**, 537 (1965).

[34] N. N. Bogoljubov, Il Nuovo Cimento **7**, 794 (1958).

[35] D. F. Walls and G. J. Milburn, Quantum Optics (Springer-Verlag, 1994).

[36] S. Brewer, J.-S. Chen, A. Hankin, E. Clements, C.-W. Chou, D. Wineland, D. Hume, and D. Leibrandt, Phys. Rev. Lett. **123**, 033201 (2019).

[37] K. Kim, M.-S. Chang, S. Korenblit, R. Islam, E. E. Edwards, J. K. Freericks, G.-D. Lin, L.-M. Duan, and C. Monroe, Nature **465**, 590 (2010).

[38] J. T. Barreiro, M. Müller, P. Schindler, D. Nigg, T. Monz, M. Chwalla, M. Hennrich, C. F. Roos, P. Zoller, and R. Blatt, Nature **470**, 486 (2011).

[39] A. Khromova, C. Piltz, B. Scharfenberger, T. F. Gloger, M. Johanning, A. F. Varón, and C. Wunderlich, Phys. Rev. Lett. **108**, 220502 (2012).

[40] F. Diedrich, J. C. Bergquist, W. M. Itano, and D. J. Wineland, Phys. Rev. Lett. **62**, 403 (1989).

[41] D. J. Wineland, C. Monroe, W. M. Itano, D. Leibfried, B. E. King, and D. M. Meekhof, J. Res. Natl. Inst. Stand. Technol. **103**, 259 (1998).

[42] K. C. McCormick, J. Keller, S. C. Burd, D. J. Wineland, A. C. Wilson, and D. Leibfried, Nature **572**, 86 (2019).

[43] A. Sørensen and K. Mølmer, Phys. Rev. Lett. **82**, 1971 (1999).

[44] C. Monroe, D. M. Meekhof, B. E. King, and D. J. Wineland, Science **272**, 1131 (1996).

[45] W. H. Zurek, Nature **412**, 712 (2001).

[46] F. Toscano, D. A. Dalvit, L. Davidovich, and W. H. Zurek, Phys. Rev. A **73**, 023803 (2006).

[47] C. Hempel, B. P. Lanyon, P. Jurcevic, R. Gerritsma, R. Blatt, and C. F. Roos, Nat. Photonics **7**, 630 (2013).

[48] K. Mølmer and A. Sørensen, Phys. Rev. Lett. **82**, 1835 (1999).

[49] C. A. Sackett, D. Kielpinski, B. E. King, C. Langer, V. Meyer, C. J. Myatt, M. Rowe, Q. Turchette, W. M. Itano, D. J. Wineland, and C. Monroe, Nature **404**, 256 (2000).

[50] P. J. Lee, K.-A. Brickman, L. Deslauriers, P. C. Haljan, L.-M. Duan, and C. Monroe, J. Opt. B **7**, S371 (2005).

[51] G. Milburn, S. Schneider, and D. James, Fortschritte der Phys. **48**, 801 (2000).

[52] D. Leibfried, B. DeMarco, V. Meyer, D. Lucas, M. Barrett, J. Britton, W. M. Itano, B. Jelenković, C. Langer, T. Rosenband, et al., Nature **422**, 412 (2003).

[53] M. Brownnutt, M. Kumph, P. Rabl, and R. Blatt, Rev. Mod. Phys. **87**, 1419 (2015).

[54] I. Talukdar, D. Gorman, N. Daniilidis, P. Schindler, S. Ebadi, H. Kaufmann, T. Zhang, and H. Häffner, Phys. Rev. A **93**, 043415 (2016).

[55] C. Gardiner, P. Zoller, and P. Zoller, Quantum noise (Springer Science & Business Media, 2004).

[56] M. Sepiol, A high-fidelity microwave driven two-qubit quantum logic gate in 43Ca+, Ph.D. thesis, University of Oxford (2016).

[57] J. Johansson, P. Nation, and F. Nori, Comput. Phys. Commun. **184**, 1234 (2013).

[58] Q. A. Turchette, C. J. Myatt, B. E. King, C. A. Sackett, D. Kielpinski, W. M. Itano, C. Monroe, and D. J. Wineland, Phys. Rev. A **62**, 053807 (2000).

[59] W. Paul, Rev. Mod. Phys. **62**, 531 (1990).

[60] D. Leibfried, R. Blatt, C. Monroe, and D. J. Wineland, Rev. Mod. Phys. **75**, 281 (2003).

[61] J. Chiaverini, R. B. Blakestad, J. Britton, J. D. Jost, C. Langer, D. Leibfried, R. Ozeri, and D. J. Wineland, Quant. Inf. Comp. **5**, 419 (2005).

[62] S. Seidelin, J. Chiaverini, R. Reichle, J. J. Bollinger, D. Leibfried, J. Britton, J. H. Wesenberg, R. B. Blakestad, R. J. Epstein, D. B. Hume, W. M. Itano, J. D. Jost, C. Langer, R. Ozeri, N. Shiga, and D. J. Wineland, Phys. Rev. Lett. **96**, 253003 (2006).

[63] C. Ospelkaus, U. Warring, Y. Colombe, K. R. Brown, J. M. Amini, D. Leibfried, and D. J. Wineland, Nature **476**, 181 (2011).

[64] T. P. Harty, High-fidelity microwave-driven quantum logic in intermediate-field $^{43}Ca^{+}$, Ph.D. thesis, University of Oxford (2013).

[65] R. Bowler, U. Warring, J. W. Britton, B. Sawyer, and J. Amini, Rev. Sci. Instrum. **84**, 033108 (2013).

[66] J. Labaziewicz, Y. Ge, D. R. Leibrandt, S. X. Wang, R. Shewmon, and I. L. Chuang, Phys. Rev. Lett. **101**, 180602 (2008).

[67] J. A. Sedlacek, A. Greene, J. Stuart, R. McConnell, C. D. Bruzewicz, J. M. Sage, and J. Chiaverini, Phys. Rev. A **97**, 020302 (2018).

[68] D. An, C. Matthiesen, E. Urban, and H. Häffner, Phys. Rev. A **100**, 063405 (2019).

[69] C. Ospelkaus, C. E. Langer, J. M. Amini, K. R. Brown, D. Leibfried, and D. J. Wineland, Phys. Rev. Lett. **101**, 090502 (2008).

[70] C. Langer, R. Ozeri, J. D. Jost, J. Chiaverini, B. DeMarco, A. Ben-Kish, R. Blakestad, J. Britton, D. Hume, W. M. Itano, et al., Phys. Rev. Lett. **95**, 060502 (2005).

[71] G. Clos, M. Enderlein, U. Warring, T. Schaetz, and D. Leibfried, Phys. Rev. Lett. **112**, 113003 (2014).

[72] D. J. Wineland and W. M. Itano, Phys. Rev. A **20**, 1521 (1979).

[73] D. Wineland and H. Dehmelt, Bull. Am. Phys. Soc. **20**, 637 (1975).

[74] U. Warring, C. Ospelkaus, Y. Colombe, R. Jördens, D. Leibfried, and D. J. Wineland, Phys. Rev. Lett. **110**, 173002 (2013).

[75] S. Bourdeauducq et al., Zenodo. 10.5281/zenodo.51303 (2016).

[76] M. L. Eickhoff and J. L. Hall, IEEE Trans. Instrum. Meas. **44**, 155 (1995).

[77] J. H. Shirley, Opt. Lett. **7**, 537 (1982).

[78] J. J. Snyder, R. K. Raj, D. Bloch, and M. Ducloy, Opt. Lett. **5**, 163 (1980).

[79] A. C. Wilson, C. Ospelkaus, A. VanDevender, J. A. Mlynek, K. R. Brown, D. Leibfried, and D. J. Wineland, Appl. Phys. B **105**, 741 (2011).

[80] Y. Colombe, D. H. Slichter, A. C. Wilson, D. Leibfried, and D. J. Wineland, Opt. Express **22**, 19783 (2014).

[81] D. T. C. Allcock, Surface-electrode ion traps for scalable quantum computing, Ph.D. thesis, Oxford University, UK (2011).

[82] H. Hahn, G. Zarantonello, M. Schulte, A. Bautista-Salvador, K. Hammerer, and C. Ospelkaus, Npj Quantum Inf. **5**, 1 (2019).

[83] U. Warring, C. Ospelkaus, Y. Colombe, K. R. Brown, J. M. Amini, M. Carsjens, D. Leibfried, and D. J. Wineland, Phys. Rev. A **87**, 013437 (2013).

[84] H.-Y. Lo, D. Kienzler, L. de Clercq, M. Marinelli, V. Negnevitsky, B. C. Keitch, and J. P. Home, Nature **521**, 336 (2015).

[85] A. Bermudez, P. O. Schmidt, M. B. Plenio, and A. Retzker, Phys. Rev. A **85**, 040302 (2012).

[86] T. P. Harty, M. A. Sepiol, D. T. Allcock, C. J. Ballance, J. E. Tarlton, and D. M. Lucas, Phys. Rev. Lett. **117**, 140501 (2016).

[87] S. Burd, R. Srinivas, J. Bollinger, A. Wilson, D. Wineland, D. Leibfried, D. Slichter, and D. Allcock, Science **364**, 1163 (2019).

[88] C. M. Caves, "Reframing SU(1,1) interferometry," (2019), arXiv:1912.12530 [quant-ph] .

[89] M. S. Safronova, D. Budker, D. DeMille, D. F. J. Kimball, A. Derevianko, and C. W. Clark, Rev. Mod. Phys. **90**, 025008 (2018).

[90] B. P. Abbott et al., Phys. Rev. Lett. **116**, 061102 (2016).

[91] H.-J. Butt, B. Cappella, and M. Kappl, Surf. Sci. Rep. **59**, 1 (2005).

[92] M. Aspelmeyer, T. J. Kippenberg, and F. Marquardt, Rev. Mod. Phys. **86**, 1391 (2014).

[93] M. J. Biercuk, H. Uys, J. W. Britton, A. P. VanDevender, and J. J. Bollinger, Nat. Nanotechnol. **5**, 646 (2010).

[94] B. Yurke, S. L. McCall, and J. R. Klauder, Phys. Rev. A **33**, 4033 (1986).

[95] E. Davis, G. Bentsen, and M. Schleier-Smith, Phys. Rev. Lett. **116**, 053601 (2016).

[96] D. Linnemann, H. Strobel, W. Muessel, J. Schulz, R. J. Lewis-Swan, K. V. Kheruntsyan, and M. K. Oberthaler, Phys. Rev. Lett. **117**, 013001 (2016).

[97] M. Malnou, D. A. Palken, B. M. Brubaker, L. R. Vale, G. C. Hilton, and K. W. Lehnert, Phys. Rev. X **9**, 021023 (2019).

[98] A. Eddins, S. Schreppler, D. M. Toyli, L. S. Martin, S. Hacohen-Gourgy, L. C. G. Govia, H. Ribeiro, A. A. Clerk, and I. Siddiqi, Phys. Rev. Lett. **120**, 040505 (2018).

[99] M. M. Nieto and D. R. Truax, Fortschr. Phys. **45**, 145 (1997).

[100] A. I. Lvovsky, "Squeezed light," (2014), arXiv:1401.4118 [quant-ph] .

[101] W. M. Itano, J. C. Bergquist, J. J. Bollinger, J. Gilligan, D. J. Heinzen, F. Moore, M. Raizen, and D. J. Wineland, Phys. Rev. A **47**, 3554 (1993).

[102] W. J. Munro, K. Nemoto, G. J. Milburn, and S. L. Braunstein, Phys. Rev. A **66**, 023819 (2002).

[103] Y. Wan, F. Gebert, J. B. Wübbena, N. Scharnhorst, S. Amairi, I. D. Leroux, B. Hemmerling, N. Lörch, K. Hammerer, and P. O. Schmidt, Nat. Commun. **5**, 3096 (2014).

[104] W. Ge, B. C. Sawyer, J. W. Britton, K. Jacobs, J. J. Bollinger, and M. Foss-Feig, Phys. Rev. Lett. **122**, 030501 (2019).

[105] C. Arenz, D. I. Bondar, D. Burgarth, C. Cormick, and H. Rabitz, Quantum **4**, 271 (2020).

[106] M. A. Nielsen and I. Chuang, Cambridge University Press (Pearson Harlow, 2000).

[107] M. Tavis and F. W. Cummings, Phys. Rev. **170**, 379 (1968).

[108] J. Majer, J. M. Chow, J. M. Gambetta, J. Koch, B. R. Johnson, J. A. Schreier, L. Frunzio, D. I. Schuster, A. A. Houck, A. Wallraff, A. Blais, M. H. Devoret, S. M. Girvin, and R. J. Schoelkopf, Nature **449**, 443 (2007).

[109] A. Blais, R.-S. Huang, A. Wallraff, S. M. Girvin, and R. J. Schoelkopf, Phys. Rev. A **69**, 062320 (2004).

[110] R. E. Evans, M. K. Bhaskar, D. D. Sukachev, C. T. Nguyen, A. Sipahigil, M. J. Burek, B. Machielse, G. H. Zhang, A. S. Zibrov, E. Bielejec, H. Park, M. Lončar, and M. D. Lukin, Science **362**, 662 (2018).

[111] J. I. Cirac and P. Zoller, Phys. Rev. Lett. **74**, 4091 (1995).

[112] A. P. Higginbotham, P. S. Burns, M. D. Urmey, R. W. Peterson, N. S. Kampel, B. M. Brubaker, G. Smith, K. W. Lehnert, and C. A. Regal, Nat. Phys. **14**, 1038 (2018).

[113] M.-A. Lemonde, N. Didier, and A. A. Clerk, Nat. Commun. **7**, 11338 (2016).

[114] Y.-H. Chen, W. Qin, and F. Nori, Phys. Rev. A **100**, 012339 (2019).

[115] W. Qin, A. Miranowicz, P.-B. Li, X.-Y. Lü, J. Q. You, and F. Nori, Phys. Rev. Lett. **120**, 093601 (2018).

[116] R. Barends, J. Kelly, A. Megrant, A. Veitia, D. Sank, E. Jeffrey, T. C. White, J. Mutus, A. G. Fowler, B. Campbell, et al., Nature **508**, 500 (2014).

[117] J. P. Gaebler, T. R. Tan, Y. Lin, Y. Wan, R. Bowler, A. C. Keith, S. Glancy, K. Coakley, E. Knill, D. Leibfried, and D. J. Wineland, Phys. Rev. Lett. **117**, 060505 (2016).

[118] C. J. Ballance, T. P. Harty, N. M. Linke, M. A. Sepiol, and D. M. Lucas, Phys. Rev. Lett. **117**, 060504 (2016).

[119] R. Mottl, F. Brennecke, K. Baumann, R. Landig, T. Donner, and T. Esslinger, Science **336**, 1570 (2012).

[120] J. Léonard, A. Morales, P. Zupancic, T. Esslinger, and T. Donner, Nature **543**, 87 (2017).

[121] C. Monroe, D. M. Meekhof, B. E. King, S. R. Jefferts, W. M. Itano, D. J. Wineland, and P. Gould, Phys. Rev. Lett. **75**, 4011 (1995).

[122] A. C. Keith, C. H. Baldwin, S. Glancy, and E. Knill, Phys. Rev. A **98**, 042318 (2018).

[123] J. Tellinghuisen, The Journal of Physical Chemistry A **105**, 3917 (2001).

[124] K. R. Brown, C. Ospelkaus, Y. Colombe, A. C. Wilson, D. Leibfried, and D. J. Wineland, Nature **471**, 196 (2011).

[125] D. J. Gorman, P. Schindler, S. Selvarajan, N. Daniilidis, and H. Häffner, Phys. Rev. A **89**, 062332 (2014).

[126] K. Toyoda, R. Hiji, A. Noguchi, and S. Urabe, Nature **527**, 74 (2015).

[127] Z. Y. Ou, S. F. Pereira, H. J. Kimble, and K. C. Peng, Phys. Rev. Lett. **68**, 3663 (1992).

[128] W. G. Unruh, Phys. Rev. D **14**, 870 (1976).

[129] S. W. Hawking, Nature **248**, 30 (1974).

[130] A. Heidmann, R. J. Horowicz, S. Reynaud, E. Giacobino, C. Fabre, and G. Camy, Phys. Rev. Lett. **59**, 2555 (1987).

[131] C. Eichler, D. Bozyigit, C. Lang, M. Baur, L. Steffen, J. M. Fink, S. Filipp, and A. Wallraff, Phys. Rev. Lett. **107**, 113601 (2011).

[132] S. L. Braunstein and P. van Loock, Rev. Mod. Phys. **77**, 513 (2005).

[133] D. Leibfried, B. DeMarco, V. Meyer, M. Rowe, A. Ben-Kish, J. Britton, W. M. Itano, B. Jelenković, C. Langer, T. Rosenband, and D. J. Wineland, Phys. Rev. Lett. **89**, 247901 (2002).

[134] U. L. Andersen, G. Leuchs, and C. Silberhorn, Laser Photonics Rev. **4**, 337 (2010).

[135] L. Ortiz-Gutiérrez, B. Gabrielly, L. F. Muñoz, K. T. Pereira, J. G. Filgueiras, and A. S. Villar, Opt. Commun. **397**, 166 (2017).

[136] D. Gottesman, A. Kitaev, and J. Preskill, Phys. Rev. A **64**, 012310 (2001).

[137] C. Flühmann, T. L. Nguyen, M. Marinelli, V. Negnevitsky, K. Mehta, and J. P. Home, Nature **566**, 513 (2019).

[138] H. Uys, M. J. Biercuk, A. P. VanDevender, C. Ospelkaus, D. Meiser, R. Ozeri, and J. J. Bollinger, Phys. Rev. Lett. **105**, 200401 (2010).

[139] K. A. Gilmore, J. G. Bohnet, B. C. Sawyer, J. W. Britton, and J. J. Bollinger, Phys. Rev. Lett. **118**, 263602 (2017).

[140] W. Magnus, Commun. Pure Appl. Math. **7**, 649 (1954).

[141] S. Burd, D. Leibfried, A. C. Wilson, and D. Wineland, in Vertical External Cavity Surface Emitting Lasers (VECSELs) V, Vol. 9349 (International Society for Optics and Photonics, 2015) p. 93490P.

[142] M. Guina, A. Rantamäki, and A. Härkönen, J. Phys. D **50**, 383001 (2017).

[143] S. C. Burd, D. T. C. Allcock, T. Leinonen, J. P. Penttinen, D. H. Slichter, R. Srinivas, A. C. Wilson, R. Jördens, M. Guina, D. Leibfried, and D. J. Wineland, Optica **3**, 1294 (2016).

[144] S. Burd, J.-P. Penttinen, P.-Y. Hou, H. Knaack, S. Ranta, M. Mäki, E. Kantola, M. Guina, D. Slichter, D. Leibfried, et al., arXiv preprint arXiv:2003.09060 (2020).

[145] M. Kuznetsov, F. Hakimi, R. Sprague, and A. Mooradian, IEEE Photon. Technol. Lett. **9**, 1063 (1997).

[146] A. Tropper and S. Hoogland, Prog. Quantum. Electron. **30**, 1 (2006).

[147] A. Garnache, A. Ouvrard, and D. Romanini, Opt. Express **15**, 9403 (2007).

[148] A. Laurain, C. Mart, J. Hader, J. V. Moloney, B. Kunert, and W. Stolz, Opt. Lett. **39**, 1573 (2014).

[149] A. Laurain, J. Hader, and J. V. Moloney, J. Opt. Soc. Am. B **36**, 847 (2019)

Appendix A

Magnus Expansion

The Magnus expansion [140] gives a series solution to differential equations of the form

$$\frac{d\hat{X}(t,t_0)}{dt} = \hat{A}(t)\hat{X}(t,t_0) \tag{A.1}$$

If the operator $\hat{A}(t)$ does not commute with itself at different times, i.e. if $[\hat{A}(t), \hat{A}(t')] \neq 0$, then the solution can be expressed as

$$\hat{X}(t,t_0) = \exp\left(\sum_{n=1}^{\infty} C_n(t)\right)\hat{X}(t_0,t_0) \tag{A.2}$$

where

$$\begin{aligned}
C_1(t) &= \int_{t_0}^{t} A(t')dt' \\
C_2(t) &= \frac{1}{2}\int_{t_0}^{t}\int_{t_0}^{t'} [A(t'), A(t'')]dt'dt'' \qquad \text{(A.3)} \\
C_3(t) &= \frac{1}{6}\int_{t_0}^{t}\int_{t_0}^{t'}\int_{t_0}^{t''} ([A(t'), [A(t''), A(t''')]] + [A(t'''), [A(t''), A(t')]])dt'dt''dt''' \qquad \text{(A.4)} \\
&\vdots
\end{aligned}$$

The Magnus expansion has the useful property that if $C_i(t) = 0$, all high order contributions vanish and the series truncates. In quantum mechanics, the time evolution operator is given by the Schrodinger equation

$$i\hbar\frac{d\hat{U}(t,t_0)}{dt} = \hat{H}\hat{U}(t,t_0), \tag{A.5}$$

which can be solved using the Magnus expansion method with $\hat{A} \to -i\frac{\hat{H}}{\hbar}$.

Appendix B

Thermal state density matrix

The density matrix for a system in thermal equilibrium is given by [29]

$$\hat{\rho}_{th} = \frac{e^{-\beta \hat{H}}}{Z} \tag{B.1}$$

where Z is the partition function and $\beta = 1/k_B T$. For a one dimensional harmonic oscillator $\hat{H} = \hbar\omega_z(\hat{n} + 1/2)$ and

$$e^{-\beta \hat{H}} = e^{-\frac{\hbar\omega_z}{2}} \sum_{n=0}^{\infty} e^{-\beta\hbar\omega_z n} \left|n\right\rangle \left\langle n\right| . \tag{B.2}$$

With

$$Z = e^{-\frac{\hbar\omega_z}{2}} \sum_{n=0}^{\infty} e^{-\beta\hbar\omega_z n} = e^{-\frac{\hbar\omega_z}{2}} \frac{1}{1 - e^{-\hbar\omega_z\beta}}, \tag{B.3}$$

the thermal density matrix can be written as

$$\hat{\rho}_{th} = (1 - e^{-\hbar\omega_z\beta}) \sum_{n=0}^{\infty} e^{-\beta\hbar\omega_z n} \left|n\right\rangle \left\langle n\right| . \tag{B.4}$$

In typical ion trapping experiments, the quantity that can be measured easily is

$$\begin{aligned} \bar{n} &= Tr[\hat{\rho}_{th}\hat{n}] \\ &= (1 - e^{-\hbar\omega_z\beta}) \sum_{n=0}^{\infty} n e^{-\beta\hbar\omega_z n} \\ &= \frac{1}{e^{\beta\hbar\omega_z} - 1} \end{aligned} \tag{B.5}$$

Rearanging gives

$$e^{\beta\hbar\omega_z} = \frac{1+\bar{n}}{\bar{n}} \tag{B.6}$$

or

$$T = \frac{\hbar\omega_z}{k_B}\frac{1}{\ln[\frac{\bar{n}}{1+\bar{n}}]} \tag{B.7}$$

Substituting into B.4 gives

$$\hat{\rho}_{th} = \frac{1}{\bar{n}+1}\sum_{n=0}^{\infty}\left(\frac{\bar{n}}{1+\bar{n}}\right)^n |n\rangle\langle n| \tag{B.8}$$

Appendix C

Matrix elements of the displacement operator

The diagonal matrix elements for the displacement operator in the number state basis can be expanded as

$$\begin{aligned}\langle n|\,\hat{D}(\alpha)\,|n\rangle &= e^{-|\alpha|^2/2}\,\langle n|\,e^{\alpha\hat{a}^\dagger}e^{-\alpha^*\hat{a}}\,|n\rangle \\ &= \sum_{l=0}^{\infty}\sum_{k=0}^{\infty}\langle n|\,\frac{(\alpha\hat{a}^\dagger)^l}{l!}\,\frac{(-\alpha^*\hat{a})^k}{k!}\,|n\rangle\,.\end{aligned}$$

Notice that the only terms of the double sum that do not vanish must have $l = k$. Also the series will truncate after $l = n$ since terms with $n < l$ will involve annihilation of the oscillator ground state.

$$\begin{aligned}\langle n|\,\hat{D}(\alpha)\,|n\rangle &= e^{-|\alpha|^2/2}\sum_{l=0}^{n}\frac{(-1)^l(|\alpha|^2)^l\times n\times(n-1)\times(n-2)\ldots\times(n-l))}{l!l!} \\ &= e^{-|\alpha|^2/2}\sum_{l=0}^{n}(-1)^l\frac{n!}{l!^2(n-l)!}(|\alpha|^2)^l \\ &= e^{-|\alpha|^2/2}\mathcal{L}_n(|\alpha|^2) \qquad \text{(C.1)}\end{aligned}$$

where $\mathcal{L}_n(|\alpha|^2)$ is the nth Laguerre polynomial. Let us now calculate the expectation value of the displacement operator when the the initial state is a thermal field.

$$\begin{aligned}
\mathrm{Tr}[\hat{\rho}_{th}\hat{D}(\alpha)] &= \sum_{l=0}^{\infty} \langle l| \hat{\rho}_{th}\hat{D}(\alpha) |l\rangle \\
&= \sum_{l=0}^{\infty} \langle l| \frac{1}{\bar{n}+1} \sum_{n=0}^{\infty} \left(\frac{\bar{n}}{1+\bar{n}}\right)^n \hat{D}(\alpha) |n\rangle \langle n|l\rangle \\
&= \sum_{n=0}^{\infty} \frac{1}{\bar{n}+1} \left(\frac{\bar{n}}{1+\bar{n}}\right)^n \langle n| \hat{D}(\alpha) |n\rangle \\
&= \sum_{n=0}^{\infty} \frac{1}{\bar{n}+1} \left(\frac{\bar{n}}{1+\bar{n}}\right)^n e^{-|\alpha|^2/2} \mathcal{L}_n(|\alpha|^2) \qquad \text{(C.2)}
\end{aligned}$$

Finally, this expression can be simplified by using the generating function for the Laguerre polynomials,

$$\sum_{n=0}^{\infty} y^n \mathcal{L}_n(x) = \frac{1}{1-y} e^{-\frac{yx}{1-y}}, \qquad \text{(C.3)}$$

to give

$$\boxed{\mathrm{Tr}[\hat{\rho}_{th}\hat{D}(\alpha)] = e^{-(\bar{n}+1/2)|\alpha|^2}} \qquad \text{(C.4)}$$

Appendix D

Vertical external-cavity surface emitting lasers

Vertical external-cavity surface-emitting lasers (VECSELs), also known as optically-pumped semiconductor lasers (OPSLs), or semiconductor disk lasers (SDLs), offer several advantageous features for AMO physics applications [141, 142]. In this appendix I describe the infrared (IR) VECSEL design that I have developed and that we have used extensively for magnesium ion experiments [143]. The same design was also used to generate all the wavelengths typically required for beryllium ion experiments [144]. This appendix focuses on construction details and VECSEL operation. Additional details about VECSEL output power, noise characteristics, and performance in experiments can be found in the articles [143, 144].

D.1 Single-frequency VECSELs for AMO physics

A schematic diagram of the single-frequency VECSELs we use is shown in Figure D.1. The linear standing-wave laser cavity is formed by an output coupler (OC) and a semiconductor gain mirror [145]. The gain mirror (Fig. D.2) consists of multiple stacked quantum wells and a Bragg reflector that functions as one of the laser cavity mirrors [142, 146]. By positioning the quantum wells at the anti-nodes of the standing wave of the laser mode, spatial hole burning can be eliminated. The VECSEL emission wavelength is determined by the choice of semiconductor materials [142] and the geometry of the gain chip structure, and can be tailored to target relevant atomic or molecular transitions. Although the VECSEL gain material can be designed for emission in the visible or even ultraviotlet [146], in many cases it is necessary or more convenient to generate

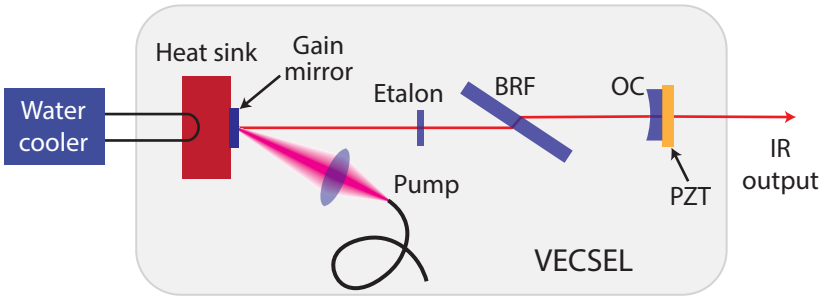

Figure D.1: Schematic diagram of a vertical external-cavity surface-emitting laser (VECSEL). BRF: birefringent filter, OC: Output coupler, PZT: piezoelectric transducer.

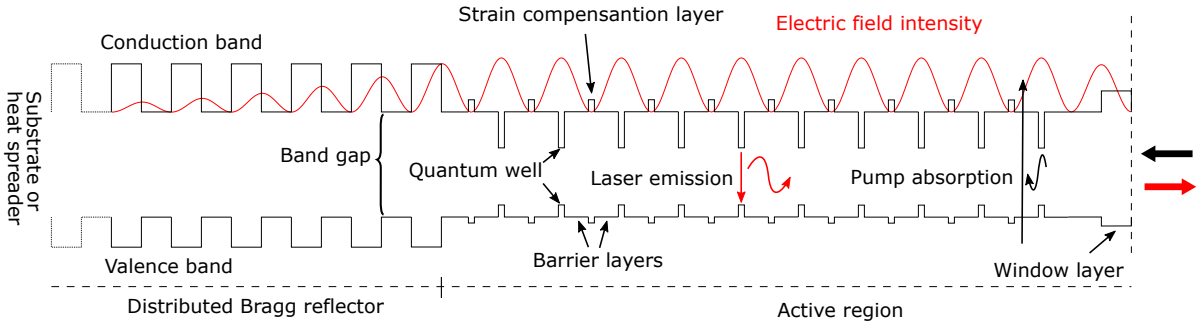

Figure D.2: Diagram of the gain chip band structure (courtesy of the Optoelectronics Research Center, Tampere University of technology, Tampere, Finland). The energies of the conduction and valence band are indicated by black rectangular features. The energy is modulated by suitable doping of the material. Inversion is created by electrons that are excited from pump absorption and then decay to the bottom of the wells due to non-radiative energy loss. The layer structure of the mirror and the external cavity favors stimulated emission from the minima of the conduction band to the maxima of the valence band (realized in the "wells"), which defines the lasing modes.

shorter wavelengths via nonlinear frequency conversion of infrared VECSELs, often because the requirement of a pump with a shorter wavelength than the VESCEL emission wavelength limits the choice of strong and convenient pump lasers and favors IR VECSELs. The relatively large gain bandwidth typically enables wavelength tuning over several 10 s of nanometers. This opens the possibility of using a single laser to target multiple fine structure transitions in a given atomic species.

The gain mirror is typically pumped with another laser; for VECSELs emitting in the infrared, this is usually a relatively cheap multimode diode laser. Optical pumping together with the external cavity enable high output power with almost diffraction-limited beam quality, which is desirable if nonlinear frequency conversion stages or fiber coupling are required. Moreover, the optically-pumped disk laser geometry is intrinsically amenable to power scaling; the active gain volume can be increased by increasing the laser mode and pump spot areas on the gain medium [146].

To enforce single-longitudinal mode operation and enable wavelength tuning, a birefringent filter (BRF) and an etalon, are placed inside the laser cavity. The short upper-state lifetime ($\sim$1 ns) in the gain medium and the relatively high finesse external cavity (giving intracavity photon lifetimes $\sim$50 ns), allow relaxation-oscillation-free operation [147] and free-running linewidths of a few 100 kHz, limited by technical noise. In contrast, rare-earth-atom doped solid-state lasers typically have long upper state ($\sim 1\,\mu$s) lifetimes and realtively low finesse laser cavities giving rise to relaxation oscillations. With active feedback from a reference cavity, single-frequency VECSELs have been demonstrated with linewidths of 4 kHz and 15 W output power [148].

D.2 Infrared VECSEL

At NIST, we have developed a custom single-frequency VECSEL that has replaced fiber and dye laser based systems in several experiments that use magnesium ions. An annotated photograph of one of our lasers is shown in Fig. D.3. The laser cavity is formed by the gain mirror [1] and

[1] The gain mirrors are specially designed and fabricated by our collaborators at Tampere University of Technology (TUT) in Finland.

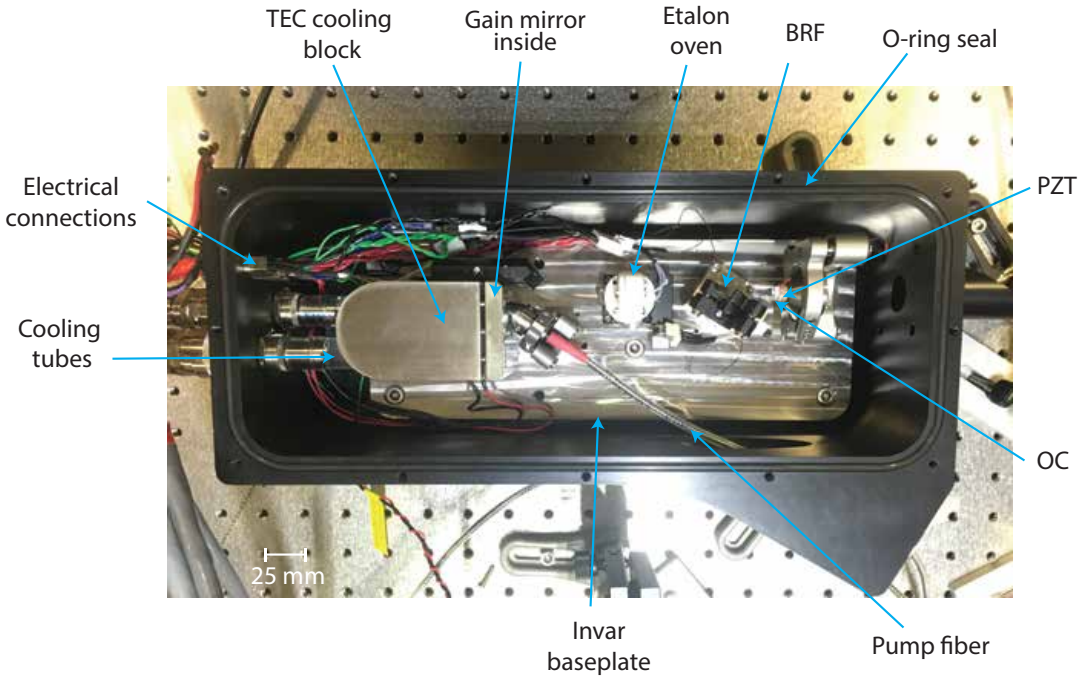

Figure D.3: Photograph the infrared (IR) VECSEL. BRF: birefringent filter, OC: Output coupler, PZT: piezoelectric transducer, TEC: thermoelectric cooler.

the output coupler, separated by $\simeq 170\,\mathrm{mm}$. A BRF and an etalon are inserted inside the laser cavity to enforce single-frequency operation and enable wavelength tuning. The laser components are attached on an invar base plate to suppress frequency drifts resulting from thermal fluctuations. The baseplate is contained within an o-ring sealed enclosure to suppress air pressure fluctuations and acoustic noise. In the following subsections, I describe several components of the VECSEL in detail. To facilitate future VECSEL construction, I have tried to list most of the commercial parts that we typically use. In many cases there are suitable substitute parts available from other vendors.

D.2.1 Gain-chip cooling block

The thermal management system for the gain chip is non trivial. Under normal operating conditions, several Watts of absorbed pump power need to be dissipated. Furthermore, for stable operation, the gain chip temperature should be controlled to within $\pm 0.01\,^{\circ}\mathrm{C}$ by means of a temperature controller[2] . To efficiently remove heat, the gain chip is mounted on a diamond heat spreader that is soldered to a copper plate heat spreader. The temperature of the copper plate near the gain chip is measured with a thermistor[3] glued to the copper plate using UV curing epoxy[4] . Heat is pumped away from the copper plate by a thermoelectric cooler (TEC)[5] . The hot side of the TEC is in contact with a water cooling plate[6] . We put layers of **non-silicone** thermal paste[7] on both sides of the TEC to ensure efficient heat transfer. The gain chip plate, TEC, and water cooling plate are clamped to the cooling block. Insulators machined from low-thermal-conductivity Mykroy glass-mica ceramic[8] limit heat conduction with the rest of the laser.

[2] Arroyo instruments 5305 TECSource
[3] TE Technology MP-2444
[4] Norland 61 (Thorlabs part number: NOA61)
[5] TE Technology HP-199-1.4-0.8
[6] Mikros 02749 Cold plate , Ni Plated. At the time of writing this part is not longer in production
[7] Silicone tends to migrate onto the gain chip.
[8] McMaster-Carr glass mica ceramic: https://www.mcmaster.com/ceramics/easy-to-machine-glass-mica-ceramic/

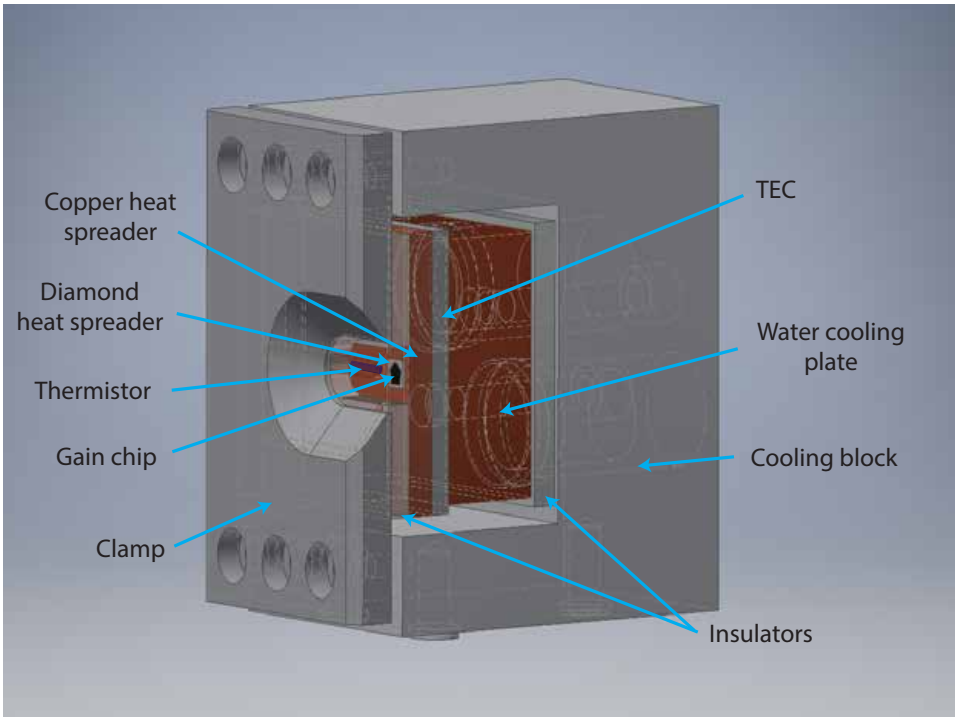

Figure D.4: 3D rendering of the gain chip cooling block. Waste heat from the gain chip is dispersed by a diamond heat spreader and a copper plate heat spreader. A thermometric cooler (TEC) pumps heat from the copper plate to the water cooling plate. The temperature of the copper plate is measured using a thermistor. Mykroy ceramic insulators limit heat transfer between the copper plate and the clamp and between the water cooling plate and the cooling block. Tubes for delivering and removing cooling water are not shown.

D.2.2 Output coupler

The output coupler (OC) allows extraction of a portion of the laser light circulating in the cavity and determines the intracavity mode geometry. We typically choose OCs with a reflectivity $R \simeq 98\%$ and a 200 mm radius of curvature [9] which gives a laser mode waist ($1/e^2$ intensity radius)on the gain chip of $\sim 160\,\mu$m. For fine tuning the laser frequency, the cavity length can be adjusted using a ring piezo electric transducer[10] connected to the OC. The piezo is bonded to a metal mount using heat curing epoxy[11] and the OC is bonded to the piezo with UV-curing epoxy[12] . For future applications requiring higher-bandwidth frequency control, a more carefully designed mount and a low mass OC may be desirable.

D.2.3 Birefringent filter

The BRF enables coarse tuning of the laser frequency (0.1 THz −1 THz range). It is an uncoated 3 mm thick quartz plate[13] inserted at Brewster's angle. As shown in Figure D.5 the BRF is glued into a Thorlabs D - mirror mount[14] using UV curing epoxy. To enable temperature measurement and control a heater[15] and temperature sensor [16] are glued to the mount using heat curing epoxy[17] . The mirror mount is screwed onto an adpater plate that is mounted on a goniomoter[18] to allow rotation of the BRF. During normal operation, the BRF temperature is controlled to within $\pm 0.05\,^{\circ}$C using a temperature controller[19] . The wavelength of the VECSEL can be coarsely adjusted by rotating the BRF or by changing the BRF set-point temperature (~ 40 GHz/K).

[9] Cavity-side radius of curvature of 200 mm, diameter 12.7 mm, back side AR coated.
[10] Noliac NAC2123, 3.3 μm maximum free stroke at 200 V
[11] Thorlabs part number: 353NDPK
[12] Norland 61 (Thorlabs part number: NOA61)
[13] Newlight Photonics BIR0030
[14] Thorlabs KM05DR
[15] Induceramic custom part
[16] Thorlabs TH100PT
[17] Thorlabs part number: 353NDPK
[18] Thorlabs GN1
[19] Arroyo instruments 5240 TECSource

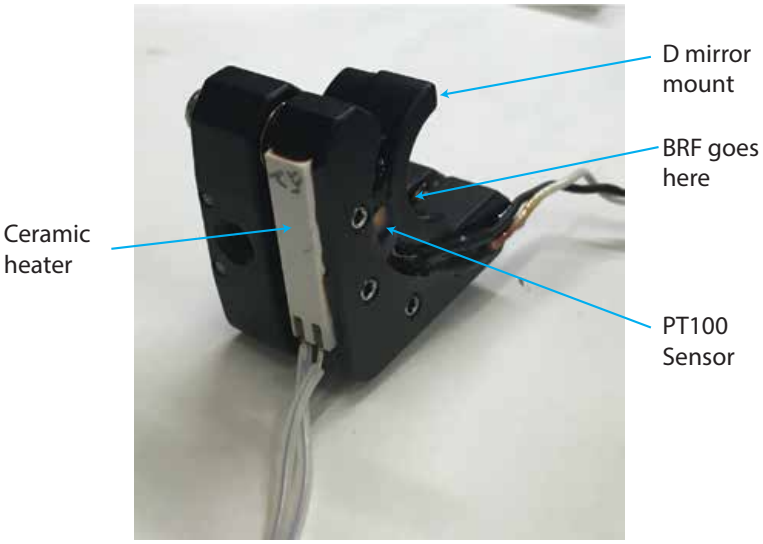

Figure D.5: Photograph of the birefringent filter (BRF) mount. The BRF plate is glued into a Thorlabs KM05DR D-shaped mirror mount. Heat is supplied by a ceramic heater glued to the side of the mount. The temperature is measured using a PT100 temperature sensor.

D.2.4 Etalon

The VECSEL contains a 1 mm thick yttrium aluminum garnet (YAG) etalon[20] with a free-spectral range of ~ 80 GHz near a wavelength of 1 μm for intermediate range tuning (1 GHz$-$100 GHz). The etalon is glued into an aluminum holder (see Fig. D.6) using UV curing epoxy[21] . A thermistor [22] and ceramic heater [23] glued to the holder enable measurement and control of the etalon temperature. The temperature is maintained to within $\pm 0.05\,^{\circ}$C a desired set point by a feedback controller[24] . The etalon holder is contained in an oven made from Macor ceramic that is mounted on a three-axis rotation stage[25] for alignment.

[20] Light Machinery OP-3167-1000
[21] Norland 61 (Thorlabs part number: NOA61)
[22] TE Technology MP-2444
[23] Induceramic custom part
[24] Arroyo instruments 5240 TECSource
[25] Opto Sigma KKD-25C

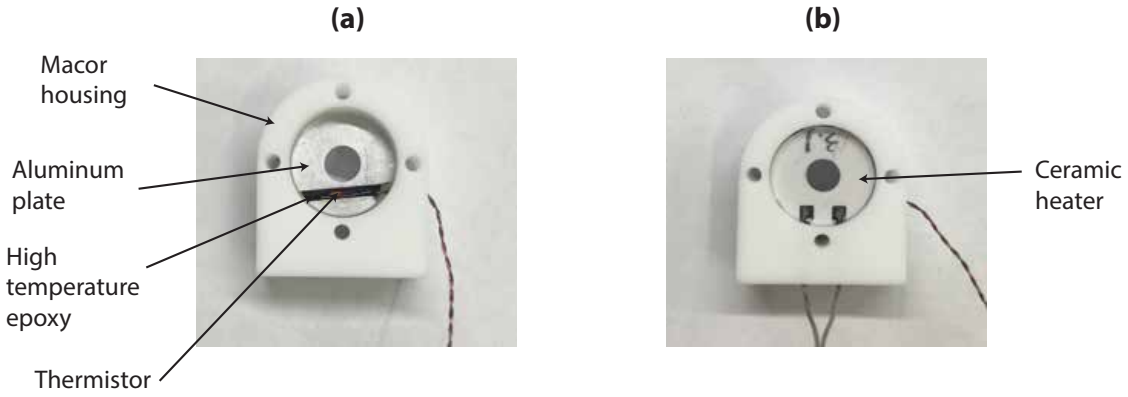

Figure D.6: Photograph of the etalon oven. (a) shows the aluminium plate that holds the the etalon (on the reverse side) with an NTC thermistor epoxied into a groove on the plate. The ceramamic heater is then expoxied onto the aluminum plate as shown in (b).

D.2.5 Pump diode

We use a fiber-coupled multi-mode pump diode [26] with a maximum output power of 50 W. The pump fiber [27] is terminated on the VECSEL side with a focussing unit ("fiber focusser") which produces a pump spot of $\sim 200\,\mu$m radius at on the gain chip. The focussing unit is secured in a mirror mount [28] so that the pump laser spot can be positioned on the gain chip. The pump spot is chosen to be slightly smaller than the laser mode ($\sim 160\,\mu$m $1/e^2$ intensity radius) to suppress oscillation of transverse modes [149].

D.3 Infrared VECSEL alignment procedure

D.3.1 Alignment of the pump diode onto the gain chip:

Remember to wear laser safety goggles! Use a camera [29] with an adjustable magnification lens[30] to image the gain chip. The pump diode current should be is set below threshold (typically to ∼6 A), so that there is spontaneous emission (from the pump diode), but not lasing. Using the camera to observe the pump spot on the gain chip, position the pump spot near the center of the gain chip (Fig. D.7) and adjust the position of the fiber focusser to minimize the pump spot size. Neutral density filters or spectral filters [31] should be used to reduce the amount of pump light reaching the camera. Next, increase the pump diode current to ∼8 A (just above the pump threshold). If defects are visible on the gain chip surface within the pump spot, move the pump spot to a region free of defects (Fig. D.8).

D.3.2 VECSEL alignment:

For coarse alignment, use a low power laser [32] as an alignment guide and two mirrors. Ensure that there is some space to insert a power meter between the VECSEL housing and the alignment

[26] Coherent M1F2S22-807.3-40C-SS2.6T3
[27] OzOptics LPF-D4-808-200-240-QM-2.2-12-6.2AS,13.9AS-35-5HPL-3A-1.5
[28] Thorlabs: K05
[29] Thorlabs DCC1545M
[30] Thorlabs MVL7000
[31] Thorlabs FEL950 or FEL1000
[32] Thorlabs CPS532

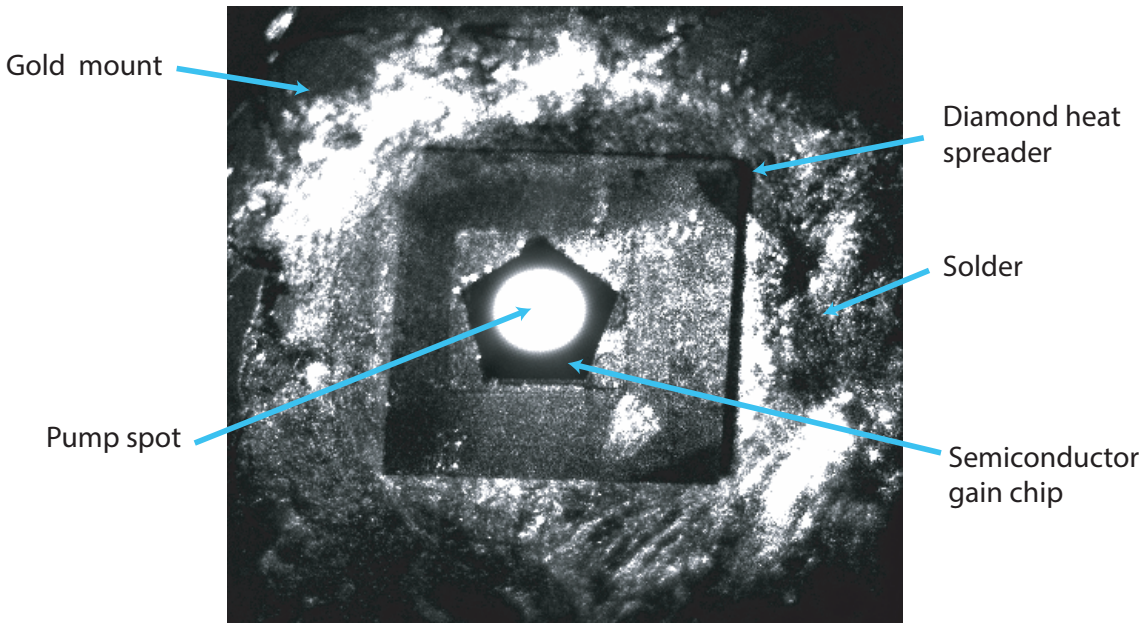

Figure D.7: Photograph of an 1120 nm gain chip under illumination with light from an 809 nm pump diode. The pump spot appears larger than it actually is as the reflected pump light is saturating the camera.

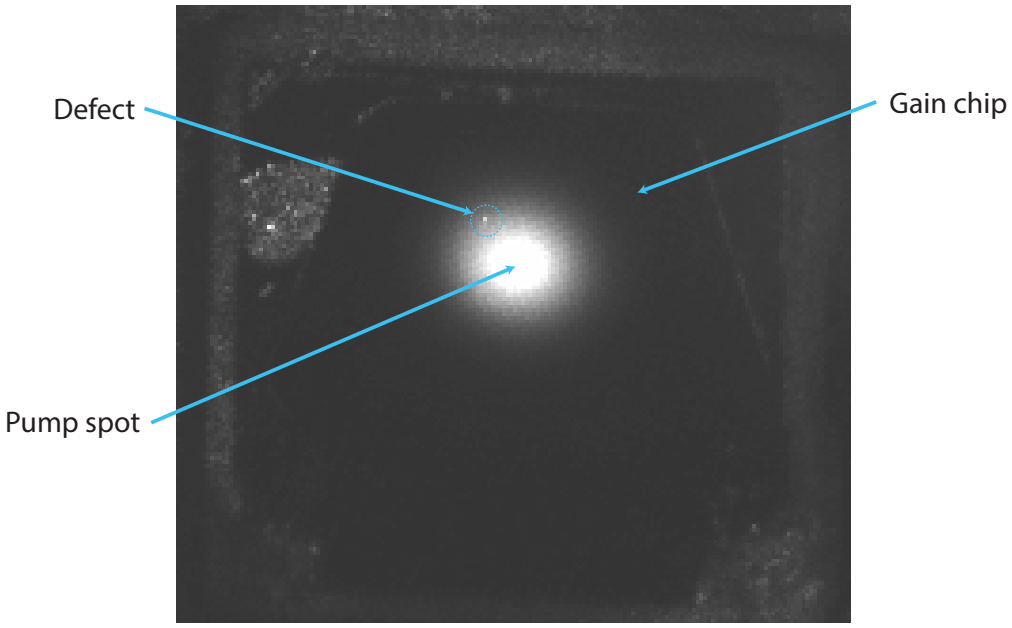

Figure D.8: Photograph of an 1120 nm gain chip showing the pump spot of the 809 nm pump diode and a defect visible as a white spot.

mirror closest to the VECSEL. Direct the alignment laser beam so that it is reflected from the center of the gain chip and that the reflected beam overlaps the incident beam. Next, insert the output coupler. With the alignment laser on, adjust the output coupler alignment so the the beam reflected from the cavity side of the output coupler returns to the gain chip. To achieve lasing, use a high-gain, large-area photodetector [33] to detect laser emission. Use long pass filters to block pump light, and 1/2" lens tube after the filters to block room light. Switch the detector to the maximum gain setting and monitor the signal on a multimeter or an oscilloscope. Position the detector so that the beam from the VECSEL would be incident on the detector active area. Set the pump diode current to about $1-2\,\mathrm{A}$ above where the VECSEL threshold is expected to be [34] . Iteratively adjust the output coupler orientation to maximize the signal on the photodetector. There should be a clear maximum in the signal when the laser is close to lasing. When lasing occurs there will be a distinct jump in the photodiode signal. Once this has happened, remove the photodetector and insert a thermal power meter. Optimize the output coupler orientation for maximum output power and for the lowest possible lasing threshold. Next insert the BRF into the cavity. The BRF is at Brewster's angle and will displace the beam slightly. Use the photodiode and adjust the OC orientation to achieve lasing again. It may be necessary to increase the pump power to achieve lasing if the BRF is selecting frequencies far from the center of the gain curve. Rotate the BRF to find the maximum output power. Adjust the BRF orientation and the OC orientation to minimize the pump power required to reach threshold. Finally insert the etalon into the cavity. Adjust the etalon orientation to achieve lasing again and to optimize the output power.

D.3.3 Tuning the laser to the desired wavelength:

Monitor the VECSEL wavelength using a wavemeter. Rotate the BRF and/or adjust its temperature to coarsely tune the laser. When the laser is as close as possible to the desired wavelength, adjust the etalon temperature. Increasing the etalon temperature should increase the

[33] Thorlabs PDA50B

[34] The threshold current depends on many factors including the gain material, the output coupler reflectivity, and the pump spotsize on the gains chip. If I do not have any idea what the threshold current should be, I would start at about 15 A

laser wavelength. There will be mode hops in roughly $\sim 1\,\mathrm{GHz}$ steps (corresponding the the FSR of the laser cavity). Once the laser is within $\sim 1\,\mathrm{GHZ}$ of the desired frequency, the PZT can be used for finer adjustment. Optimize the output power at the desired wavelength by making fine adjustments to the etalon and BRF temperatures.

D.4 Output power

Figure D.9 presents example measurements of the output power of an 1140 nm VESCEL. Above threshold, the output power initially increases linearly with the pump power. At sufficiently high pump power, thermal gradients in the gain chip will reduce the power conversion efficiency. In general, the efficiency of a laser depends on the single-pass gain and the cavity losses. For single-frequency lasers, intra-cavity frequency selective elements can contribute a significant loss. For the data in Fig. D.9, the slope efficiency drops from 27 % in multimode operation (no frequency selective elements) to 21 % when the etalon and BRF are inserted into the cavity. The output coupler reflectively can be optimized to maximize the efficiency of the VECSEL for a given pump power. For each different gain material we typically try OCs with a few different reflectivity values R ranging from 0.5 to 3.0 %. For the data in D.9, the single-mode slope efficiency drops by more than a factor of 2 if the OC is changed to one with $R = 0.5\,\%$. I have found that it is usually worthwhile starting with an OC of $R = 2.0\,\%$.

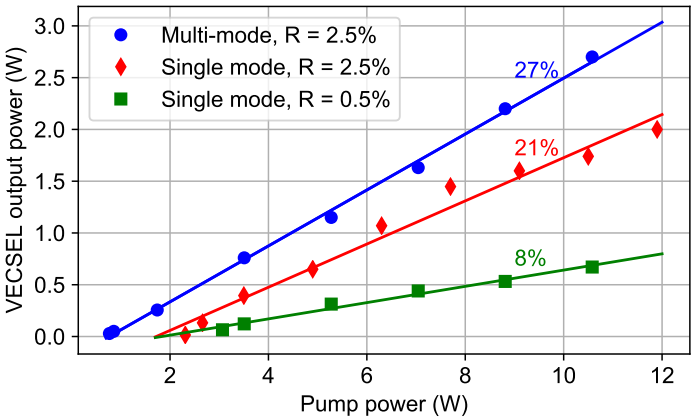

Figure D.9: Output power of an 1140 nm VECSEL as a function of pump power for multi-mode and single-mode operation for different output coupler reflectivities (R). Data points are measured pump power. Solid lines are linear fits to the data. Slope efficiencies obtained from the fits are listed. There is $\sim 5\%$ calibration uncertainty for all power measurements (not shown).